To the Graduate Council:

I am submitting herewith a thesis written by Sheri Lea Hlady entitled "A Numerical Study of a Simulated Solid Rocket Motor, Including an Examination of Vortex Shedding". I have examined the final copy of this thesis for form and content and recommend that it be accepted in partial fulfillment of the requirements for the degree of Master of Science, with a major in Engineering Science.

G.A. Flandro, Major Professor

We have read this thesis and
recommend its acceptance:

Accepted for the council:

Associate Vice Chancellor and
Dean of the Graduate School

A NUMERICAL STUDY OF A SOLID ROCKET MOTOR, INCLUDING AN EXAMINATION OF VORTEX SHEDDING

A Thesis

Presented for the

Master of Science

Degree

The University of Tennessee, Knoxville

Sheri Lea Hlady

December 1998

With all my love,

this thesis is dedicated to

Wilson Denovan Johnston.

Always with me.

Per ardua ad astra.

ACKNOWLEDGMENTS

First and foremost, I would like to acknowledge the support of my family. My Grandfather for his perspicacity and convivial nature. My Grandmother, Luella Johnston, for her strength, as well as her unconditional love and support. To my parents, Dorothy and Doug, who began my education, and for their love, support, and encouragement along the way. To my "little" brother Jason, for always being there, for being proud of me, and especially for his free proof-reading services. Thank you all for all the motivation that you have provided.

I must also pay tribute to the entire UTSI staff; they make the institution what it is, and have thus provided me with the opportunity to pursue postgraduate studies. In particular I would like to thank Dr. Roach for starting me on this journey, and to my committee members, Dr. Flandro, Dr. Merkle, and Dr. Antar, for helping me finish it. I also thank Dr. Moulden for his help with Fourier Transforms. The help of Brenda Brooks, Linda Engels, Mary-Frances Ferber, Kathy Hice, and Mary Lo, with details such as graphics, forms, fax machines, and library searches is greatly appreciated.

ABSTRACT

This thesis is an attempt to improve upon a previous numerical study of internal flow fields in a simulated solid rocket. The current study attempts to reduce or remove two obvious errors: one in time accuracy; the other, the splitting error produced by the Approximate Factorization scheme. To improve the time accuracy, the code is made second order in time; results are presented. To remove the AF splitting error, quasi-Newton inner iterations are used. There are a number of ways to optimize the use of inner iterations. This thesis addresses the questions: when is the best time to use inner iterations, how many should be used, and is there a significant improvement in convergence?

Results of this numerical study are compared to previous numerical, experimental, and analytical results to investigate one of the major sources of instability in solid rocket motors, that of acoustic axial disturbances. One source of instability is traced to a vortex shedding phenomenon. The periodic disturbance occurs at the natural frequency of the rocket chamber.

TABLE OF CONTENTS

CHAPTER		PAGE
1.	INTRODUCTION	1
2.	BACKGROUND	3
3.	NUMERICAL PROCEDURE	8
	Inner Iterations	10
	Artificial Viscosity	16
	Computational Grids	16
4.	INITIAL CONDITIONS	23
5.	BOUNDARY CONDITIONS	26
	Burning Surface Boundary	26
	Supersonic Outflow	27
	Solid Walls	28
	Centerline	28
6.	RESULTS AND DISCUSSION	30
	Steady State Convergence	30
	Pressure Wave	34
	Standing Wave	41
	Frequency of Oscillation	45
	Vorticity	52
7.	CONCLUSIONS AND RECOMMENDATIONS	59
	REFERENCES	61
	APPENDICES	65
	APPENDIX A: Pressure Contour Figures	66
	APPENDIX B: Velocity Magnitude Figures	77

APPENDIX C: Close-up Velocity Magnitude Figures 88

APPENDIX D: Close-up Velocity Vector Figures 94

VITA 100

LIST OF TABLES

TABLE		PAGE
1.	Reynolds' Numbers	40
2.	Axial Locations	51

LIST OF FIGURES

FIGURE		PAGE
1.	Slotted and Non-slotted Computational Grids.	18
2.	Residual Convergence for the Slotted Rocket.	31
3.	Residual Convergence of Inner Iterations.	35
4.	Residual Convergence for the Non-slotted Rocket.	36
5.	Pressure Profile for the Two Rockets at the Head End and in the Chamber at X/D = 1.8.	37
6.	Continuous Increase in Pressure at the Head End Centerline.	41
7.	Momentum Flux at the Throat Levels Off.	42
8.	Pressure Wave Amplitudes in the Two Rockets.	43
9.	Typical Velocity Trace from Chamber Location X/D=1.8.	46
10.	Amplitude and Phase Distributions for Selected Pressure and Velocity Computations.	47
11.	Axial Velocity Profiles of the Two Rockets.	55
A-A.1	Pressure contours at 1/10th of a cycle.	67
A-A.2	Pressure contours at 2/10th of a cycle.	68
A-A.3	Pressure contours at 3/10th of a cycle.	69
A-A.4	Pressure contours at 4/10th of a cycle.	70
A-A.5	Pressure contours at 5/10th of a cycle.	71
A-A.6	Pressure contours at 6/10th of a cycle.	72
A-A.7	Pressure contours at 7/10th of a cycle.	73
A-A.8	Pressure contours at 8/10th of a cycle.	74

A-A.9	Pressure contours at 9/10th of a cycle.	75
A-A.10	Pressure contours at 10/10th of a cycle.	76
A-B.1	Velocity magnitude contours at 1/10th of a cycle.	78
A-B.2	Velocity magnitude contours at 2/10th of a cycle.	79
A-B.3	Velocity magnitude contours at 3/10th of a cycle.	80
A-B.4	Velocity magnitude contours at 4/10th of a cycle.	81
A-B.5	Velocity magnitude contours at 5/10th of a cycle.	82
A-B.6	Velocity magnitude contours at 6/10th of a cycle.	83
A-B.7	Velocity magnitude contours at 7/10th of a cycle.	84
A-B.8	Velocity magnitude contours at 8/10th of a cycle.	85
A-B.9	Velocity magnitude contours at 9/10th of a cycle.	86
A-B.10	Velocity magnitude contours at 10/10th of a cycle.	87
A-C.1	Close-up of velocity magnitude contours near the slot at 1/10th of a cycle.	89
A-C.2	Close-up of velocity magnitude contours near the slot at 2/10th of a cycle.	89
A-C.3	Close-up of velocity magnitude contours near the slot at 3/10th of a cycle.	90
A-C.4	Close-up of velocity magnitude contours near the slot at 4/10th of a cycle.	90
A-C.5	Close-up of velocity magnitude contours near the slot at 5/10th of a cycle.	91
A-C.6	Close-up of velocity magnitude contours near the slot at 6/10th of a cycle.	91
A-C.7	Close-up of velocity magnitude contours near the slot at 7/10th of a cycle.	92

A-C.8 Close-up of velocity magnitude contours near the slot at 8/10th of a cycle. 92

A-C.9 Close-up of velocity magnitude contours near the slot at 9/10th of a cycle. 93

A-C.10 Close-up of velocity magnitude contours near the slot at 10/10th of a cycle. 93

A-D.1 Close-up of velocity vectors near the slot at 1/10th of a cycle. 95

A-D.2 Close-up of velocity vectors near the slot at 2/10th of a cycle. 95

A-D.3 Close-up of velocity vectors near the slot at 3/10th of a cycle. 96

A-D.4 Close-up of velocity vectors near the slot at 4/10th of a cycle. 96

A-D.5 Close-up of velocity vectors near the slot at 5/10th of a cycle. 97

A-D.6 Close-up of velocity vectors near the slot at 6/10th of a cycle. 97

A-D.7 Close-up of velocity vectors near the slot at 7/10th of a cycle. 98

A-D.8 Close-up of velocity vectors near the slot at 8/10th of a cycle. 98

A-D.9 Close-up of velocity vectors near the slot at 9/10th of a cycle. 99

A-D.10 Close-up of velocity vectors near the slot at 10/10th of a cycle. 99

LIST OF ABBREVIATIONS

A_	Derivative Operator
AF	Approximate Factorization
B_	Derivative Operator
CPU	Central Processing Unit
F,G,H	Flux vectors
FFT	Fast Fourier Transform
Hz	Hertz
ISTP	Counter for regular time steps
k	Inner iteration counter
KSTP	Counter for inner iteration steps
LHS	Left hand side
N_2	Nitrogen gas
NS	Navier-Stokes
M_b	Burning surface Mach number
max	Maximum pressure amplitude
min	Minimum pressure amplitude
n	Iteration counter
P	Pressure
PHECL	Pressure at the head end centerline
Pr	Prandtl number
QNI	Quasi-Newton iterations
q	Dependent variable vector
Re	Reynolds Number
Re*	Unit Reynolds Number

RHS	Right hand side
SRM	Solid Rocket Motor
t	Time
UTSI	University of Tennessee Space Institute
u	Axial velocity
v	Radial velocity
VENUS	Vectorized Euler Navier-Stokes Unsteady Solver
WRT	With respect to
X/D	Nondimensional axial location; ratio of chamber length over chamber diameter
γ	Ratio of Specific Heats
μ	Dynamic Viscosity Coefficient
ρ	Density
Ω	Vorticity

Chapter 1

INTRODUCTION

This thesis was initiated to improve upon previous work, specifically two studies, one by Smith, *et al.* [1], and the other by Flandro, *et al.* [2]. It is a numerical study of an unsteady, viscous, internal flow field in a solid rocket motor (SRM), under acoustically excited conditions.

Due to the finite precision of computer calculations, and the limitations of using discrete numerical methods to model continuous phenomena, errors in numerical schemes are unavoidable. Although Smith, *et al.* [1], was a continuation of Flandro, *et al.* [2], there was still room for improvement. This thesis addresses four types of errors in the previous numerical schemes: space accuracy, time accuracy, the splitting error of the Approximate Factorization (AF) algorithm, and assumptions regarding boundary conditions.

The computer code used in this thesis, as well as in Smith, *et al.* [1], and Flandro, *et al.* [2], is a version of the **V**ectorized **E**uler **N**avier-Stokes **U**nsteady **S**olver (VENUS), developed by R. L. Roach [3]. The VENUS code solves the unsteady compressible, Navier-Stokes (NS) equations, using an AF algorithm.

The space accuracy error was investigated first. The code was second order in space; an attempt was made to make the code fourth order. In the fourth order version, the corner of the nozzle and outflow boundary was unstable. Extensive efforts could not

eliminate the instability; using a code that was accurate to second order in space, the focus of the study thus moved on to investigate the remaining errors.

Fortunately, more success was achieved in improving the time accuracy. The code was made second order in time; results are presented.

Removing the AF splitting error, through the use of quasi-Newton inner iterations (QNI), proved to be an interesting path of study. The original intent was to compare different methods of implementing inner iterations such as: dual time stepping and alternative direction implicit. After the QNI were implemented, evidence suggested that the QNI algorithm was correct, however, residual errors were not reduced. Pursuit of the anomaly lead to an examination of vortex shedding. A comparison of different inner iteration implementations did not seem appropriate under the current investigation.

Finally, an attempt was made to write a numerical burning surface boundary condition analogous to Flandro's [4, 5] analytical derivation. Round off error made this algorithm ineffective; results are discussed.

Chapter 2

BACKGROUND

It is important to understand combustion instability in SRMs for many reasons, not the least of which is to keep them from exploding unexpectedly. Understanding, predicting, and controlling the instability may lead to safer and more efficient SRMs.

Many authors (*e.g.*, Brown *et al.*, Flandro, Kourta *et al.*, Anthoine *et al.*, Roh *et al.*, and Yang *et al.*), agree that the classical, one dimensional, plane wave, acoustic theory fails to accurately capture the nature of a SRM flow [4-10]. The plane wave model used in most stability analyses is insufficient, since acoustic oscillations are often present in a flow field. Although a stability model may predict stability for pressure and thrust in SRMs, such as the Titan IV, in actual firing tests, the rockets are not always stable.[11]

After a static firing test of a U.S. Air Force Titan IV prequalification motor failed, Chang *et al.* [11] provided a numerical analysis of the mishap. They used a full NS code that varied each term in the viscous stress tensor separately, and ran compressible, viscous, conditions on an adaptive, unstructured, finite element mesh. They found that there were large pressure gradients and that the coupling of gas pressure and grain deformation continued, causing head end pressure to rise and finally rupture the motor case. The measured data showed that the difference between the head and

aft end pressure was significantly greater than that predicted for a well behaved motor.

Pressure increases as described above are related to the interaction of acoustic waves and the unsteady combustion process. Many authors (*e.g.*, Flandro, Kourta *et al.*, and Flatau *et al.*), have reported flow instabilities such as: vortex shedding, shear flow, and acoustic oscillations [4,7,12].

Oscillations which pulse at the frequency of the acoustic mode of the chamber were found in a number of studies [7,12,13]. The motion of the oscillation affects combustion by causing local changes in the gas phase of the combustive process [4,8,9]. The oscillations have been linked to periodic vortex shedding [13], and acoustic waves [9]. Anthoine *et al.*, found that periodic vortex shedding in the Ariane 5 SRM, is the result of strong coupling between the instability of the mean shear flow and the natural acoustic mode of the chamber [14].

In Kourta *et al.*, thrust and pressure oscillations were studied using an explicit predictor/corrector MacCormack scheme [7]. Forward or backward approximations were used on inviscid terms, while central differencing was used on the viscous terms. Like the present study, Kourta *et al.*, was second order in space and time [7]. AF was not used for unsteady calculations to avoid damping effects. The boundary conditions used were: no slip at the head end and in between the burn surface segments, injection from the burning surface, symmetry on the internal side, and supersonic on the outflow. Time steps were 0.5E-6 seconds; 3,000,000 iterations were

run. It was noted that a vortex developed halfway down the chamber as a result of a segment corner, the vortex then traveled down the chamber and was absorbed by the nozzle. Differing viscosity was examined. Increasing the viscosity had the effect of reducing the amplitude of oscillations and vortex shedding became more organized. [7]

Vortices occur when shearing is present in the flow. Shearing can occur in areas where the flow turns rapidly, for example, when flow is injected normal from the burning surface and must turn longitudinally to exit the chamber [4,5,7]. Sharp corners are another possible shearing source. During combustion, as the propellant burns off, the surface retreats thus exposing inhibitor rings. As these rings begin to protrude into the flow field, they may become the source of vortex shedding [12]. Kourta *et al.*, looked at sharp as well as smooth corners [7]. The affect of the smooth segment corner was to lower the amplitude of the oscillation, while the vortex shedding remained at the same frequency [7].

In Smith *et al.*, results from an experimental cold flow study were presented along with matching numerical and analytical results [2]. One aspect of the flow that the numerical analysis did not capture well was the amplitude and phase angle of the acoustic flow components [2]. Analytical and experimental works show amplitude overshoot is close to double that of the centerline value while the profiles contain 6-7 peaks encompassing 40% to 60% of the radial distance to the centerline [2]. Amplitude profiles, similar to the analytical and experimental ones, have been captured numerically

by Baum, Kassoy *et al.*, Vuillot and Avalon [15-17]. However, all of the numerical results underestimate the amplitude, the number of peaks, and the distance the effect carries towards the centerline. It appears that numerical dissipation dampens some important physics.

The final error that was investigated in this thesis was the burning surface algorithm. How to calculate the radial velocity off of a burning surface is a point of much debate. It is a complex phenomenon involving grain size, chemical reactions, and flow field interactions within the chamber. Usually an admittance function is used. The admittance function used in this thesis was: ρv = constant.

The problem with using an admittance function is that it assumes one understands surface combustion when in fact, surface combustion is the item under study. The acoustic fluctuations in the chamber interact with the burning surface, which affects the surface combustion.

Using Crocco's theorem, Flandro writes [5,18] the surface vorticity as:

$$\Omega(t)\Big|_{surface} = \frac{\partial u}{\partial y} = M_b(\pi^2 x) - \frac{1}{M_b}\frac{\partial p'}{\partial x} \qquad [1]$$

where:

- M_b = burning surface Mach number
- x = dimensionless axial position measured from the head end.
- $\partial u / \partial y$ = rate of change of axial velocity normal to the surface (vorticity magnitude).
- $\partial p' / \partial x$ = axial unsteady pressure gradient at the surface from the numerical solution.

Using this formulation, the goal was a new description of the velocity at the burning surface. Therefore, the following boundary condition algorithm was tried.

$$\Omega(t)\Big|_{surface} = \frac{\partial u}{\partial y} - \frac{\partial v}{\partial x} = M_b(\pi^2 x) - \frac{1}{M_b}\frac{\partial p'}{\partial x} \qquad [2]$$

By solving for the derivative $\partial v / \partial x$, it is possible to get a value of v on the surface.

$$v(i) = v(i-1) + \frac{1}{2}\frac{(\Omega - \partial u/\partial y)_i - (\Omega - \partial u/\partial y)_{i-1}}{x(i) - x(i-1)} \qquad [3]$$

Although Flandro was able to solve the equations analytically, a problem inherent with numerical calculations prevented a useful numerical solution. The terms Ω and $\partial u / \partial y$ are of the same order, but $\partial v / \partial x$ is much smaller. The difference $(\Omega - \partial u/\partial y)_i - (\Omega - \partial u/\partial y)_{i-1}$ is a very small number, therefore each subtraction introduces a numerical round off error. This error is compounded when the equation is integrated along the entire burning surface; the summation of all the round off errors quickly makes the calculation meaningless. This is further indication that v is small.

It would be interesting and worthwhile to replicate Flandro's analytical results numerically. A more creative implementation is needed and is left for future studies to pursue.

Chapter 3

NUMERICAL PROCEDURE

The numerical method is based on the AF methods of Pulliam and Steger, Crank - Nicholson, Beam and Warming, and Douglass and Gunn [19].

The unsteady, three-dimensional, NS equations can be written in vector form for Cartesian Coordinates as [19]:

$$q_t + (F - F_v)_x + (G - G_v)_y + (H - H_v)_z = 0 \qquad [4]$$

where,

$$q = \begin{bmatrix} \rho \\ \rho u \\ \rho v \\ \rho w \\ \rho e \end{bmatrix} \quad F = \begin{bmatrix} \rho u \\ \rho u^2 + P \\ \rho uv \\ \rho uw \\ u(e+P) \end{bmatrix} \quad G = \begin{bmatrix} \rho v \\ \rho uv \\ \rho v^2 + P \\ \rho vw \\ v(e+P) \end{bmatrix} \quad H = \begin{bmatrix} \rho w \\ \rho uw \\ \rho vw \\ \rho w^2 + P \\ w(e+P) \end{bmatrix}$$

$$P = (\gamma - 1)[e - \tfrac{\rho}{2}(u^2 + v^2 + w^2)]$$

$$F_v = \begin{bmatrix} 0 \\ \tau_{xx} \\ \tau_{xy} \\ \tau_{xz} \\ \delta_x \end{bmatrix} \quad G_v = \begin{bmatrix} 0 \\ \tau_{xy} \\ \tau_{yy} \\ \tau_{yz} \\ \delta_y \end{bmatrix} \quad H_v = \begin{bmatrix} 0 \\ \tau_{xz} \\ \tau_{yz} \\ \tau_{zz} \\ \delta_z \end{bmatrix}$$

$$\tau_{xx} = 2\mu\frac{\partial u}{\partial x} + \lambda\nabla\cdot V \qquad \tau_{yy} = 2\mu\frac{\partial v}{\partial y} + \lambda\nabla\cdot V \qquad \tau_{zz} = 2\mu\frac{\partial w}{\partial z} + \lambda\nabla\cdot V$$

$$\tau_{xy} = \mu\left(\frac{\partial u}{\partial y} + \frac{\partial v}{\partial x}\right) \qquad \tau_{yz} = \mu\left(\frac{\partial v}{\partial z} + \frac{\partial w}{\partial y}\right) \qquad \tau_{xz} = \mu\left(\frac{\partial w}{\partial x} + \frac{\partial u}{\partial z}\right)$$

$$\delta_x = \frac{\gamma\mu}{Pr}\frac{\partial \varepsilon}{\partial x} + u\tau_{xx} + v\tau_{xy} + w\tau_{xz} \qquad \delta_y = \frac{\gamma\mu}{Pr}\frac{\partial \varepsilon}{\partial y} + u\tau_{yx} + v\tau_{yy} + w\tau_{yz}$$

$$\delta_z = \frac{\gamma\mu}{Pr}\frac{\partial \varepsilon}{\partial z} + u\tau_{zx} + v\tau_{zy} + w\tau_{zz}$$

$$\varepsilon = \frac{e}{\rho} - \frac{1}{2}\left(u^2 + v^2 + w^2\right) \qquad \lambda = -\frac{2}{3}\mu$$

In curvilinear coordinates the above equations become:

$$\hat{q}_t + \hat{F}_\xi^{n+1} + \hat{G}_\eta^{n+1} + \hat{H}_\zeta^{n+1} = \left(\hat{F}_v\right)_\xi^n + \left(\hat{G}_v\right)_\eta^n + \left(\hat{H}_v\right)_\zeta^n \qquad [5]$$

$$\hat{q} = \frac{1}{J}\begin{bmatrix} \rho \\ \rho u \\ \rho v \\ \rho w \\ e \end{bmatrix}$$

$$\hat{F} = \frac{1}{J}\left(\xi_t q + \xi_x F + \xi_y G + \xi_z H\right)$$

$$\hat{G} = \frac{1}{J}\left(\eta_t q + \eta_x F + \eta_y G + \eta_z H\right)$$

$$\hat{H} = \frac{1}{J}\left(\zeta_t q + \zeta_x F + \zeta_y G + \zeta_z H\right)$$

Where n is the current (known) time step and n+1 is the next (unknown) time step. Thus the convection terms are solved implicitly while the viscous terms are lagged by one iteration.

Inner Iterations

It is now time to add the inner iterations. Consider again, the implicit finite difference solution of the vectorized NS equations [19]:

$$q_t + f(q)_x + g(q)_y = 0 \qquad [6]$$

Solving implicitly this can be written [20]:

$$(1+\xi)\Delta q^n - \xi\Delta q^{n-1} =$$

$$-\Delta t\left[\theta\frac{\partial f^{n+1}}{\partial x} + (1-\theta)\frac{\partial f^n}{\partial x}\right] - \Delta t\left[\theta\frac{\partial g^{n+1}}{\partial y} + (1-\theta)\frac{\partial g^n}{\partial y}\right] + (\theta - \frac{1}{2} - \xi)\vartheta(\Delta t^2) \qquad [7]$$

Where:

$$\Delta q^n = q^{n+1} - q^n$$

$$\Delta q^{n-1} = \Delta q^n - \Delta q^{n-1}$$

And θ and ξ determine the type of implicit scheme and control the time accuracy. The values of θ = 1 and ξ = 0 were used for an Euler Implicit Scheme, first order in time, while the values of θ = 1 and ξ = 0.5 were used for a Three Point Backward Implicit scheme with second order time accuracy. The flux vectors, F and G, are then expanded in time by a Taylor series. [19]

$$f^{n+1} = f^n + \Delta t\left(\frac{\partial f}{\partial t}\right)^n + \vartheta(\Delta t^2)$$

$$\Rightarrow f^{n+1} = f^n + \Delta t\left[\frac{\partial f}{\partial q}\frac{\partial q}{\partial t}\right]^n + \vartheta(\Delta t^2) \qquad [8]$$

Canceling the Δt term with the ∂t term and setting $\partial f / \partial q = A$ results in:

$$\Rightarrow f^{n+1} = f^n + A^n\left(q^{n+1} - q^n\right) + \vartheta(\Delta t^2)$$

$$\Rightarrow f^{n+1} = f^n + A^n \Delta q^n + \vartheta(\Delta t^2) \qquad [9]$$

This equation is substituted into equation [7] and the order term is now dropped for brevity, although it is implied throughout the derivation.

$$(1+\xi)\Delta q^n - \xi \Delta q^{n-1}$$

$$= -\Delta t\left[\theta \frac{\partial}{\partial x}(f^n + A^n \Delta q^n) + (1-\theta)\frac{\partial f^n}{\partial x}\right] - \Delta t\left[\theta \frac{\partial}{\partial y}(g^n + B^n \Delta q^n) + (1-\theta)\frac{\partial g^n}{\partial y}\right]$$

$$= -\Delta t\left[\theta \frac{\partial}{\partial x}(A^n \Delta q^n) + \frac{\partial f^n}{\partial x} + \theta \frac{\partial}{\partial y}(B^n \Delta q^n) + \frac{\partial g^n}{\partial y}\right] \qquad [10]$$

Move the coefficients of Δq^n to LHS and coefficients of Δq^{n-1} to the RHS:

$$\left[(1+\xi)I + \Delta t\theta(A_)_x^n + \Delta t\theta(B_)_y^n\right]\Delta q^n = -\Delta t(f_x^n + g_y^n) + \xi \Delta q^{n-1} \qquad [11]$$

Where A and B are as defined above, with the "_" signifying a derivative operator. To solve the system at this point, the LHS operation would require a pentadiagonal coefficient matrix with a large number of diagonals in between the three main diagonal groups and the outer two. This would require a large amount of computer time to solve. To expedite the process, divide through by $(1+\xi)$, then factor the LHS.[19] Next, the derivative operator is approximately factored to give:

$$\left\{\left[I+\frac{\theta\Delta t}{(1+\xi)}(A_)_x^n\right]\left[I+\frac{\theta\Delta t}{(1+\xi)}(B_)_y^n\right]-\left(\frac{\theta\Delta t}{(1+\xi)}\right)^2(A_)_x^n(B_)_y^n\right\}\Delta q^n$$

$$=-\frac{\Delta t}{(1+\xi)}(f_x^n+g_y^n)+\frac{\xi}{(1+\xi)}\Delta q^{n-1} \qquad [12]$$

The factorization error could be dropped at this point. The author chose to combine the error term with the error term arising from the inner iteration implementation (see equations [16-17]). The error term is dropped before it is implemented into the code (see equation 20]). Now, write out the Δq terms:

$$\left[I+\frac{\theta\Delta t}{(1+\xi)}(A_)_x^n\right]\left[I+\frac{\theta\Delta t}{(1+\xi)}(B_)_y^n\right]\left(q^{n+1}-q^n\right)$$

$$=-\frac{\Delta t}{(1+\xi)}(f_x^n+g_y^n)+\frac{\xi}{(1+\xi)}\left(q^n-q^{n-1}\right)+\left(\frac{\theta\Delta t}{(1+\xi)}\right)^2(A_)_x^n(B_)_y^n\left(q^{n+1}-q^n\right) \qquad [13]$$

To get the inner iteration form, an intermediate level value of q, called q^k, is added and subtracted from the left side:

$$\left[I+\frac{\theta\Delta t}{(1+\xi)}(A_)_x^n\right]\left[I+\frac{\theta\Delta t}{(1+\xi)}(B_)_y^n\right]\left(q^{n+1}-q^k+q^k-q^n\right)$$

$$=-\frac{\Delta t}{(1+\xi)}(f_x^n+g_y^n)+\frac{\xi}{(1+\xi)}\left(q^n-q^{n-1}\right)+\left(\frac{\theta\Delta t}{(1+\xi)}\right)^2(A_)_x^n(B_)_y^n\left(q^{n+1}-q^n\right) \qquad [14]$$

This intermediate value of q will be the iterated value of the dependent variables. It will start off being equal to the value of q at the nth time level an will end up, after iterating, with the n+1 value

of q. Iterations on k are identical to iterations on n except for the fact that k iterations occur in between n iterations; taking only one k iteration is exactly the same as taking one n iteration. The term q^{n+1} could also be written as q^{k+1}, but it is left as q^{n+1} to emphasize that the goal an improvement in the accuracy of the nth time step.

Now, take q^k-q^n to the RHS, then expand the factors on the RHS.

$$\left[I+\frac{\theta\Delta t}{(1+\xi)}(A_)_x^n\right]\left[I+\frac{\theta\Delta t}{(1+\xi)}(B_)_y^n\right]\left(q^{n+1}-q^k\right)$$

$$=-\frac{\Delta t}{(1+\xi)}(f_x^n+g_y^n)+\left(\frac{\theta\Delta t}{(1+\xi)}\right)^2(A_)_x^n(B_)_y^n\left(q^{n-1}-q^k\right)$$

$$-\left[I+\frac{\theta\Delta t}{(1+\xi)}(A_)_x^n+\frac{\theta\Delta t}{(1+\xi)}(B_)_y^n+\left(\frac{\theta\Delta t}{(1+\xi)}\right)^2(A_)_x^n(B_)_y^n\right]\left(q^{n+1}-q^k\right)$$

Collect coefficients of the q's and the flux terms.

$$=-\left(\frac{1}{1+\xi}\right)\left[(1+\xi)q^k-(1+2\xi)q^n+\xi q^{n-1}\right]+\left(\frac{\theta\Delta t}{(1+\xi)}\right)^2(A_)_x^n(B_)_y^n\left(q^{n+1}-q^k\right)$$

$$-\frac{\Delta t}{(1+\xi)}(f_x^n+g_y^n)-\frac{\theta\Delta t}{(1+\xi)}\left[(A_)_x^n+(B_)_y^n\right]\left(q^k-q^n\right) \qquad [15]$$

Looking for a moment, just at the flux terms, add and subtract the flux derivatives on the RHS.

$$-\frac{\Delta t}{(1+\xi)}(f_x^n+g_y^n)-\frac{\theta\Delta t}{(1+\xi)}\left\{\left[(A_)_x^n+(B_)_y^n\right]\left(q^k-q^n\right)+\left[f_x^n-f_x^n+g_y^n-g_y^n\right]\right\}$$

Next, group terms in order to apply equation [9].

$$-\frac{\theta\Delta t}{(1+\xi)}\left\{\left[(A_)_x^n\Delta q^k+f_x^n\right]+\left[(B_)_y^n\Delta q^k+g_y^n\right]\right\}+\left(\frac{\theta\Delta t}{(1+\xi)}-\frac{\Delta t}{(1+\xi)}\right)\left(f_x^n+g_y^n\right)$$

$$=-\frac{\theta\Delta t}{(1+\xi)}\left(f_x^k+g_y^k\right)+(\theta-1)\frac{\Delta t\left(f_x^n+g_y^n\right)}{(1+\xi)} \qquad [16]$$

Thus, the complete equation is:

$$\left[I+\frac{\theta\Delta t}{(1+\xi)}(A_)_x^n\right]\left[I+\frac{\theta\Delta t}{(1+\xi)}(B_)_y^n\right]\left(q^{n+1}-q^k\right)$$

$$=-\left(\frac{1}{1+\xi}\right)\left[(1+\xi)q^k-(1+2\xi)q^n+\xi q^{n-1}\right]+\left(\frac{\theta\Delta t}{(1+\xi)}\right)^2(A_)_x^n(B_)_y^n\left(q^{n+1}-q^k\right)$$

$$-\frac{\theta\Delta t}{(1+\xi)}\left(f_x^k+g_y^k\right)+(\theta-1)\frac{\Delta t\left(f_x^n+g_y^n\right)}{(1+\xi)} \qquad [17]$$

For first order time accuracy,

$$\left[I+\Delta t(A_)_x^n\right]\left[I+\Delta t(B_)_y^n\right]\left(q^{n+1}-q^k\right)$$

$$=-\left[q^k-3q^n+q^{n-1}\right]+\Delta t^2(A_)_x^n(B_)_y^n\left(q^{n+1}-q^k\right)-\Delta t\left(f_x^k+g_y^k\right) \qquad [18]$$

For second order time accuracy,

$$\left[I+\frac{2}{3}\Delta t(A_)_x^n\right]\left[I+\frac{2}{3}\Delta t(B_)_y^n\right]\left(q^{n+1}-q^k\right)$$

$$=-\frac{1}{3}\left[3q^k-4q^n+3q^{n-1}\right]+\frac{4}{9}\Delta t^2(A_)_x^n(B_)_y^n\left(q^{n+1}-q^k\right)-\frac{2}{3}\Delta t\left(f_x^k+g_y^k\right) \qquad [19]$$

Theoretically, at convergence, $q^k = q^{n+1}$, and therefore the error term is zero. In application, the error term is dropped before the algorithm is implemented into the computer code. In order to eliminate excess multiplication in the independent sweeps of the AF algorithm the equation is multiplied through by $(1+\xi)/\theta\Delta t$.

$$\left[\frac{(1+\xi)}{\theta\Delta t}I+(A_)_x^n\right]\Delta q^* = -\left(\frac{1}{\theta\Delta t}\right)\left[(1+\xi)q^k-(1+2\xi)q^n+\xi q^{n-1}\right]-\left(f_x^k+g_y^k\right)$$

$$\left[\frac{(1+\xi)}{\theta\Delta t}I+(B_)_y^n\right]\left(q^{n+1}-q^k\right)=\frac{(1+\xi)}{\theta\Delta t}\Delta q^* \qquad [20]$$

Where:

$$\Delta q^* = \left[I+\frac{\theta\Delta t}{(1+\xi)}(B_)_y^n\right]\left(q^{n+1}-q^k\right)$$

For first order time accuracy, this becomes:

$$\left[\frac{1}{\Delta t}I+(A_)_x^n\right]\Delta q^* = -\frac{\Delta q^k}{\Delta t}-\left(f_x^k+g_y^k\right)$$

$$\left[\frac{1}{\Delta t}I+(B_)_y^n\right]\left(q^{n+1}-q^k\right)=\frac{1}{\Delta t}\Delta q^* \qquad [21]$$

Similarly, for second order time accuracy, the sweeps are written as:

$$\left[\frac{3}{2\Delta t}I+(A_)_x^n\right]\Delta q^* = -\left(\frac{1}{2\Delta t}\right)\left[3\Delta q^k-\Delta q^n\right]-\left(f_x^k+g_y^k\right)$$

$$\left[\frac{3}{2\Delta t}I+(B_)_y^n\right]\left(q^{n+1}-q^k\right)=\frac{3}{2\Delta t}\Delta q^* \qquad [22]$$

These two dimensional equations may now be solved more efficiently by using block-tridiagonal solvers instead of the previously mentioned pentadiagonal matrix. [19]

Artificial Viscosity

The convection terms were differentiated using central differences. This method produces odd-even decoupling. To compensate, the following term was added to the right hand side [1].

$$-\Delta t \varepsilon_E J^{-1}\left(\varepsilon_\xi \delta_{\xi\xi\xi\xi} + \varepsilon_\eta \delta_{\eta\eta\eta\eta} + \varepsilon_\zeta \delta_{\zeta\zeta\zeta\zeta}\right) J \hat{q}^n$$

Artificial diffusion was also added to the right hand side in the following second order implicit form [1]:

$$-\Delta t \varepsilon_I J^{-1}\left(\delta_{\xi\xi} + \delta_{\eta\eta} + \delta_{\zeta\zeta}\right) J$$

The constants are grid dependent. For this study, the explicit artificial coefficient was $\varepsilon_E = 0.015$, and the implicit artificial viscosity coefficient was $\varepsilon_I = 0.06$.

Computational Grids

Two grids, of matching chamber and nozzle dimensions, were used to study the flow inside a SRM. The only difference between the grids is that one had a cylindrical slot at the nozzle end of the chamber and the other did not. The slotted rocket grid is a representation of an experimental cold flow apparatus. The slot is

used as an inlet to drive a pressure wave inside the chamber. The slotted rocket and non-slotted rocket grids are shown in Figure 1. Figure 1.a and Figure 1.b, give a perspective of the length of the rockets, although the figures are not to scale. Figure 1.c and Figure 1.d are close-up views of the nozzle end of the grids.

The chamber radius is two inches, and the chamber length is 76.2 inches. Virtually all of the chamber wall is porous to allow transpiring air to simulate a burning surface. At the nozzle end of the chamber is a slot of width 0.6 inches and radius 3.0 inches. The slot is used to impose a periodic disturbance. The nozzle has a throat radius of 0.9 inches and an exit radius of 1.2 inches.

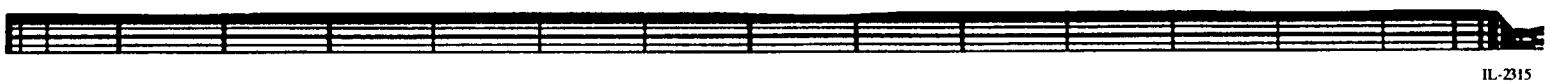
The slotted grid and its construction are described in detail in Smith *et al.* [1]. The non-slotted grid was constructed to match the dimensions of the slotted grid. A brief summary of the construction is presented here.

The slotted rocket consists of a chamber, a slot (both of cylindrical geometry), and a converging-diverging nozzle. The main grid is two dimensional in "x" and "y" coordinates. Since the flow is axisymetric, a third dimension is achieved by rotating the grid about the centerline axis. The domain of the grid includes the bounding surfaces, the centerline, outflow and interior flow region. [1]

The computational grid lines are counted with "I" and "J" indices. The index I counts grid lines parallel to the head end of the rocket. Numbering begins at the head end with I=1, and ends at the nozzle exit with I=II. The J index enumerates grid lines running parallel to the centerline in the chamber (these lines are curved



a. long view of slotted grid



IL-2315

b. long view of non-slotted grid

Figure 1. Slotted and non-slotted computational grids.

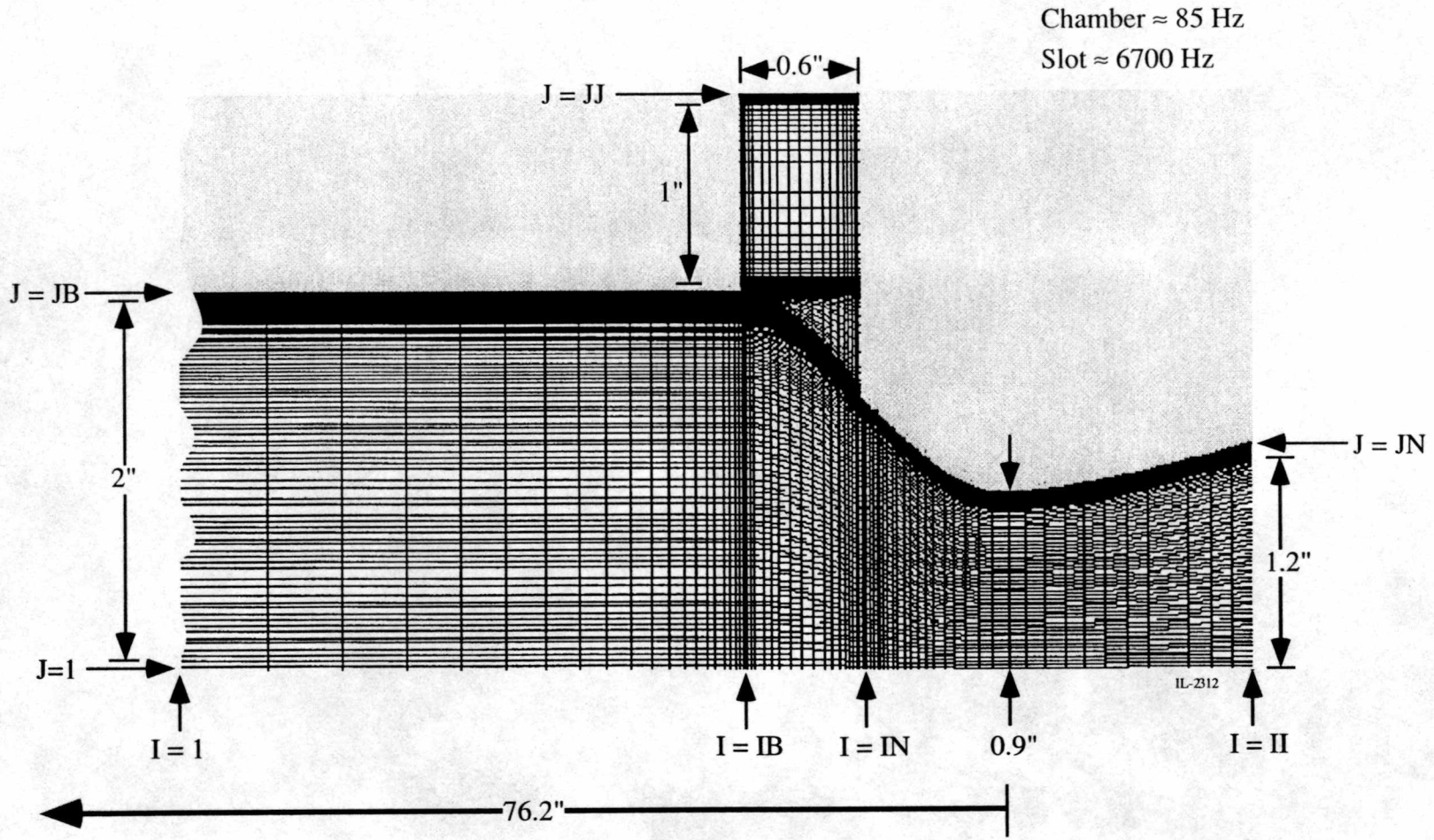


Figure 1.c Close-up of slotted rocket.

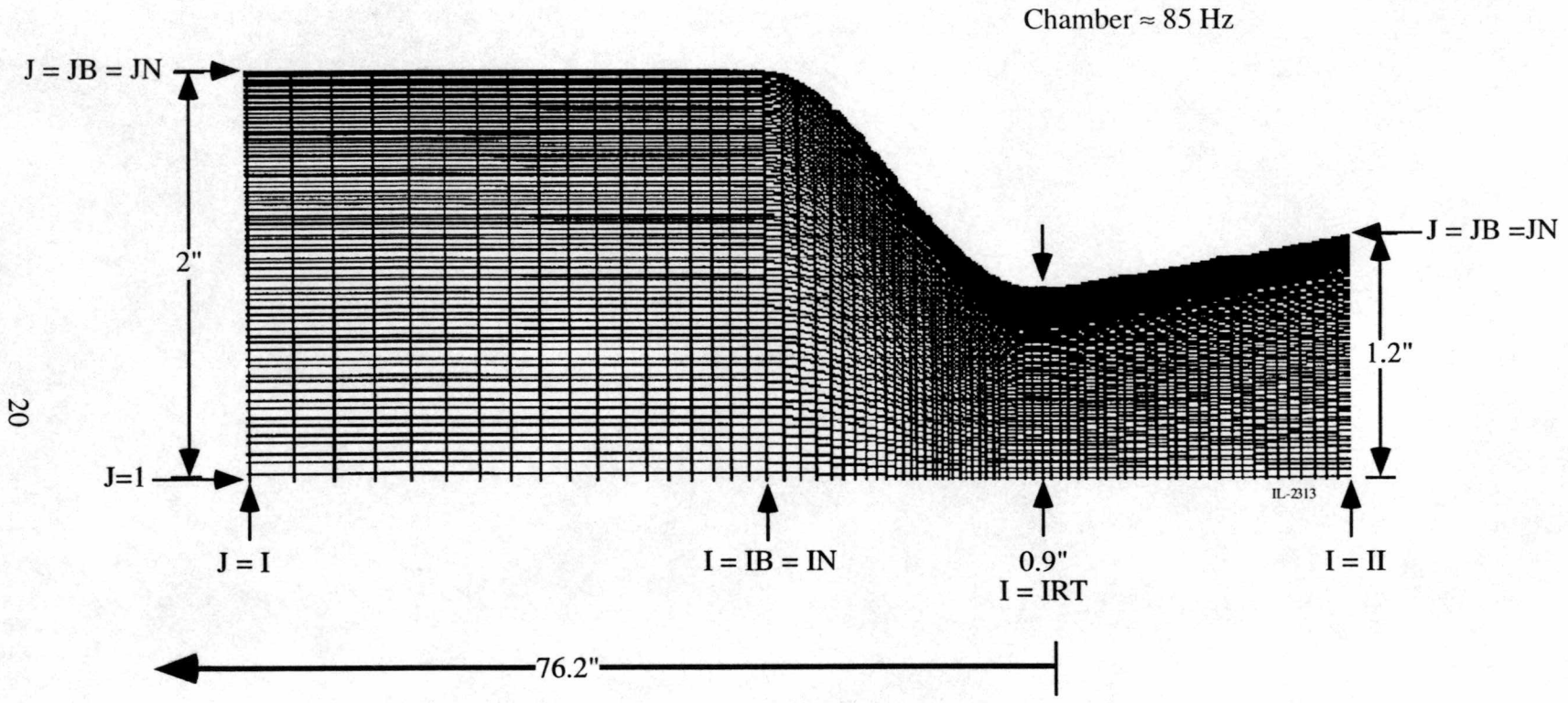


Figure 1.d Close-up of non-slotted rocket.

where the nozzle curves). The centerline is numbered, J=1, and the wall is J=JJ. [1]

More attention is given to areas where rapid change is expected, such as boundary layers, the throat, and the slot walls. To track the changes, more grid lines were placed in these areas. Since the major flow direction is axial, the spacing of the J lines near the burning surface is critical. The I grid line spacing is less critical, since there is very little flow velocity parallel to the head end or the two radial slot walls. The smallest axial spacing is generally one order of magnitude larger than the smallest radial spacing. [1]

Although the slot geometry is defined in cylindrical coordinates, and converted to a Cartesian system, the actual computations are performed in a transformed "ξ - η" plane. This generalized, curvilinear, coordinate system is used to reduce the complexity of the finite difference formulas, thus making the solutions procedure more general and easier to apply to other problems. [1]

The previous work [1] did not show the axial result of the implicit centerline boundary condition. Results of the new boundary condition will be presented.

Although previous work [1,2] reported CFL's of 25 and 50, and the code appears stable with CFL's as high as 100 or 500, for the current work, the CFL was always set to 10 (except for one specific run). All runs were time accurate. The CFL of 10 was based on the smallest grid spacing, which occurs in the radial direction. The smallest radial grid spacing is 10 times smaller than the smallest

axial grid spacing along the burning surface. The reason for this choice of CFL is the speed of the pressure wave in the chamber; at a CFL larger than 10, the wave will skip grid points on each iteration, effectively making the grid more coarse. The author chose to take full advantage of the fine grid spacing. It was suggested, in Vuillot and Avalon [7], that a coarse grid may compromise results.

The acoustic pressure wave in the chamber is a standing wave with a node at the chamber center and anti-nodes at the head and slot ends. The frequency of the wave is 85.2020 Hz which is the natural frequency of the chamber. It was therefore used as the driving frequency in the unsteady trials. The axial velocity is affected by the pressure wave. The velocity wave also has a frequency around 85 Hz.

Chapter 4

INITIAL CONDITIONS

This work expands on Smith *et al.* [1]; the initial conditions were established there. A summary will be presented here.

In an effort to reduce computation time, an effort was made to choose initial conditions which would closely resemble the steady state conditions of the rocket. Chamber conditions were generated from isentropic quasi-one dimensional gas dynamics [1]. Stagnation pressure and temperature, Reynolds number, the specific heat ratio, and the Prandtl number were all specified. Inflow and exit Mach numbers were calculated based on geometry. Static quantities at the surface are then calculated for pressure, temperature, and sound speed. From sound speed, the inflow radial velocity is calculated. Axial velocity is zero, thus enforcing the no slip condition. [1]

The Culick radial velocity profile is used to specify radial velocity in the chamber [1]. The axial velocity is determined by integrating along the surface form the head end to the axial location to determine inflow mass rate. The axial velocity is determined by scaling the Culick profile by the value of the integrated mass. Density and pressure are determined from stagnation values and local mach number. Internal energy comes from the velocity and pressure. Velocity in the slot is set to zero, density and internal energy are set to stagnation values. [1]

In the nozzle, the local area ratio and specific heat ratio are used to find Mach number temperature and sound speed. The velocity components are determined by the sine and cosine of the slope of the grid line in the stream wise direction, multiplied by the velocity magnitude. Density and pressure still come from the local mach number. Internal energy is calculated from the velocity magnitude and pressure. [1]

For the steady state runs, the initial condition was to set the q-vector to a constant value at all grid points on the interior of the chamber. This was done for two reasons. The initial conditions generated from the Culick profile are quite good, and thus convergence was achieved very rapidly. Since one objective of the thesis was to look at the effect of inner iterations, a poor choice on initial conditions makes it easier to see the effect of inner iterations. The second reason for this choice of initial conditions was to ensure that there was no initial pressure wave in the chamber. Runs were first computed on the non-slotted rocket. These initial conditions caused problems in the nozzle at the desired CFL of 10. When the CFL was lowered to 1.0, the code was stable. After 1000 iterations, it was possible to increase the CFL back to 10. All other runs used a CFL of 10.

Due to the difficulties with the non-slotted rocket initial conditions, a slightly different approached was used for the slotted rocket. All the q vectors in the chamber from the head end to the throat were set to a constant value. Past the throat, the outflow

initial conditions were supersonic. With these conditions, it was possible to start with a CFL of 10.

Subsequent runs used the output of the previous run as initial conditions, including the runs where the driving function was activated. In total, the longest run was over 500,000 iterations. Since all runs were time accurate, this corresponds to approximately 0.6 seconds and 40 oscillations.

Chapter 5

BOUNDARY CONDITIONS

A full description of the boundary conditions can be found in Smith *et al.*, [1]. A summary is presented here.

Burning Surface Boundary

This numerical study simulates a cold flow experiment which simulated the combustion of a SRM. In an actual SRM, the size of the main combustion zone and the time scale of the combustion process are both extremely small compared to the size and time scale of the mean gas flow. Although the combustion zone has a negligible thickness, important viscous effects such as the no slip condition play an important role in this zone [4]. The dominant effect in the combustion region is the release of chemical energy. Since chemical reactions have a much smaller time scale than any of the acoustic time scales, they are neglected. It is assumed that the gases emerging from the solid fuel are the final product of the combustion process and have properties appropriate to a completed set of reactions. The gas is assumed to be homogeneous and at some specified stagnation temperature and pressure. The expiration of real combustive gases was simulated by N_2 gas at 290 K and was thus, a cold flow. [1]

Numerical simulation of this boundary condition involved modeling an injecting surface. Mass flux was computed from the one-dimensional Mach number / area ratios with the nozzle throat area, burning surface area, and known stagnation conditions. To account for a boundary layer blockage at the throat, the mass flux was updated periodically until a steady state was reached. [1]

Second order, one sided differences with zero gradient are used to compute the surface values of the thermodynamic variables. Since the mass flux is fixed, the normal velocity is adjusted to change in the density. Since the density changes are proportional to changes in the pressure, this amounts to adjusting the burn back velocity in response to the pressure. [1]

Since a second order zero gradient condition was used on the thermodynamic variables, values from the interior were allowed to change burning surface values. Burning surface normal velocity computed from known mass flux. [1]

Supersonic Outflow

The outflow boundary is at the exit plane of the nozzle where the flow is primarily supersonic. The outflow boundary was treated implicitly using first order upwind differencing. [1]

Solid Walls

The head end of the chamber, all three walls of the slot, and the nozzle walls are all inert surfaces. For viscous flows, the velocities are zero. No heat transfer is allowed through the walls. Second order, one-sided differences are used to relate the surface density and pressure to their values at the two grid points nearest the wall. For example, the density can be written as:

$$\rho_1 = \frac{\rho_2 \Delta\eta_2^2 - \rho_3 \Delta\eta_3^2}{\Delta\eta_2^2 - \Delta\eta_3^2}$$

where the subscripts are 1 = wall, 2 and 3 are the two points nearest the wall, and Δ is the distance between the points.[1]

Centerline

Previous work used an explicit centerline boundary condition with second order zero gradient extrapolations for the axial velocity and all the thermodynamic variables. Radial velocity was zero. The explicit implementation caused the velocity magnitude to lag the rest of the domain, manifested in a curve near the centerline of the velocity amplitude versus radial position plots. Experimental and analytical results do not curve at the centerline. Instead of using the boundary conditions to form equations at the centerline, they were used to modify a quadratic interpolant through the centerline and its two neighboring points. To see how this works, one can consider fitting a quadratic through three points. For the variables with a

zero gradient, the coefficients of the quadratic were evaluated from the zero gradient at the centerline and the values of the two neighboring points. This results in the following expression for the derivative at J=2.

$$\left.\frac{\partial \phi}{\partial y}\right|_{j=2} = \frac{2}{3}\frac{\phi_3 - \phi_2}{\Delta y}$$

Thus, the expression for the derivative does not include the value of the variable at the centerline. Likewise, for variables with a zero value, a zero was used along with the values of the two neighboring points to evaluate the coefficients. In this case, the expression becomes:

$$\left.\frac{\partial \phi}{\partial y}\right|_{j=2} = \frac{\phi_3}{2\Delta y}$$

Again, these expressions do not use the value of the variable at the centerline, but do include the boundary condition at the centerline by a modification of the radial differencing at the nearest point. When these expressions are used in place of the usual differencing in the implicit solution procedure, the centerline values are not directly computed since there will be no coefficients for the centerline values. However, the finite difference expression at J=2 has been modified to reflect the centerline boundary conditions to second order. Thus the variables at J=2 are a combination of interior and boundary conditions and the effect of the new values of the variables along the centerline are felt by points at J=2. After the matrix is solved and new values of the dependent variables have been computed, the non-zero centerline values are found by using the second-order expression equivalent to the quadratic expression given above. [1]

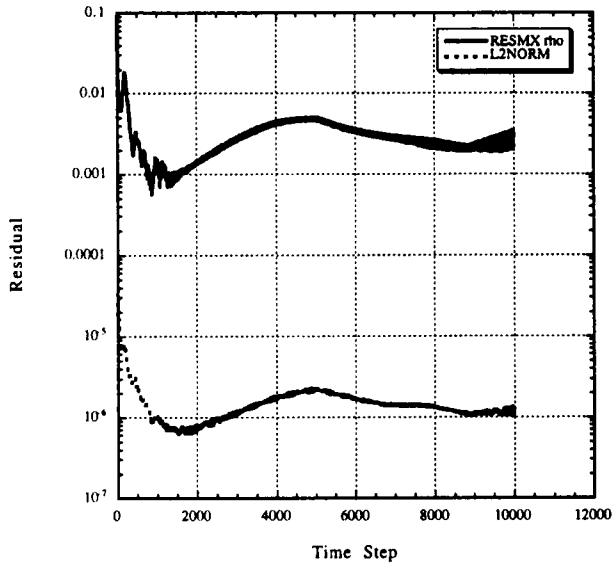
Chapter 6

RESULTS AND DISCUSSION

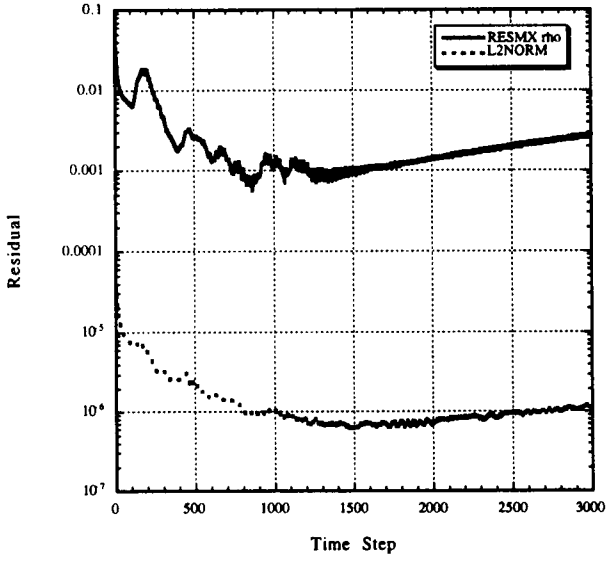
Steady State Convergence

Two criteria, the L2 Norm and the maximum residual, were used to judge whether or not the code had reached convergence. Usually a simple process, defining a steady state became a problem in this investigation. In Smith *et al.*, the code was reported to reach a steady state; a pressure wave, of small amplitude, was reported to damp out unless the system was being driven [1]. Using the slotted grid, the current version of the code would not converge; a periodic disturbance was sustained regardless of how long the code was run. Figure 2.a shows a plot of the residual convergence. Notice the sinusoidal wave form of the residuals after the residuals initially appeared to drop two orders of magnitude; an acceptable order of convergence would be at least three (but preferably more) orders of magnitude.

One source of error in the numerical scheme is the AF splitting error. Inner iterations were used in an attempt to remove this error. A comparison was made to try and optimize the number of iterations used as well as the time when to apply them. Figure 2.b is a close up of Figure 2.a, focusing on the first 3000 time steps. Figure 2.c show the convergence of the first 3000 time steps with 10 inner iterations between each time step. After 1500 time steps, there is no

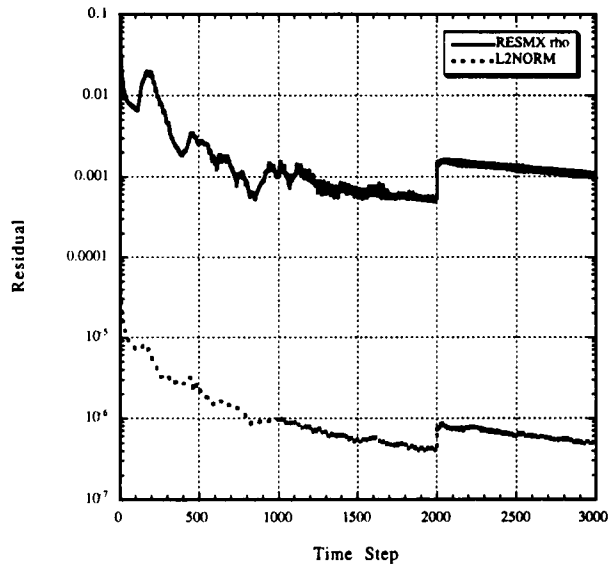


a.) Non-driven Conditions, Second Order Time Accuracy.

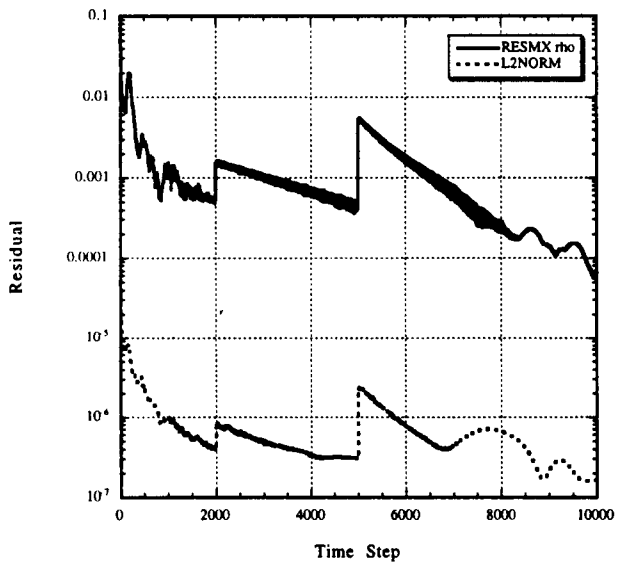


b.) Non-driven Conditions, Second Order Time Accuracy.
Close-up of First 3000 Time Steps.

Figure 2. Residual Convergence for the Slotted Rocket.



c.) Non-driven Conditions, Second Order Time Accuracy. Close-up of First 3000 Time Steps with 10 Inner Iterations per Time Step.



d.) Non-driven Conditions, Second Order Time Accuracy. Three Inner Iterations per Time Step.

Figure 2. Continued.

significant difference between the maximum residuals (refer to Figure 2.b and Figure 2.c). There is a very significant efficiency difference; taking 10 inner iterations with each time step requires 10 times the CPU time for calculations. Obviously, 10 inner iterations per time step are too expensive. Graveline found improved convergence rates when the inner iterations are applied several time steps into a run rather than right from the start [21]. The argument is that initially large errors are present and the accuracy of the inner iterations is wasted on these large errors. Another run applied the inner iterations only after the first 2000 time steps were run. Figure 2.c is a composite of two different trials. The first trial began the inner iterations immediately (time steps 0-2000). The second trial used no inner iterations until after the 2000th time step. The sharp increase in Figure 2.c at the 2000 mark indicates where the two trials are joined; it also highlights the tiny advantage gained by using the inner iterations over the first 2000 time steps. After time steps 2000-3000 were run, there was still no significant improvement.

There is a downward slope between time steps 2000-3000, which warrants further investigation. To investigate whether or not three inner iterations were enough to reduce the AF splitting error, another trial was run. Figure 2.d is a composite of three runs. In the first trial, three inner iterations per time step were run from the first time step to the 2000th time step; there was little improvement over using no inner iterations. The second case applied three inner iterations per time step after 2000 time steps were run without inner iterations. Figure 2.d shows a sharp increase at 2000 time

steps, which indicates the applications of inner iterations. Another 3000 time steps, with three inner iterations each, still showed no significant improvements. The third trial applied the inner iterations after 5000 time steps were run; the slope in the residual curve is quite steep, indicating rapid convergence.

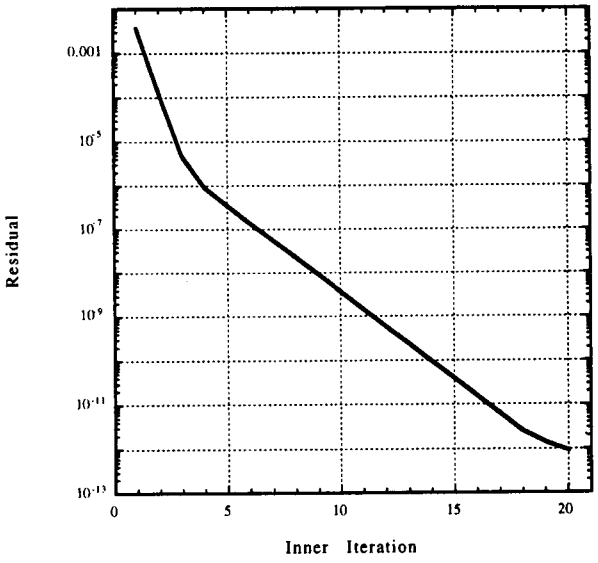
At this point two options were considered; the inner iteration implementation could be wrong, or the code itself could have a flaw preventing convergence. Both options were investigated.

The point of inner iterations is to reduce the AF splitting error. Figure 3.a shows the convergence of 20 inner iterations approaching machine zero. It appears that the inner iterations are converging correctly, but they are having no effect on converging the time step residuals as shown is Figure 3.b. It is possible that no steady state exists.

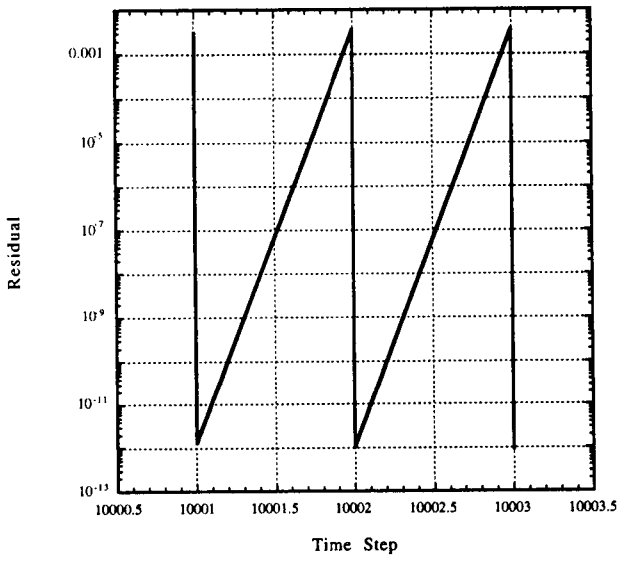
To test whether or not there was a fault in the code itself, the code was applied to another rocket, one with no slot. The residual convergence on the non-slotted rocket is shown in Figure 4. The sharp decrease in residuals to near machine zero indicates the code was working very well.

Pressure Wave

Both the code and the inner iterations algorithm appeared to be working correctly. The source of the disturbance was yet to be identified.



a.) Inner Iterations vs. Convergence.



b.) Regular Time Steps (with inner iterations) vs. Convergence.

Figure 3. Residual Convergence of Inner Iterations.

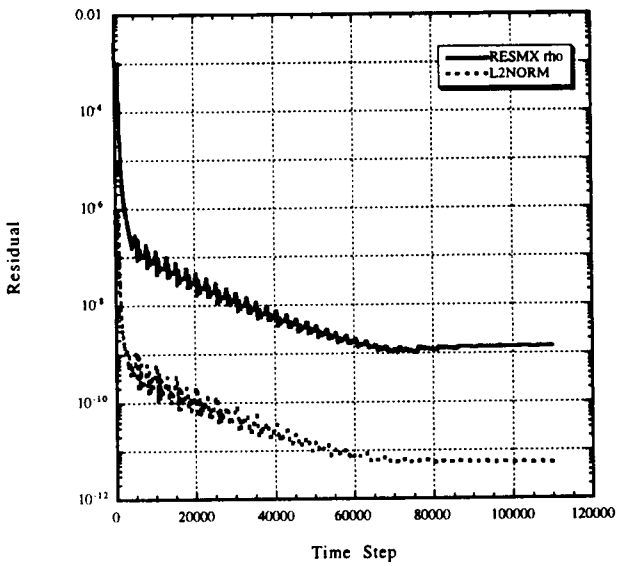
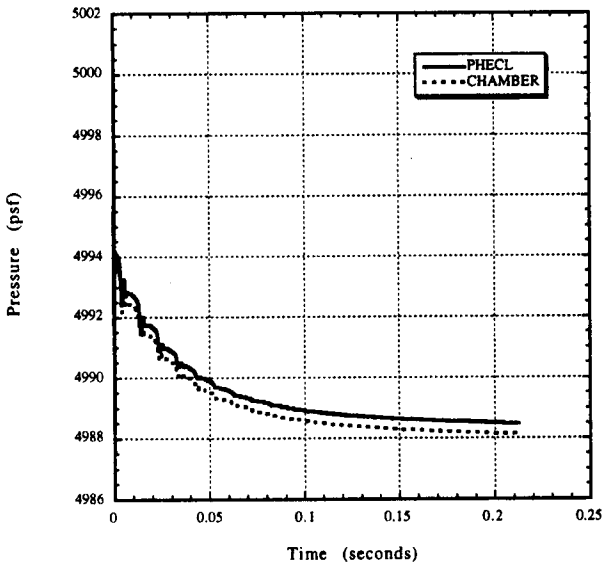


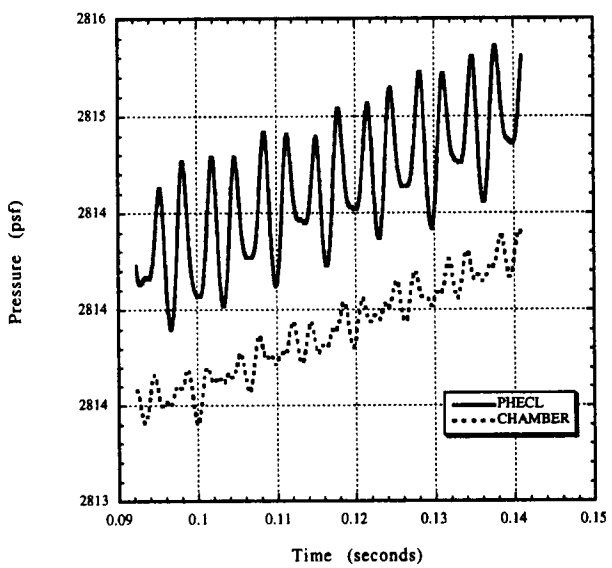
Figure 4. Residual Convergence for the Non-slotted Rocket. Non-driven Conditions, Second Order Time Accuracy.

Based on findings of Smith *et al.*, a good hypothesis was that the lack of convergence was related to pressure oscillations in the chamber. Looking first at the non-slotted rocket, Figure 5.a shows a continual pressure drop in the chamber at two centerline locations. Pressure traces at the head end, centerline, and in the chamber at non-dimensional axial distance X/D = 1.82, show very little periodic behavior.

The situation is much different when the slot is present, even when the system is not being driven. Under "steady" conditions, a pressure wave can be seen in Figure 5.b. Although the amplitude of this wave is small, it is still very significant. Since the term "steady"

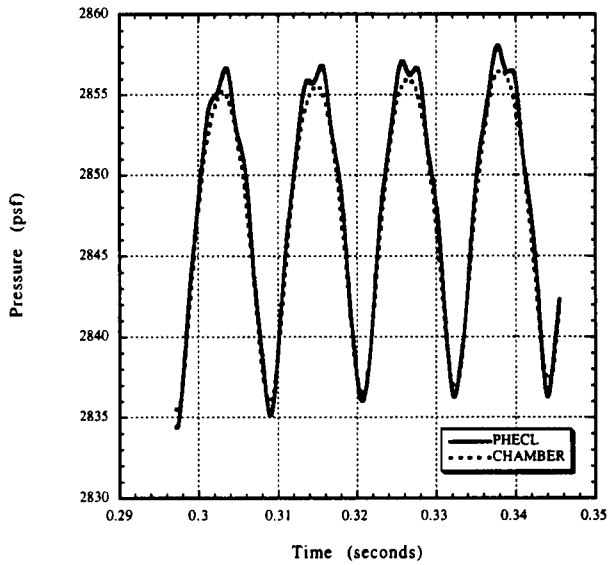


a.) Non-slotted Rocket, Non-driven Conditions,
Second Order Time Accuracy.

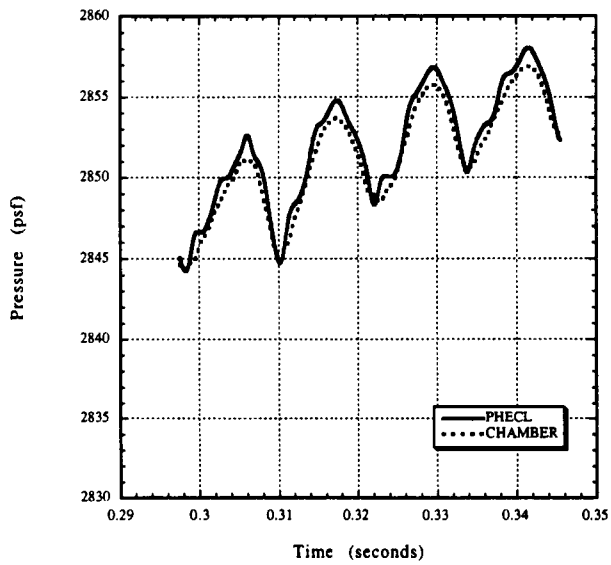


b.) Slotted Rocket, Non-driven Conditions,
Second Order Time Accuracy.

Figure 5. Pressure Profiles for the Two Rockets at the Head End and in the Chamber at X/D = 1.8.

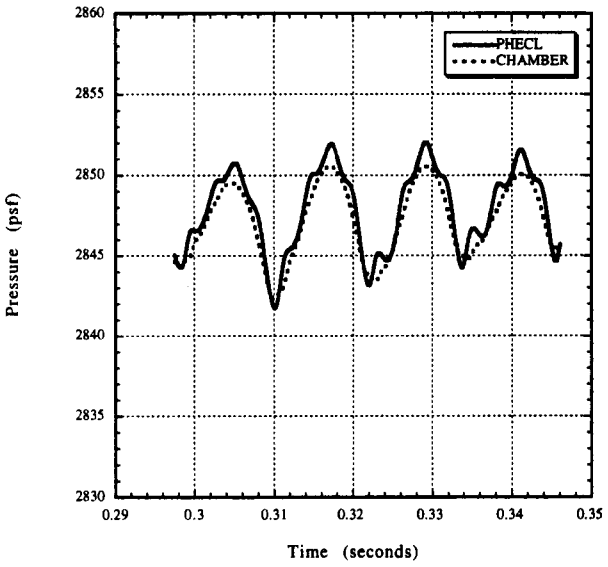


c.) Slotted Rocket, Driven Conditions, First Order Time Accuracy.

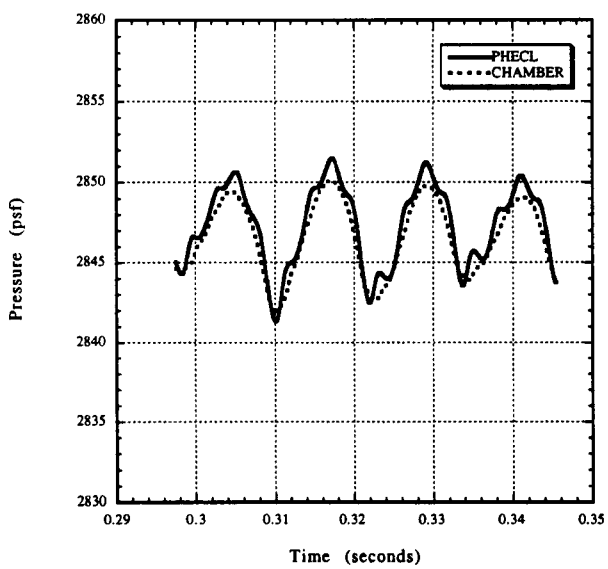


d.) Slotted Rocket, Driven Conditions,
Second Order Time Accuracy, Re*=1,000,000.

Figure 5. (continued).



e.) Slotted Rocket, Driven Conditions,
Second Order Time Accuracy, Re*=5,000,000.



f.) Slotted Rocket, Driven Conditions,
Second Order Time Accuracy, Re*=10,000,000.

Figure 5. (continued).

does not apply, all references will now be made to driven and non-driven conditions.

The lack of residual convergence is the starting point for further investigation. Having established the slot as the source of the instability, all driven trials were run exclusively on the slotted rocket. Variables studied under the driven conditions included: first and second time accuracy, and three different Reynolds' numbers. Figure 5.(b-f), traces the pressure wave in the slotted rocket under these different conditions. Notice that the largest pressure amplitude occurs under first order time accuracy conditions. Since the damping that occurs with second order time accuracy is less that with first order, second order plots should have the largest amplitude.

The Reynolds number used in Smith *et al.* (Re* = 5,000,000) was dimensionalized with respect to one foot [1]. Table 1. lists the dimensional and corresponding non-dimensional numbers used in this study.

Table 1. Reynolds' Numbers

Re (dimensional WRT 1 foot)*	*Re (non-dimensional equivalent)*
1,000,000	166,666
5,000,000	833,333
10,000,000	1,666,667

The pressure at the head end, centerline, continued to rise during the study (see Figure 6). It was expected that the pressure would level off and oscillate at a mean value.

Initially, the mass flux off of the surface is greater than the mass flux at the throat. The mass balance should quickly come to an equilibrium, with mass flux from the surface equal to the mass flux at the throat. To discover if a mass accumulation in the chamber was responsible for the pressure increase, the momentum flux at the throat was plotted in Figure 7. The momentum flux quickly levels off at a value which indicates that there is not a mass build up in the chamber. The increase in the pressure at the head end centerline cannot be attributed to the momentum flux.

Standing Wave

Driving the slotted rocket created a standing pressure wave along the centerline in the chamber. The amplitude of a pressure

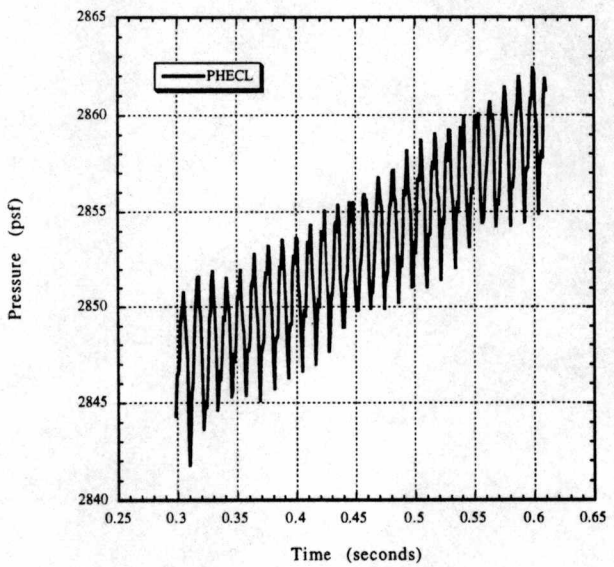


Figure 6. Continuous Increase in Pressure at the Head End Centerline.

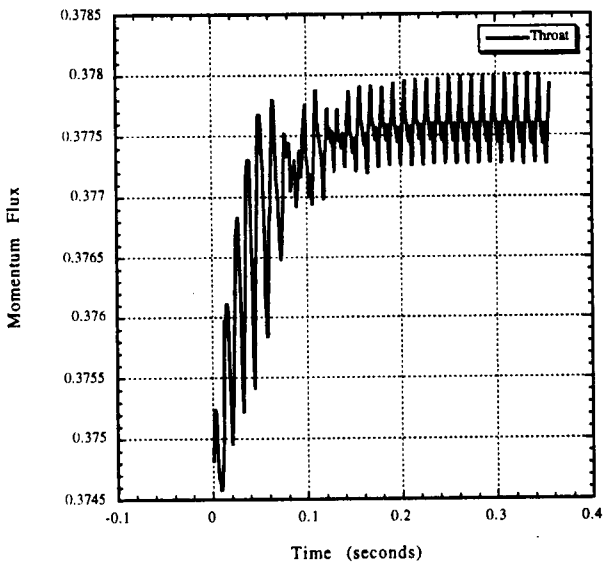
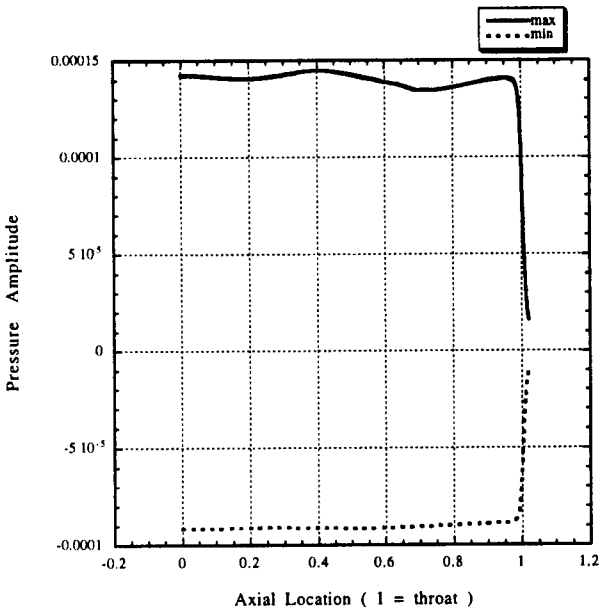
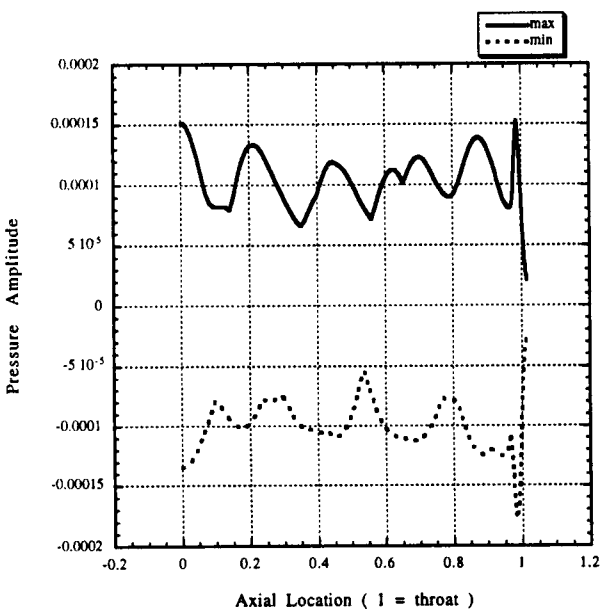


Figure 7. Momentum Flux at the Throat Levels Off.

wave versus axial chamber position, is shown in Figure 8.(a-d) under the following conditions: in the non-slotted rocket, in the slotted rocket with second order time accuracy and non-driven conditions, in the slotted rocket with first order time accuracy and driven conditions, and in the slotted rocket with second order time accuracy and driven conditions, respectively. In the non-slotted rocket, the pressure amplitude is fairly constant through out the chamber (Figure 8.a). Under non-driven conditions in the slotted rocket the amplitude shows huge variation with axial position (Figure 8.b). Notice the node halfway down the axis and the anti-nodes at the head and aft ends when the slotted rocket is driven (Figure 8. c & d). Figure 8.c clearly shows a standing wave; a similar wave form was

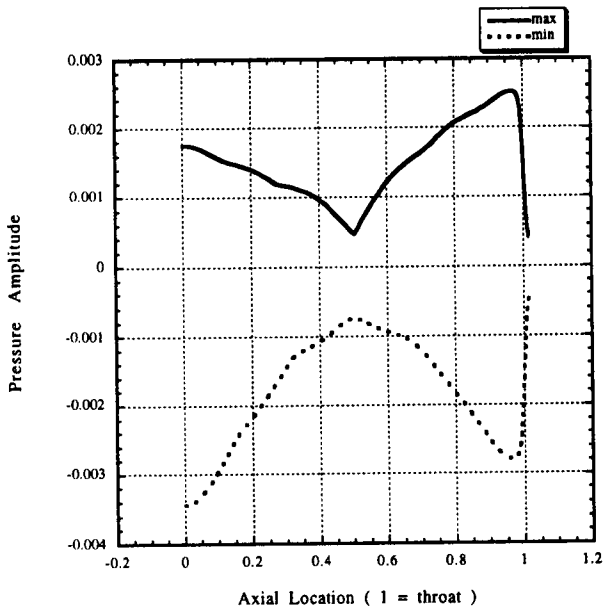


a.) Non-slotted rocket, Non-driven Conditions,
Second Order Time Accuracy.

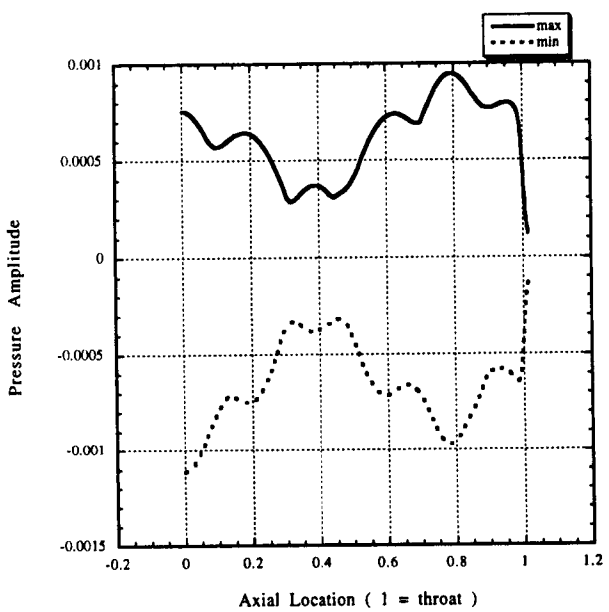


b.) Slotted Rocket, Non-driven Conditions,
Second Order Time Accuracy.

Figure 8. Pressure Wave Amplitudes in the Two Rockets.



c.) Slotted Rocket., Driven Conditions, First Order Time Accuracy.



d.) Slotted Rocket, Driven Conditions, Second Order Time Accuracy.

Figure 8. (continued).

expected in Figure 8.d. The disturbances in the wave form in the latter figure may indicate a problem in the second order time accuracy algorithm or the affects of slot disturbances. Results of the Dotson study showed a perfect sinusoidal wave form in a rocket that did not have a slot [22].

Frequency of Oscillation

A Fast Fourier Transform (FFT) was done on the non-driven conditions pressure wave. The frequency of the wave was 85 Hz, which corresponds to the natural frequency of the rocket chamber; second, third, and fourth harmonics were also present. For all driven trials, 85 Hz was chosen as the driving frequency.

The pressure wave affects the velocity profile. A typical velocity profile is displayed in Figure 9. A FFT of the velocity data indicates that the wave frequency is 85 Hz, and that other harmonic frequencies are present.

A FFT was also used to compare frequencies and phase angles of the pressure and velocity data in each rocket at various locations. Pressure data was sampled at the head end centerline, at five locations along the centerline, and at the burning surface. Velocity data was sampled at the same five locations along the centerline and burning surface as the pressure data. Velocity was not sampled at the head end centerline since the no slip boundary condition dictates that velocity is zero at the head end.

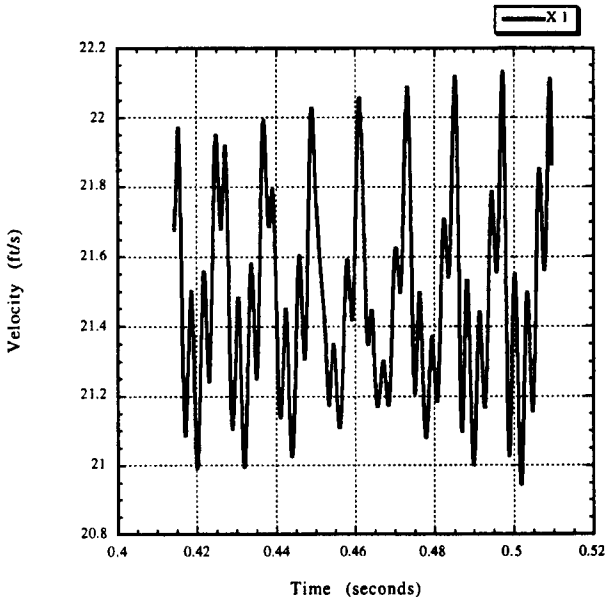
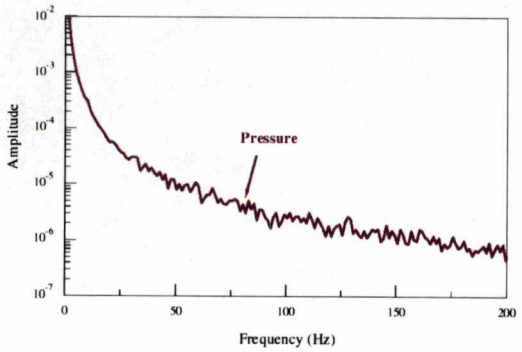
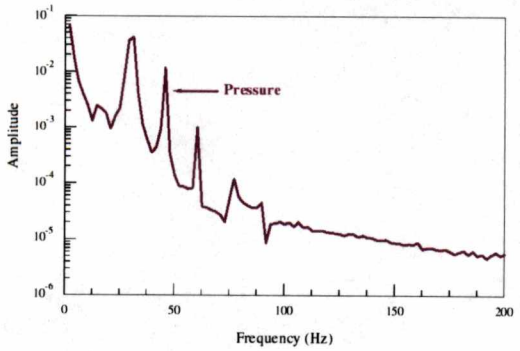


Figure 9. Typical Velocity Trace from Chamber Location X/D = 1.8.

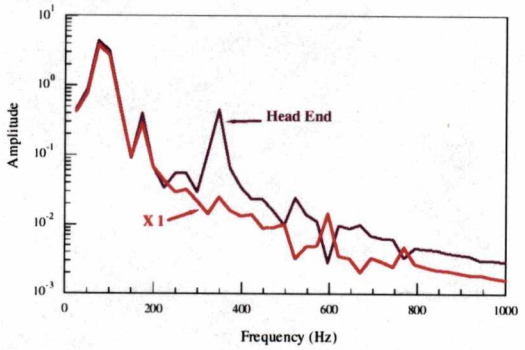
Figure 10.(a-p) shows the results for the FFT of data from various trials. Figure 10.a shows the FFT of the pressure in the non-slotted rocket; no wave is present in the chamber. Under non-driven conditions in the slotted rocket, a pressure wave of low amplitude is present; one of the peaks in Figure 10.b is at the expected frequency of 85 Hz. Note that all of the peaks in this figure have very small amplitudes. The signal was very weak, therefore it was necessary to first use a linear extrapolation on the data. Overall, the mean pressure rose in the rocket chamber (refer to Figure 5); the linear extrapolation was used to remove the average pressure increase from the data before it was analyzed.



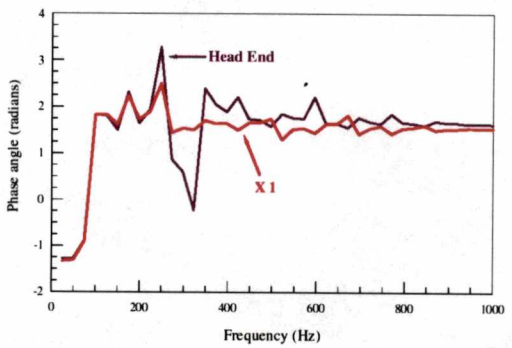
(a) Non-slotted Rocket, Non-driven Conditions



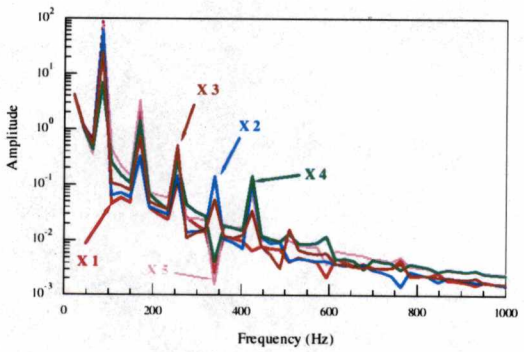
(b) Slotted Rocket, Driven Conditions



(c) Centerline Pressure

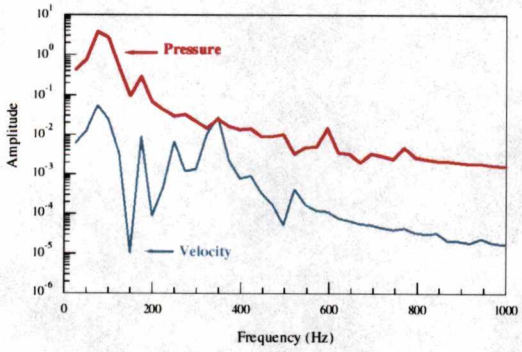


(d) Centerline Pressure

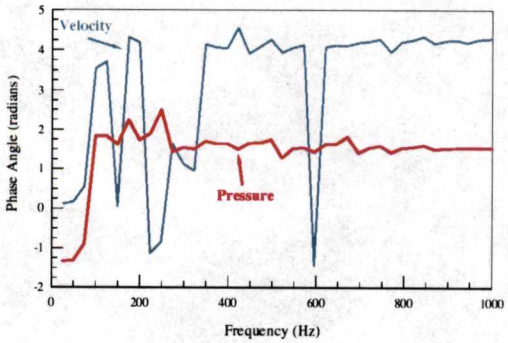


(e) Centerline Pressure at five locations

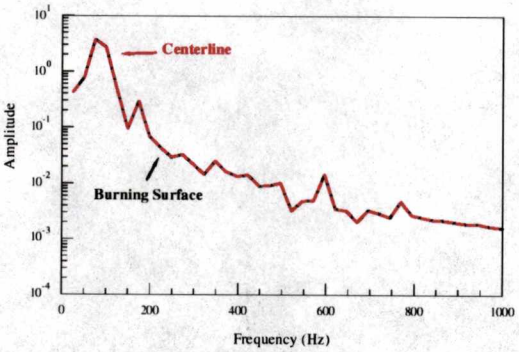
Figure 10. Amplitude and phase distributions for selected pressure and velocity computations. Conditions for (C–P) are Slotted Rocket, Driven Conditions.



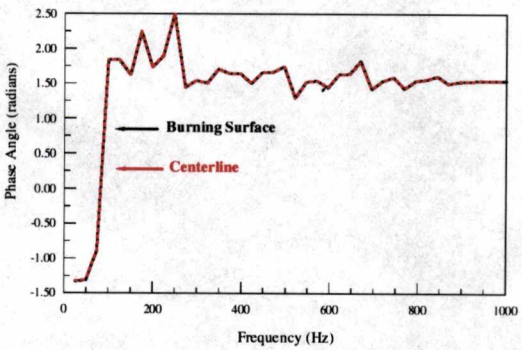
(f) Centerline



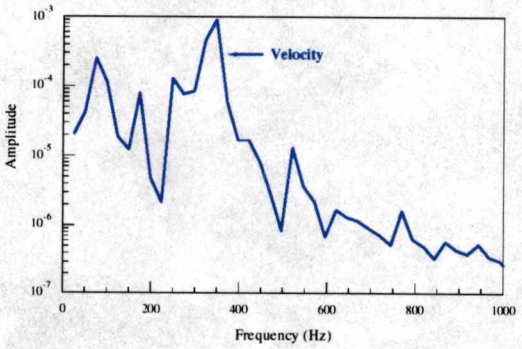
(g) Centerline



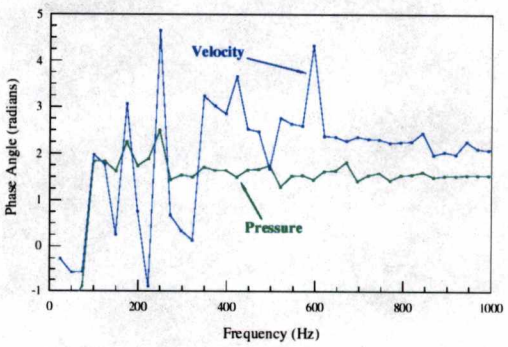
(h) Pressure at X1



(i) Pressure at X1

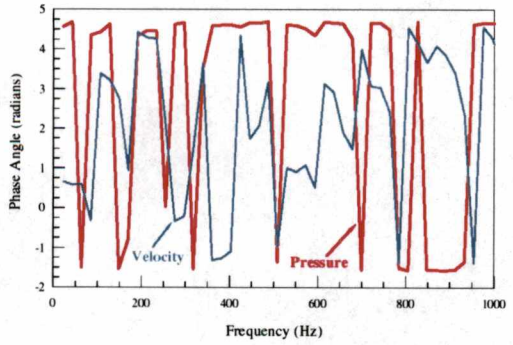


(j) Burning Surface at X1

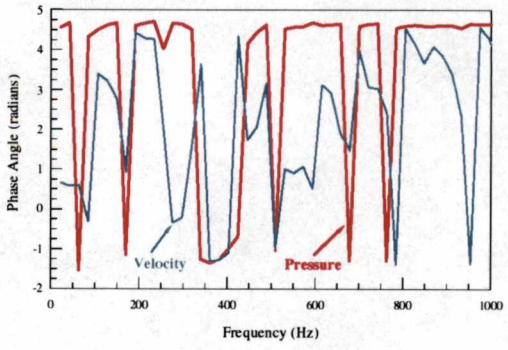


(k) Burning Surface at X1

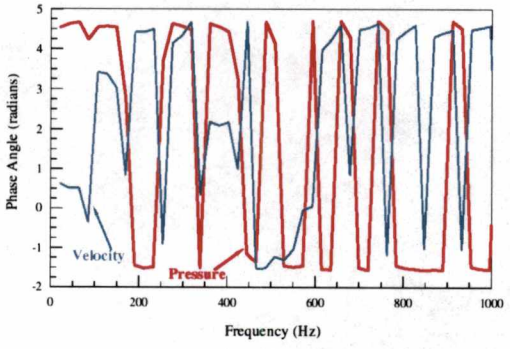
Figure 10. (continued).



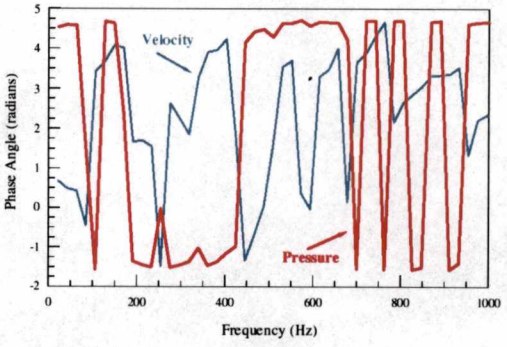
(l) Centerline at X1



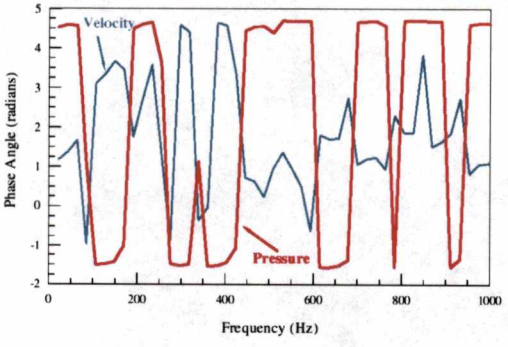
(m) Centerline at X2



(n) Centerline at X3



(o) Centerline at X4



(p) Centerline at X5

Figure 10. (continued).

The trials in Figure 10.c to Figure 10.p were all run with driven conditions in the slotted rocket. Figure 10.c shows the frequency of the pressure wave at two axial locations in the chamber, one at the head end, the other 9% of the chamber length away from the head end. The largest amplitude occurs at the head end at 85 Hz; this was expected, since an anti-node occurs at the head end. Note these amplitudes are much larger than under non-driven conditions. Other peaks occur around the frequencies of 170 Hz, 255 Hz, and 340 Hz, corresponding to the second, third, and fourth harmonics. Around 500 Hz, the two curves become almost mirror images of each other; this phenomenon will be discussed shortly.

Figure 10.d displays the phase angle of the pressure wave at the head end and in the chamber. The curves are in phase at the second and third harmonics. That the first harmonic does not appear is attributed to a resolution problem.

To look more closely at what happens along the centerline in the chamber, Figure 10.e plots five axial centerline locations. The locations are all non-dimensionalized by chamber length over chamber diameter. The axial locations were chosen to correspond to Smith *et al.* [1]; Table 2 lists the five locations. In Figure 10.e, the peaks are congruent over the first three harmonics. Beyond 300 Hz, the peaks are no longer in agreement. The incongruent peaks are attributed to noise.

The velocity wave responds to the pressure wave; Figure 10.f and Figure 10.g show the response. The velocity FFT manifests the

Table 2. Axial Locations

Axial Location	*Non-dimensional Distance*	*% of Chamber Length WRT Head End*
X1	1.8	9%
X2	4.22	22%
X3	6.64	34%
X4	11.5	60%
X5	17.6	92%

first four harmonics. Figure 10.g indicates that the pressure and velocity at 100 Hz are out of phase by 1.75 radians (approximately 100 degrees). Most stability models assume the velocity and pressure are out of phase by 90 degrees. [1] The data sample used in this FFT included 20,000 time steps. One cycle of oscillation requires over 12,000 time steps at 85 Hz. The discrepancy between the current results and stability models is attributed to a resolution error, thus more analyses were performed using data sampled over 50,000 time steps (or approximately four oscillations). The results from the additional runs will be discussed after the results from the burning surface.

The pressure at the centerline and at the burning surface match in both amplitude and phase, as shown in Figure 10. h & i. Figure 10.j shows the axial velocity amplitude at the burning surface with the expected harmonic peaks. The phase angle in Figure 10.k,

between the pressure and the pressure and velocity at the burning surface, is very small. This is a very significant result which is not predicted by linear theory, but it is in agreement with other analytical and experimental results. [1,2,4]

Figure 10.(l-p), presents the results of trials performed to check the resolution error in Figure 10.g. A FFT will not detect low frequencies when too few cycles are analyzed; this may be the reason that a peak does not appear at 85 Hz in Figure 10.g. At axial locations X1-X4 at 85 Hz, the velocity and pressure are out of phase by approximately 4.75 radians (270 degrees). Note the relative positions of the pressure and velocity lines in Figure 10.g and Figure 10.l - in the first figure the velocity has a higher phase angle than the pressure, and vise versa in the second figure. This shows that the plots are consistent; the velocity and pressure are out of phase in the same direction. The difference in phase angle in Figure 10.p is 5.25 radians (300 degrees). The proximity of X5 to the slot could account for the deviation in phase angle from the expected 90 degrees.

Vorticity

It is apparent that the presence of the slot is causing pressure oscillations. What are the phenomena associated with the slot that cause oscillations? Is the effect important in real SRMs?

The pressure wave in the chamber is caused by the periodic vortex shedding in the slot. The vortices are the result of flow

turning and shear flow affects. Flow is injected normal to the wall, which satisfies the no slip condition as axial velocity along the wall is zero. The flow off the burning surface is entirely radial. At the centerline the flow is completely axial, and in between both radial and axial components are present, although the dominant flow is longitudinal. The mean flow, as well as the oscillatory flow, is necessarily rotational to accomplish the transition from the burning surface to nozzle outflow.

Flandro's analysis shows that the dominant cause of vortices can be traced to the flow turning effect [4,5]. Viscosity effects are much smaller. Another interesting result related to the oscillatory motion is the variation in the axial velocity amplitude as a function of radial location. Depending on the axial location, at some spots, the amplitude near the burning surface is twice the amplitude at the center [1]. The small phase angle and large amplitude at the burning surface are quite different than the plane wave model on which most stability assessments are based.

Brown [6] drew several conclusions from his work, two are especially significant to the current work.

(1). The oscillatory wave motion does not alter the mean velocity.

(2). Oscillatory vorticity is significant and has an important role in determining how the oscillatory flow at the surface transitions to axial acoustic wave motion.

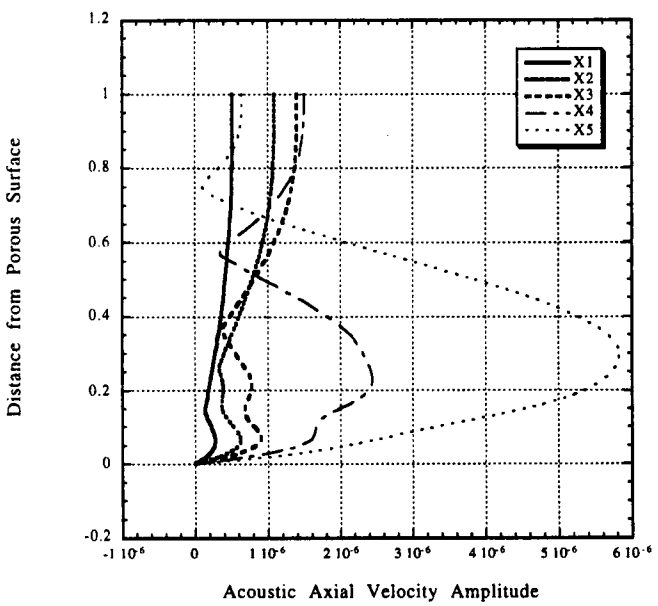
A real SRM may have segment corners or inhibitor rings with sharp corners that, at some point, protrude into the SRM's flow. The

sharp corner at the entrance to the slot is an analogous protrusion in the flow field.

The sharp corner is the source of a vortex. This vortex is the source of the pressure and velocity fluctuations. Snapshots of pressure contours, velocity magnitude contours, and velocity vectors, show the movement of the vortex in the slot. Data samples were taken 20 times during on cycle of oscillation. From these samples, pressure contour, velocity magnitude contour, and velocity vector plots were made at 10 points in the cycle. In particular, the velocity magnitude plots appear to show the formation of vortices near the corner, the progression of the vortices during one cycle of oscillation, and finally the shedding of the vortices and their absorption by the nozzle. In the Appendices, Figures A-A.(1-10) are a series of pressure contours, Figures A-B.(1-10) are a series of velocity magnitude contours, Figures A-C.(1-10) are a series of velocity magnitude contours, and Figures A-D.(1-10) are a series of velocity vector plots. All of the figures are taken from snapshots of the flow field at 20 different times during one cycle of oscillation.

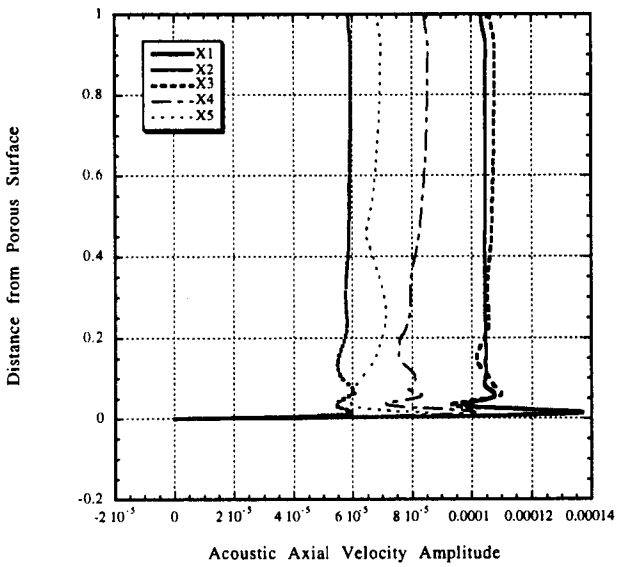
The oscillatory behavior of the acoustic velocity profile is shown in Figure 11.(a-f). In the non-slotted rocket, the acoustic velocity amplitude is very small and shows little variation with radial location. In the slotted rocket, when no driving function is applied, a small variation in axial velocity amplitude with radial location occurs. The variation becomes large under driven conditions. Figure 11.(c-f) traces driven conditions under different orders of time accuracy and viscosity. Figure 11.(c-f) also shows a

marked improvement from previous work [1]. The implicit centerline boundary condition has completely eliminated the lag at the centerline. Improvements in time accuracy allow more oscillations to be traced, thus coming closer to the analytical solution.

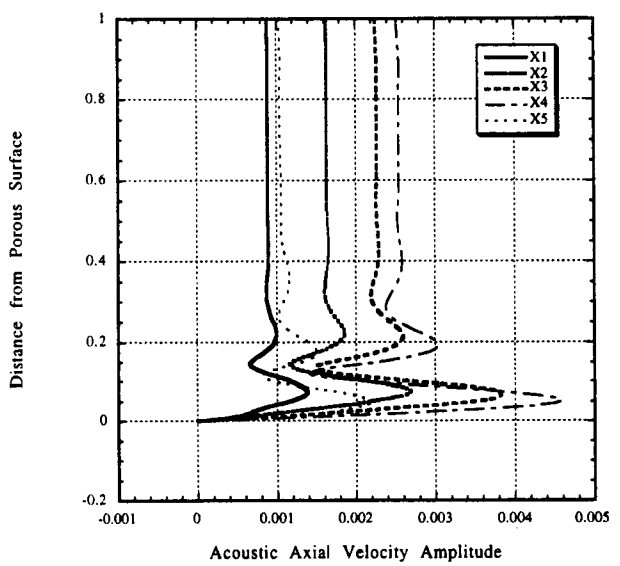


a.) Non-Slotted Rocket, Non-driven Conditions,
Second Order Time Accuracy.

Figure 11. Axial Velocity Profiles of the Two Rockets.

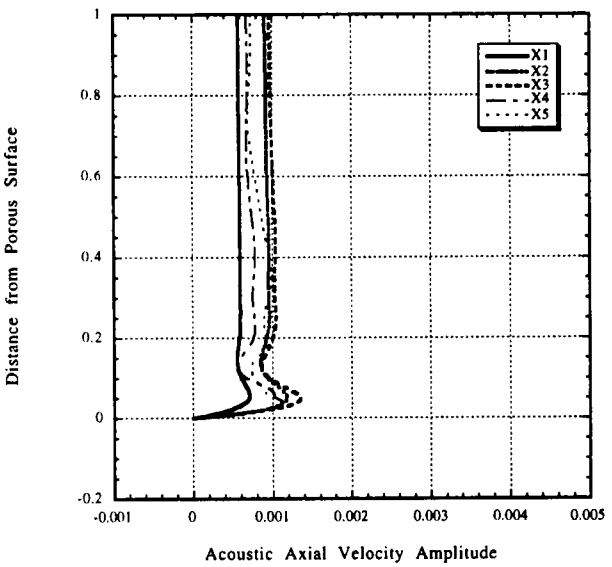


b.) Slotted Rocket, Driven Conditions, Second Order Time Accuracy.

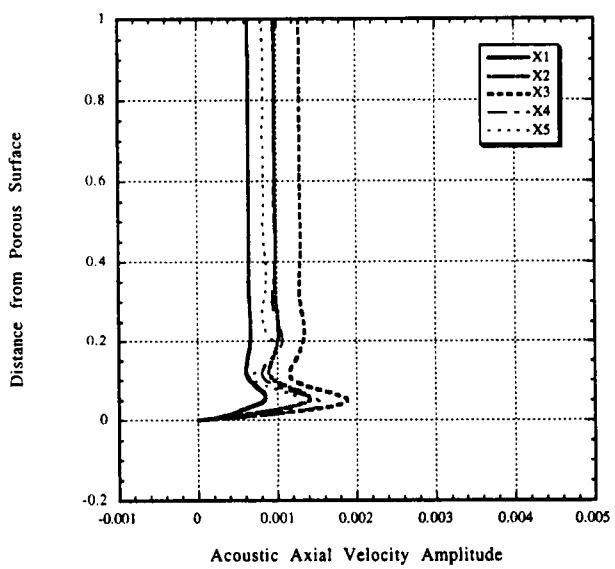


c.) Slotted Rocket, Driven Conditions, First Order Time Accuracy.

Figure 11. (continued).

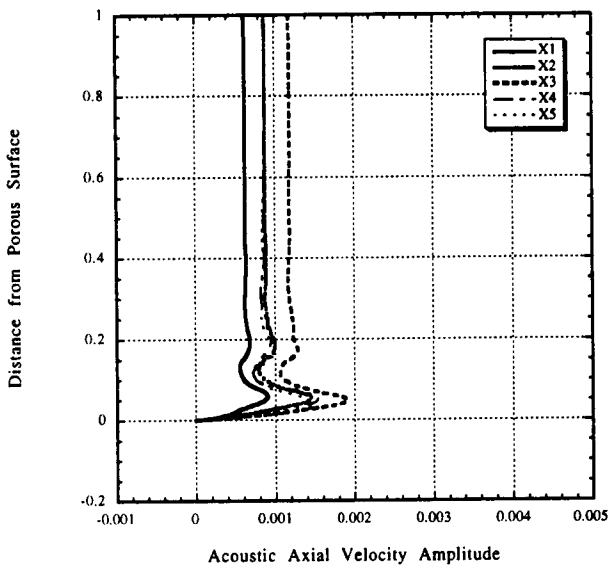


d.) Slotted Rocket, Driven Conditions,
Second Order Time Accuracy, Re*=1,000,000.



e.) Slotted Rocket, Driven Conditions,
Second Order Time Accuracy, Re*=5,000,000.

Figure 11. (continued).



f.) Slotted Rocket, Driven Conditions,
Second Order Time Accuracy, Re*=10,000,000.

Figure 11. (continued).

Chapter 7

CONCLUSIONS AND RECOMMENDATIONS

Although the results presented here are similar to analytical and experimental results, all the numerical results suffer from damping effects. For example, in the plots of the axial velocity profiles versus radial location, numerical results show that the disturbance extends 40% of the radial distance from the burning surface. By comparison, analytical and experimental results show the disturbance extending 60% of the radial distance from the burning surface. By removing or lessening the numerical damping effects, the oscillations could extend beyond 40% of the radial distance.

Numerical errors that were examined in this thesis include space, time, AF algorithm, and boundary condition errors. Some improvement was made in the time accuracy and in the AF algorithm, but the time accuracy implementation requires more study. No progress was made in improving the spatial accuracy of the code or in developing a new burning surface boundary condition. Results presented on the implicit centerline boundary condition show an improvement over previous efforts [1,2].

The grid used in this investigation has a high cell aspect ratio, especially near the burning surface. This may cause problems for two separate reasons. In trying to implement a new burning surface boundary condition, it was necessary to integrate along the burning

surface in the axial direction. The large grid spacing in the axial direction may have contributed to the round off error problems encountered with the new burning surface boundary condition. A large aspect ratio may lead to spurious solutions [22], a phenomenon that was not investigated in this thesis.

Future investigations may want to look at higher harmonic frequencies. To achieve proper resolution for a FFT, an appropriate combination of CFL and grid size is required. The combination used in this thesis focused on the natural frequency of 85 Hz. Care must be taken to satisfy Nyquist criterion at higher frequencies [22].

Despite the numerical errors present in the approximate solution, results similar to analytical and experimental results indicate that it is capturing some subtle aspects of the flow field. These results, especially the phase angle between the pressure and velocity at the burning surface, and the axial velocity profiles, indicate that the current linear stability model is inadequate. More attention needs to be given to surface effects, such as flow turning as a source of vorticity.

REFERENCES

REFERENCES

1. Smith, T.M., Roach, R.L., and Flandro, G.A., "Numerical Study of the Unsteady Flow in a Simulated Solid Rocket Motor," AIAA Paper 93-0112, June 1993.
2. Flandro, G.A., Roach, R.L., and Smith, T.M., "Effects of Vorticity Transport on Combustion Instability," AIAA Paper 91-1673, June 1991.
3. Personal communication, R.L. Roach, June 1997.
4. Flandro, G.A., "Effects of Vorticity on Rocket Combustion Stability," *Journal of Propulsion and Power*, Vol. 11, No. 4, 1995, pp. 607-625.
5. Flandro, G.A., "On Flow Turning," AIAA Paper 95-2730, July 1995.
6. Brown, R.S., and Blackner, A.M., Willoughby, P.G., and Dunlap, R., "Coupling Between Velocity Oscillations and Solid Propellant Combustion," Final Report on Contracts F49620-81-C-0027 and F49620-84-c-0082, Chemical Systems Division, August 1986.
7. Kourta, A., and Soula, C., "Vortex Shedding in Solid Rocket Motors," AIAA Paper 95-0727, January 1995.
8. Anthoine, J., Olivari, D., Hulshoff, S., and Van Rooij, M., "Qualitative Model of Vortex Induced Oscillations in a Model of Solid Propellant Boosters," AIAA Paper 98-2270, June 1998.

9. Roh, T-S., Tseng, I-S., and Yang, V., "Effects of Acoustic Oscillations on Flame Dynamics of Homogeneous Propellants in Rocket Motors," *Journal of Propulsion and Power,* Vol. 11, No. 4, 1995, pp. 640-650.

10. Yang, V., Hsieh, K.C., and Tseng, I.S., "Velocity-Coupled flow Oscillations in a Simulated Solid-Propellant Rocket Environment," AIAA Paper 88-0543, January 1988.

11. Chang, I-S., Patel, N.R., and Yang,S., "Titan IV Motor Failure and Redesign Analyses," *Journal of Spacecraft and Rockets,* Vol. 32, No. 4, July-August 1995.

12. Flatau, A., and VanMoorhem, W., "Prediction of vortex Shedding Responses in Segmented Solid Rocket Motors," AIAA Paper 90-2073, July 1990.

13. Kourta, A., "Shear Layer Instability and Acoustic Interaction in Solid Propellant Rocket Motors," *International Journal for Numerical Methods in Fluids,* Vol. 25, 1997, pp. 973-981.

14. Anthoine, J., Planquart, P., and Olivari, D., "Cold Flow Investigations of the Flow Acoustic Coupling in Solid Propellant Boosters," AIAA Paper 98-0475, January 1998.

15. Baum, J.D., "Numerical Investigation of Energy Exchange Mechanisms Between the Mean and Acoustic Flow Fields in a Simulated Rocket Combustor," AIAA Paper 90-2310, AIAA/ASME/ASEE 26th Joint Propulsion Conference, July 1990, Orlando Fl.

16. Kassoy, D.R., Kirkkopru, K., and Zhao, Q., "Nonlinear Acoustic Processes in a Solid Rocket Engine," Air Force Office of Scientific Research Technical Report. Grant No. AFOSR-89-0023. March 1994.

17. Vuillot, F., and Avalon, G., "Acoustic Boundary Layers in Solid Propellant Rocket Motors Using Navier-Stokes Equations," *Journal of Propulsion,* Vol. 7, No. 2, March-April 1991.

18. Personal communication, G.A. Flandro, June 1998.

19. Roach, R.L., "Inner Iterations for Approximate Factorization Schemes," AE 599 CFD Class Notes.

20. Hirsch, C., Numerical Computation of Internal and External Flows - Volume 2: Computational Methods for Inviscid and Viscous Flows, New York: Wiley.

21. Graveline, J.R.S., Quasi-Newton Iterations, Preconditioning, and Numerical Diffusion for a 4th-Order Operator Compact Compressible Navier-Stokes Solver, Master's Thesis, UTSI, Tullahoma, TN. August 1997.

22. Dotson, K.W., Koshingoe, S., and Pace, K.K., "Vortex Shedding in a Large Solid Rocket Motor Without Inhibitors at the Segment Interfaces," *Journal of Propulsion and Power,* Vol. 13, No. 2, 1997, pp. 197-206.

23. Personal communication, T. Moulden, November 1998.

APPENDICES

APPENDIX A

PRESSURE CONTOUR FIGURES

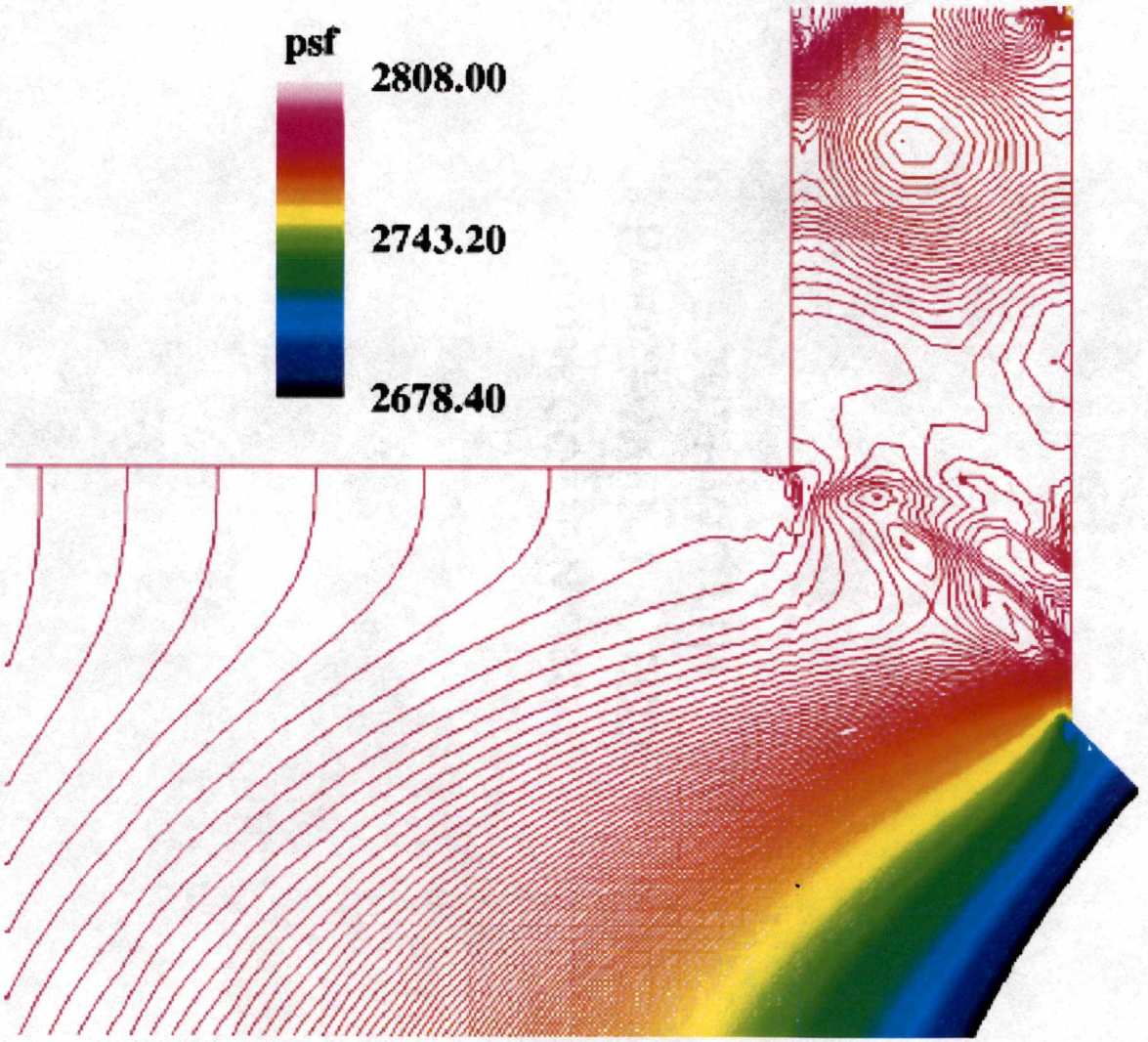


Figure A-A.1. Pressure contours at 1/10th of a cycle.

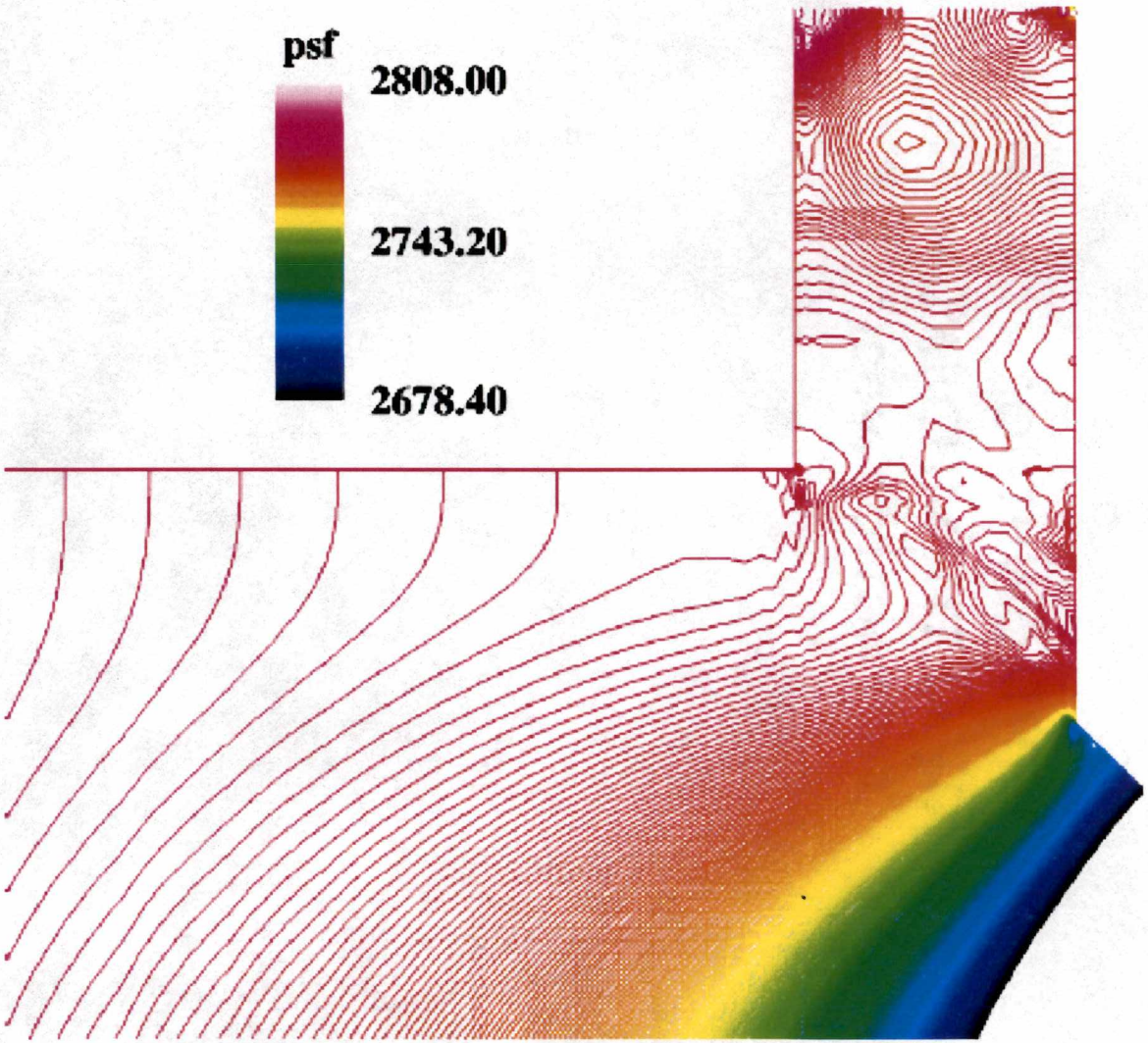


Figure A-A. 2. Pressure contours at 2/10th of a cycle.

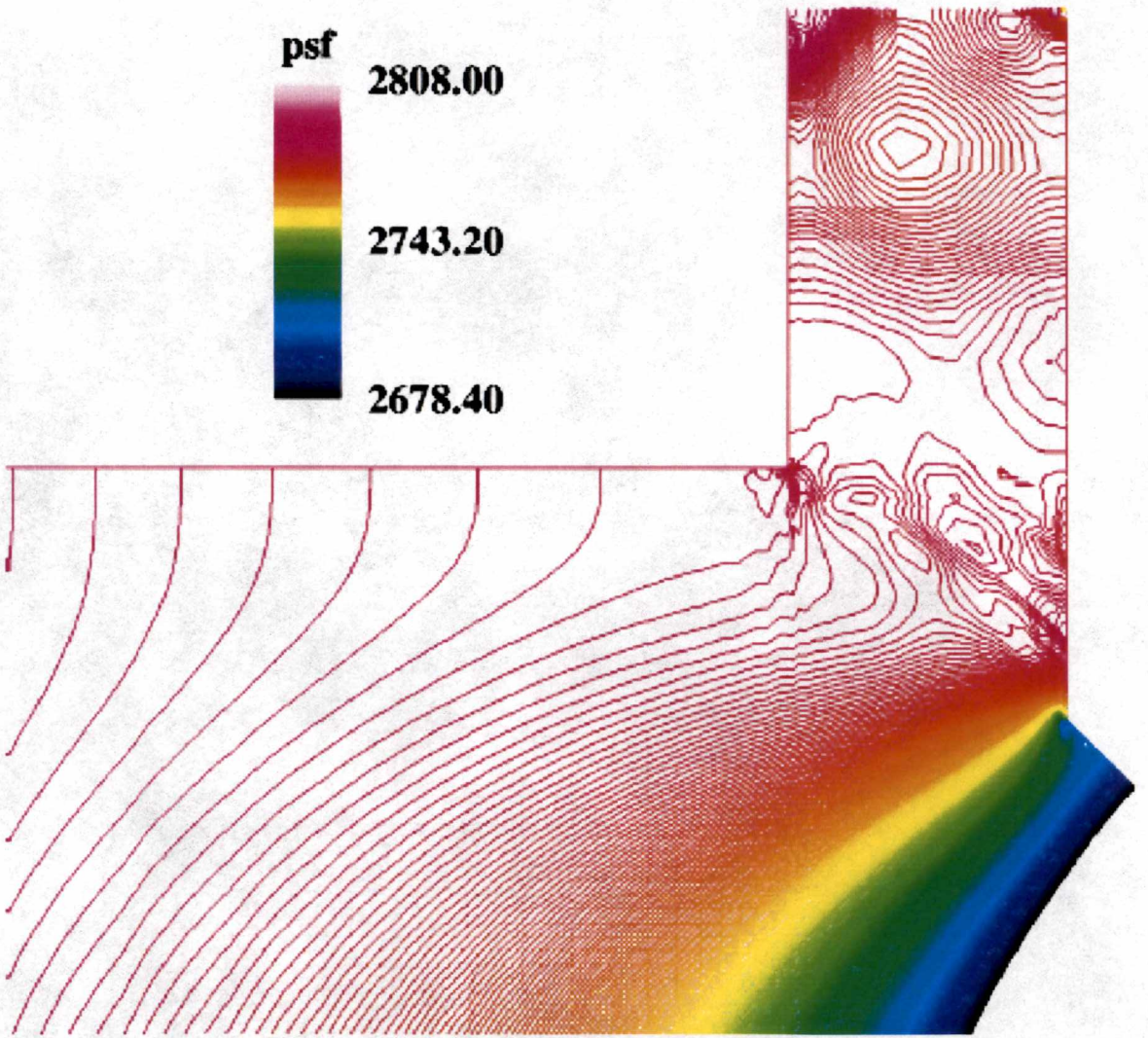


Figure A-A. 3. Pressure contours at 3/10th of a cycle.

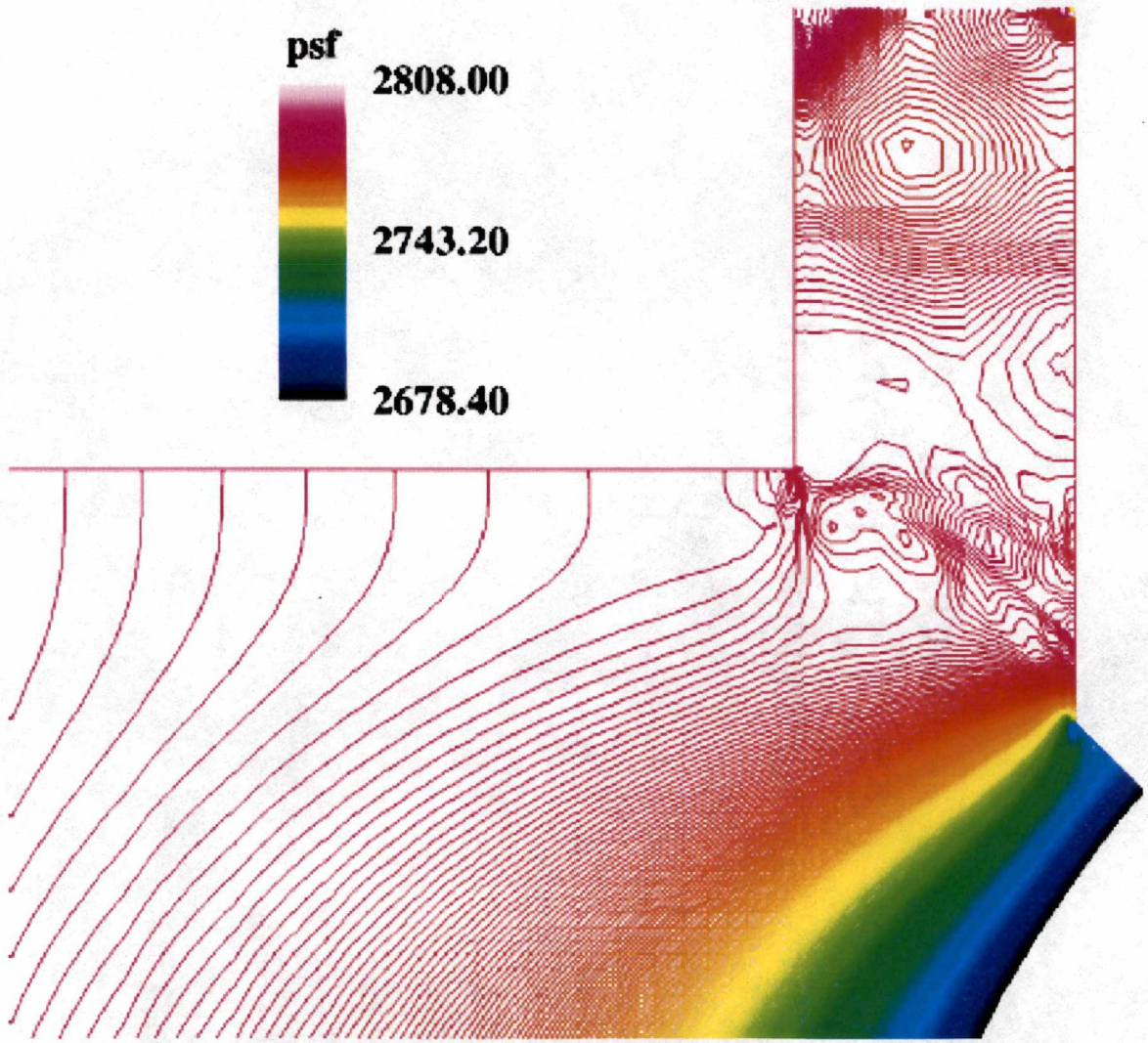


Figure A-A. 4. Pressure contours at 4/10th of a cycle.

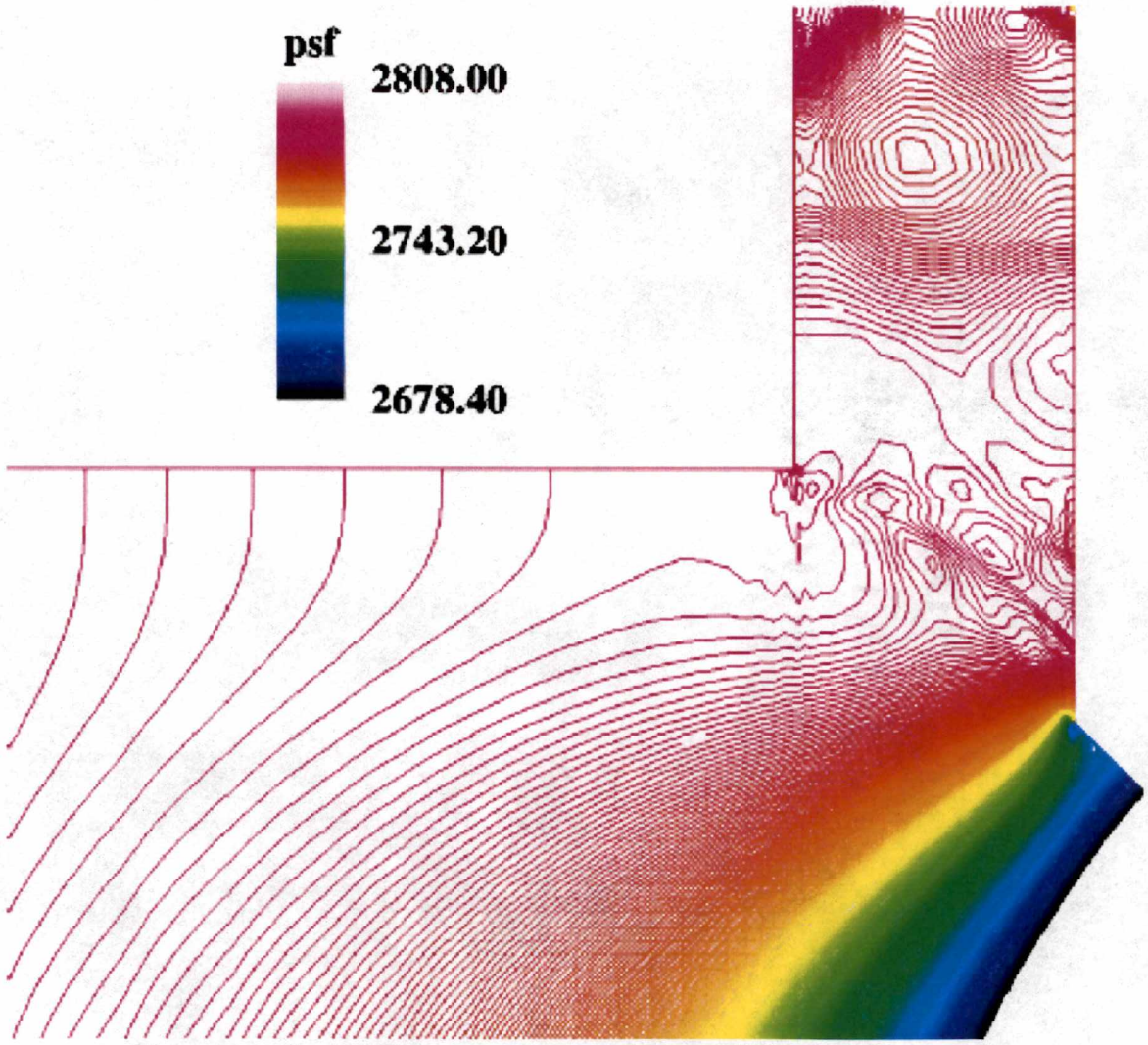


Figure A-A. 5. Pressure contours at 5/10th of a cycle.

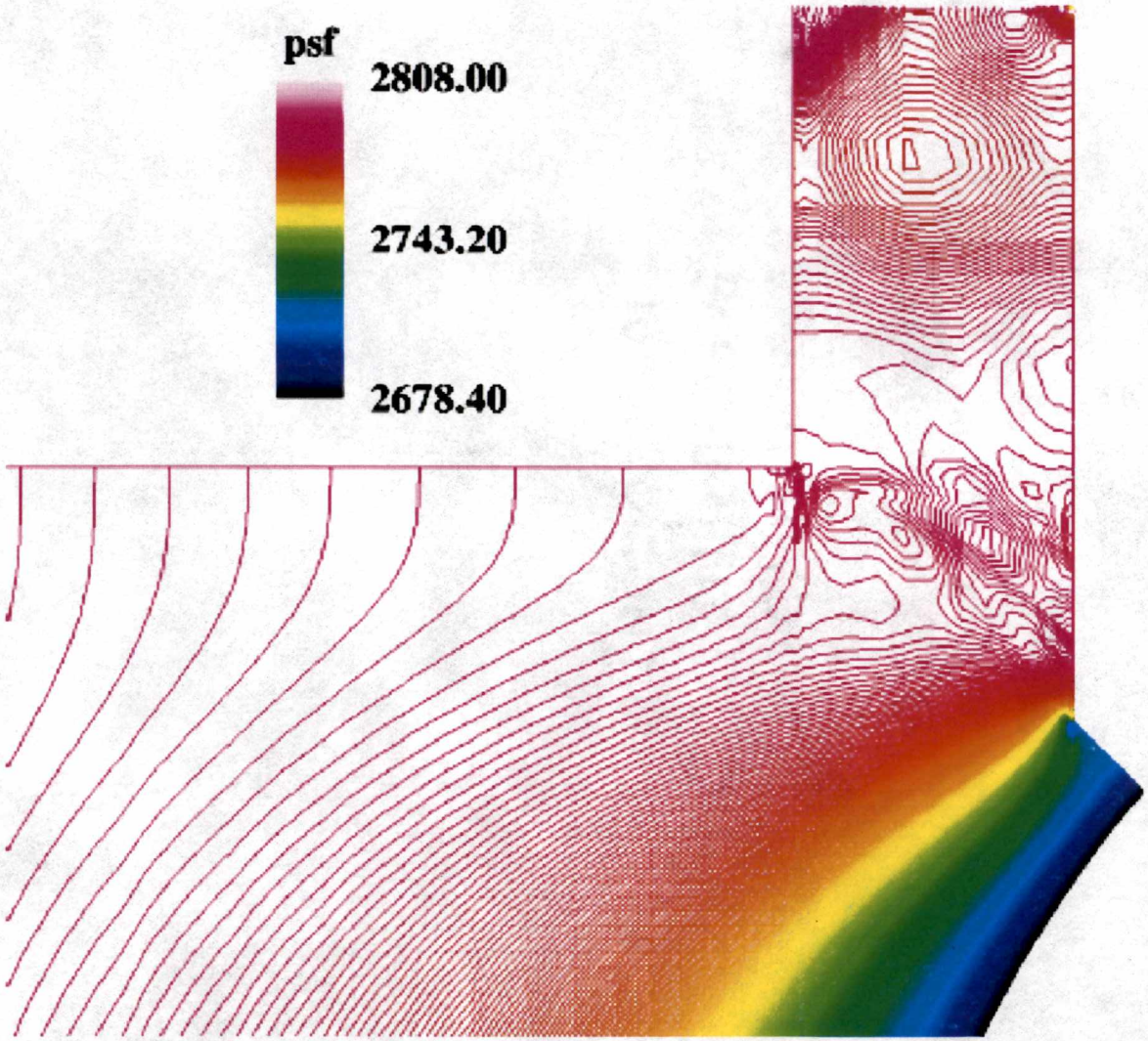


Figure A-A. 6. Pressure contours at 6/10th of a cycle.

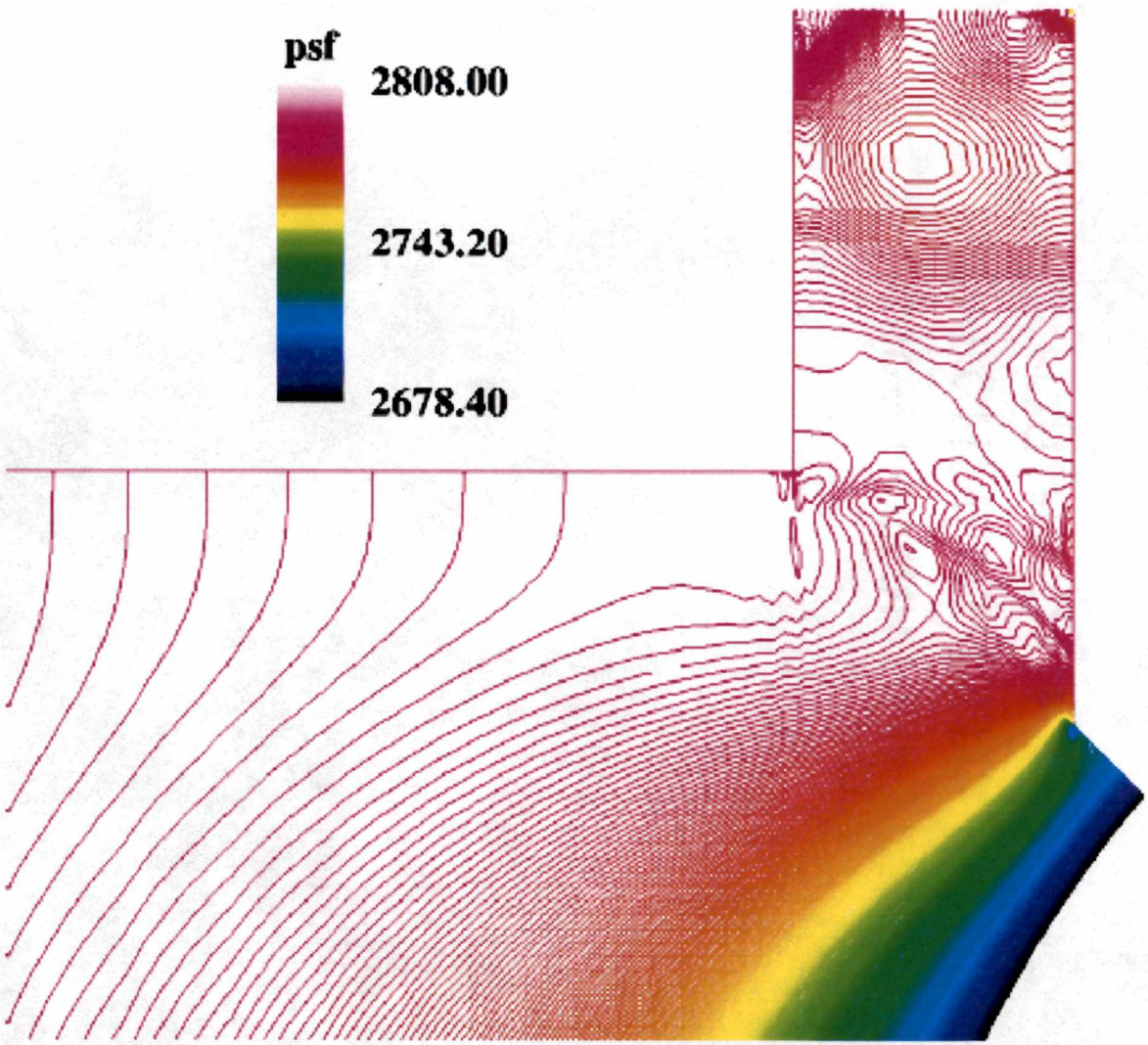


Figure A-A. 7. Pressure contours at 7/10th of a cycle.

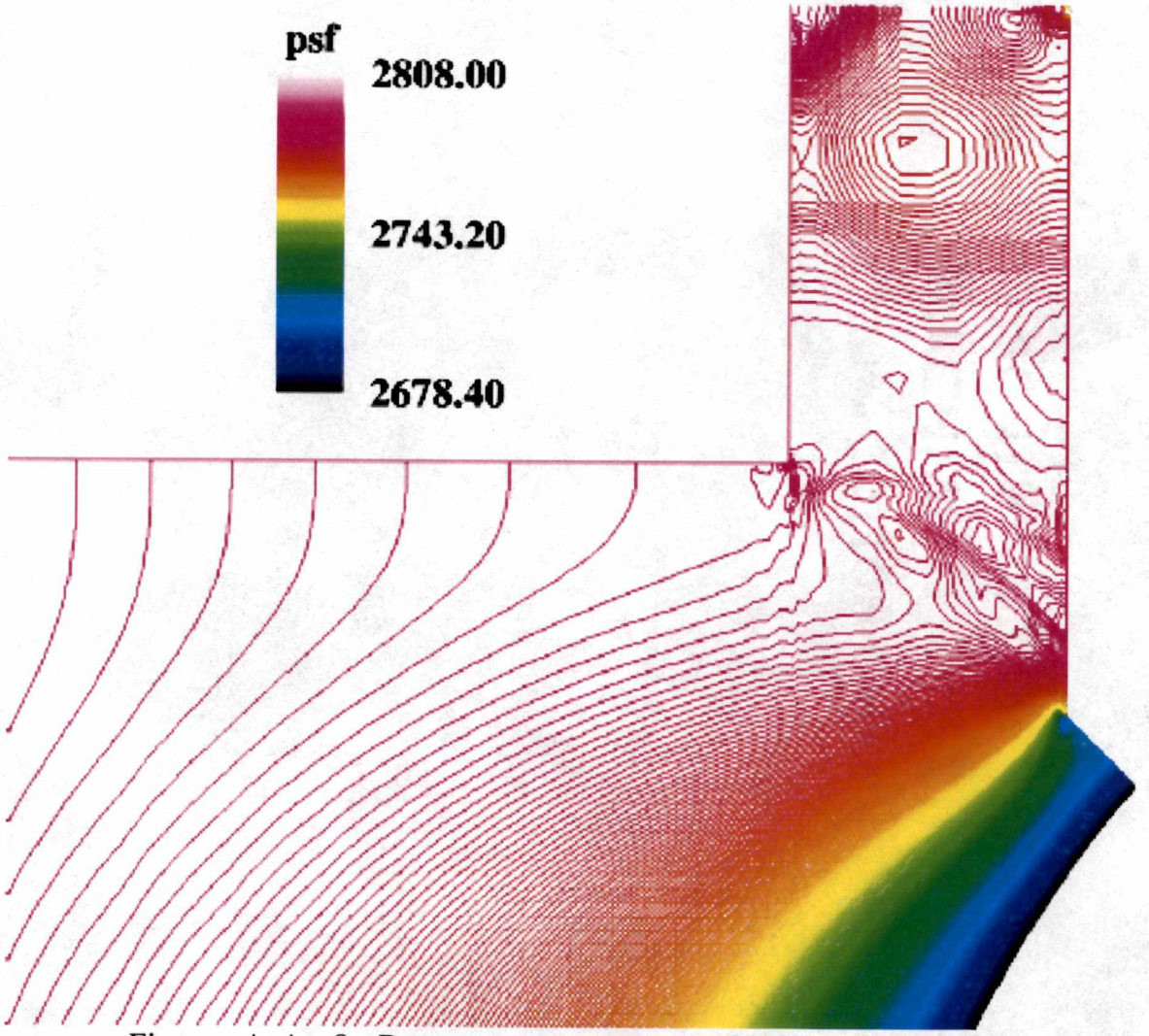


Figure A-A. 8. Pressure contours at 8/10th of a cycle.

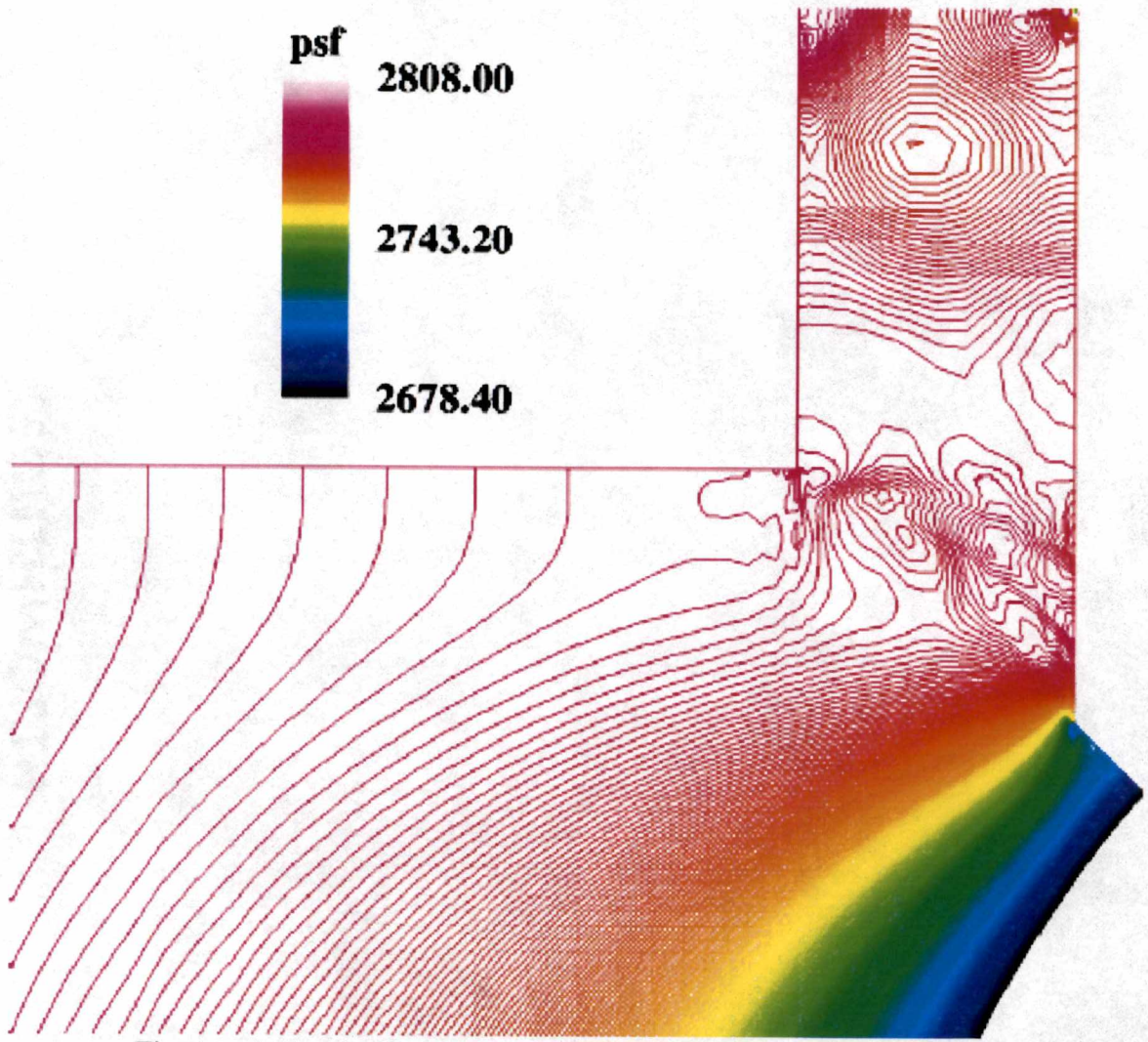


Figure A-A. 9. Pressure contours at 9/10th of a cycle.

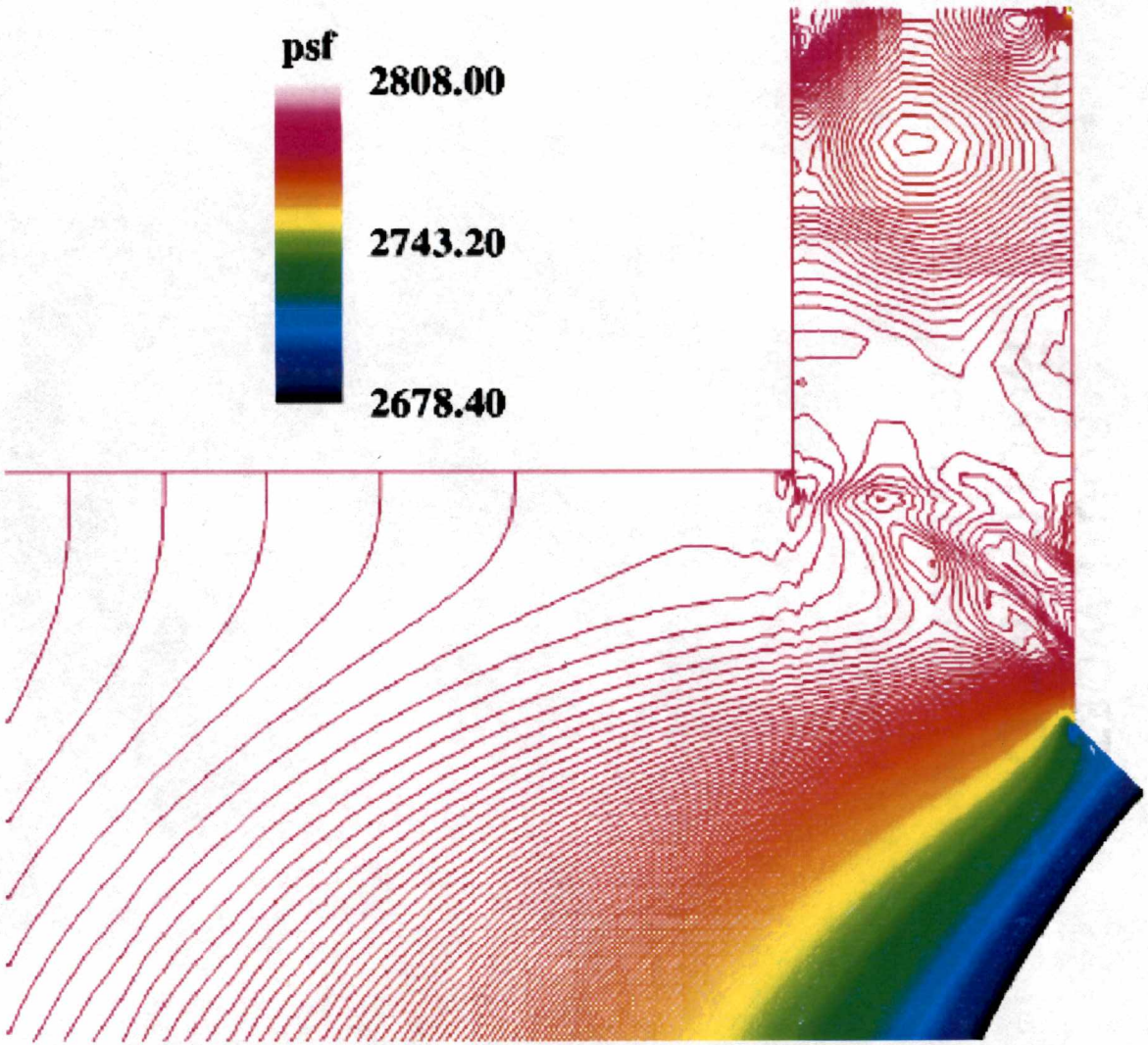


Figure A-A. 10. Pressure contours at 10/10th of a cycle.

APPENDIX B

VELOCITY MAGNITUDE FIGURES

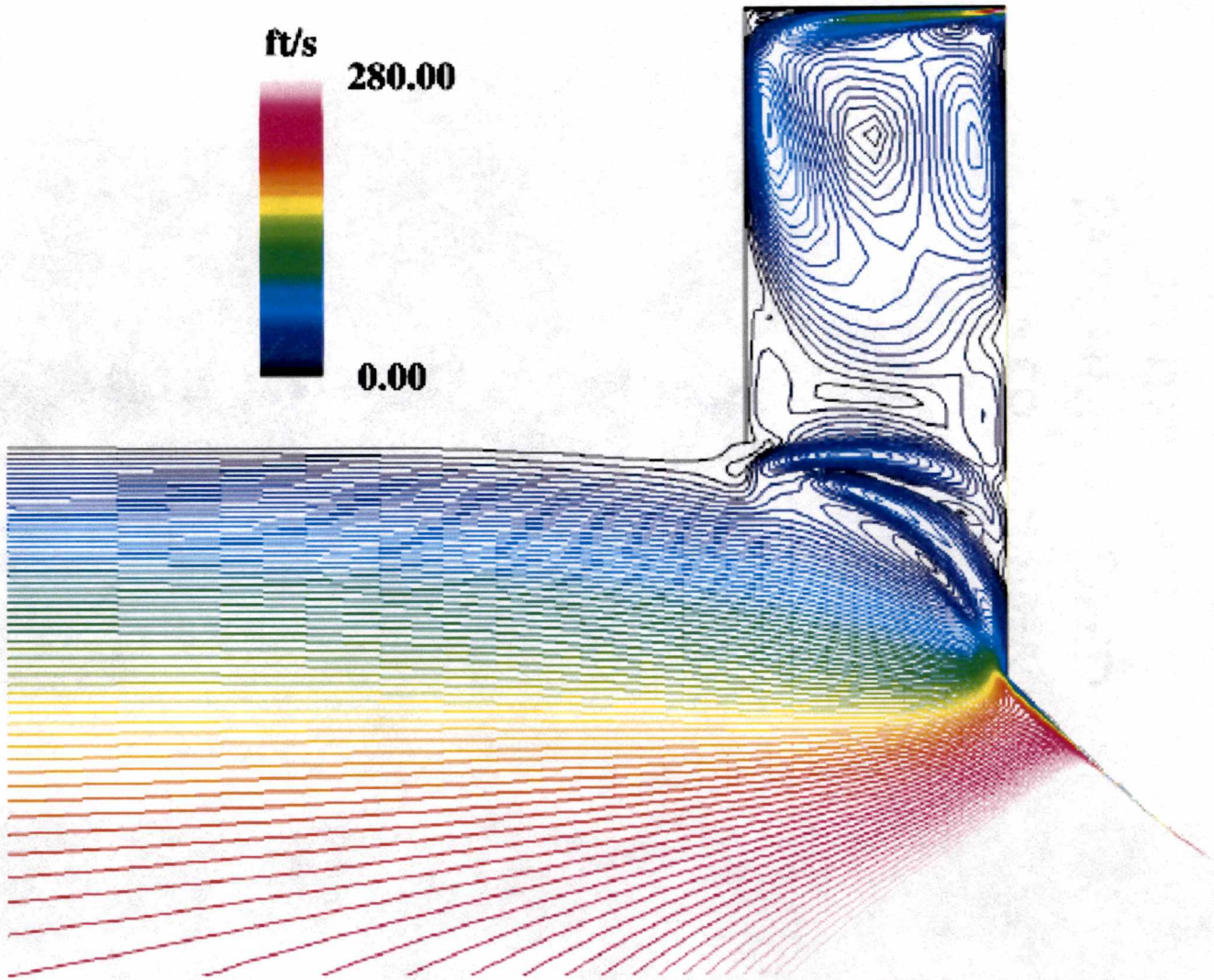


Figure A-B. 1. Velocity magnitude contours at 1/10th of a cycle.

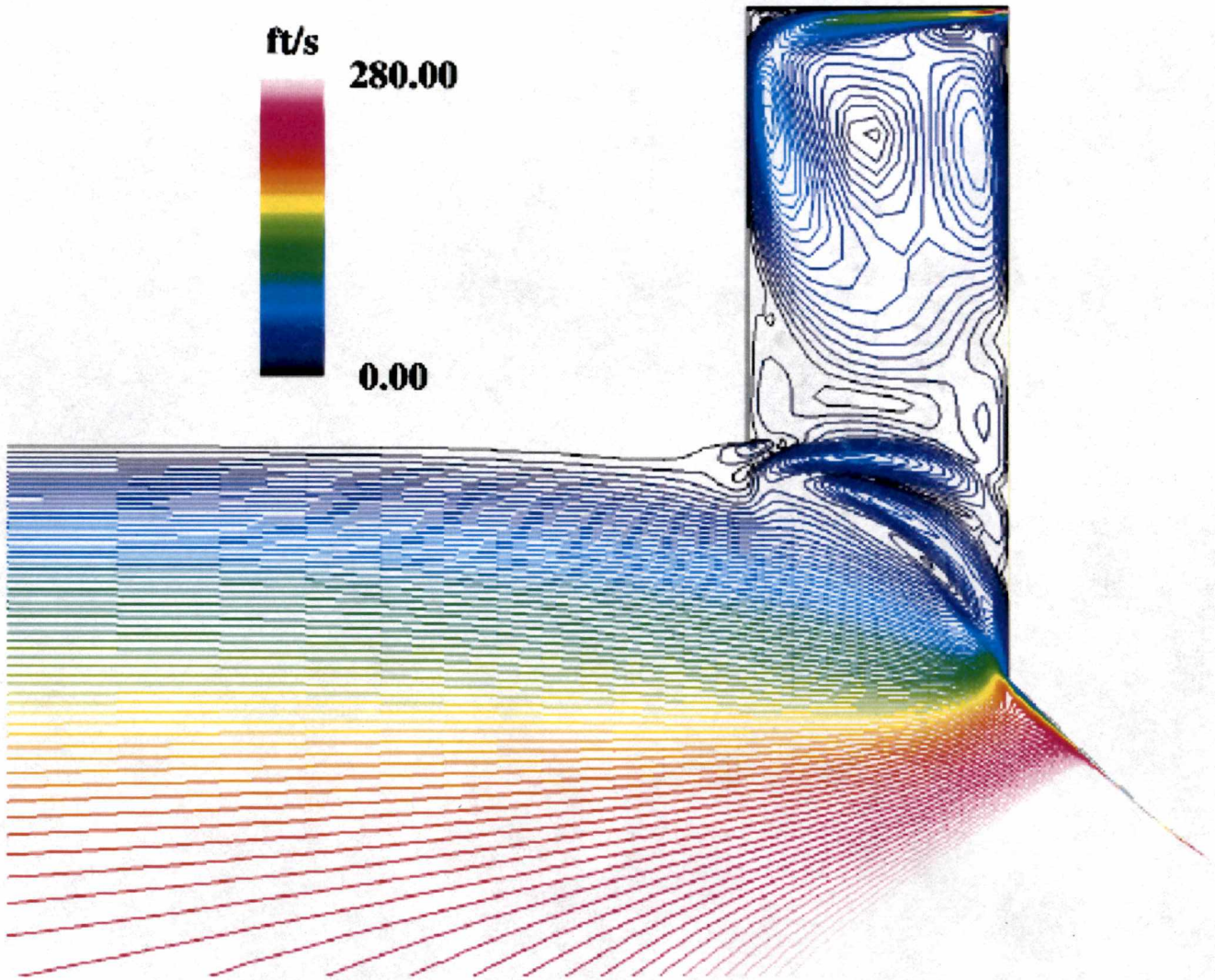


Figure A-B. 2. Velocity magnitude contours at 2/10th of a cycle.

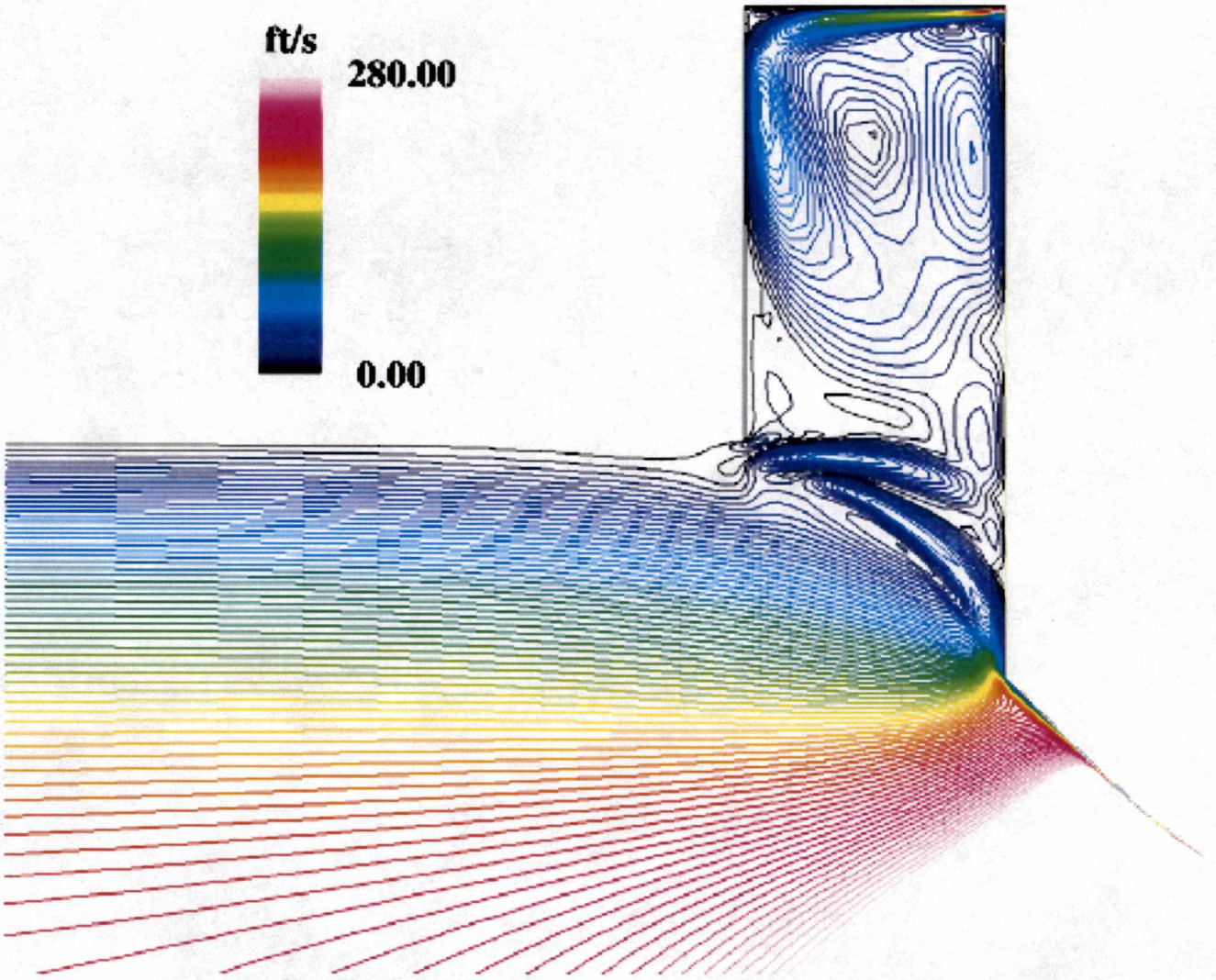


Figure A-B. 3. Velocity magnitude contours at 3/10th of a cycle.

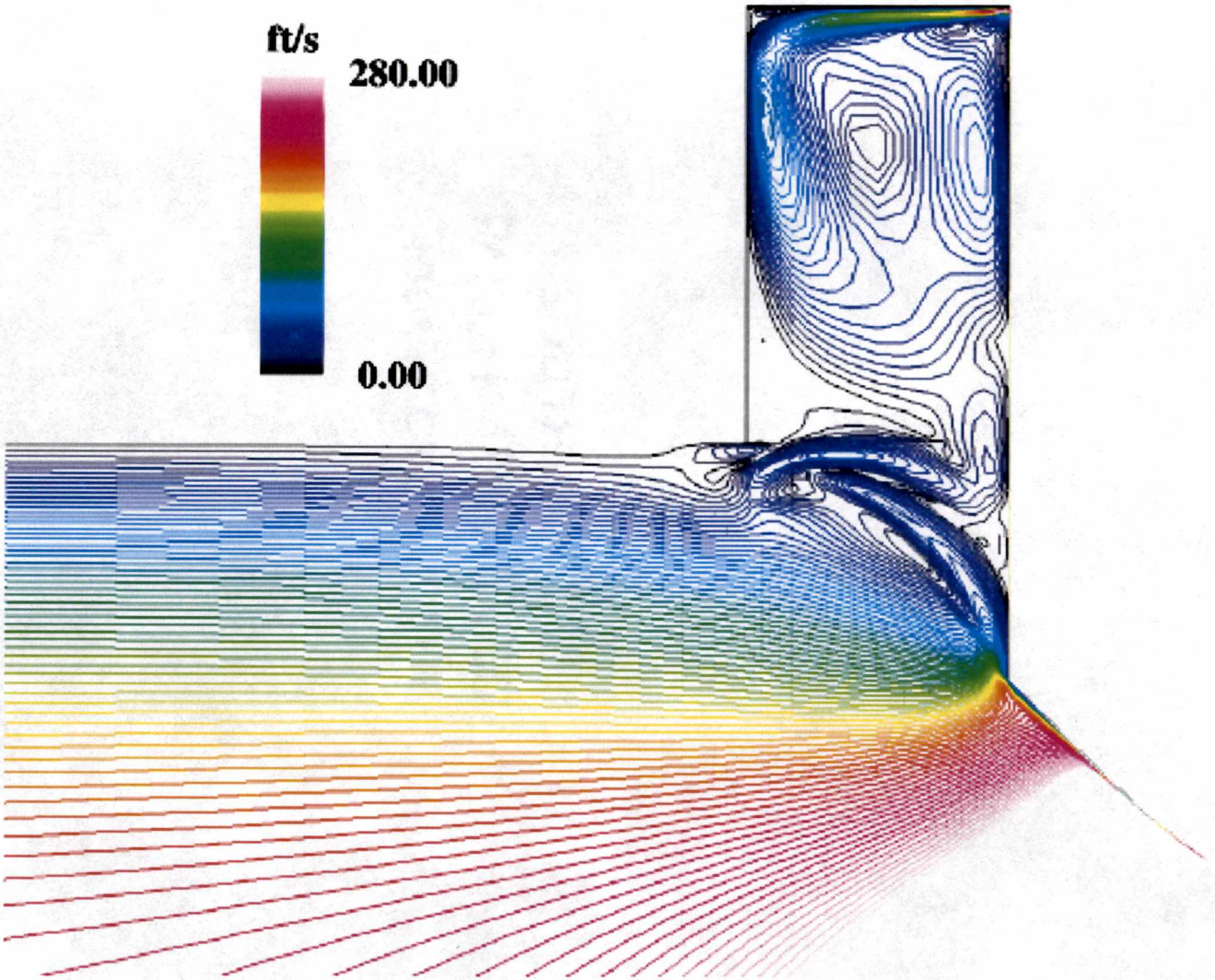


Figure A-B. 4. velocity magnitude contours at 4/10th of a cycle.

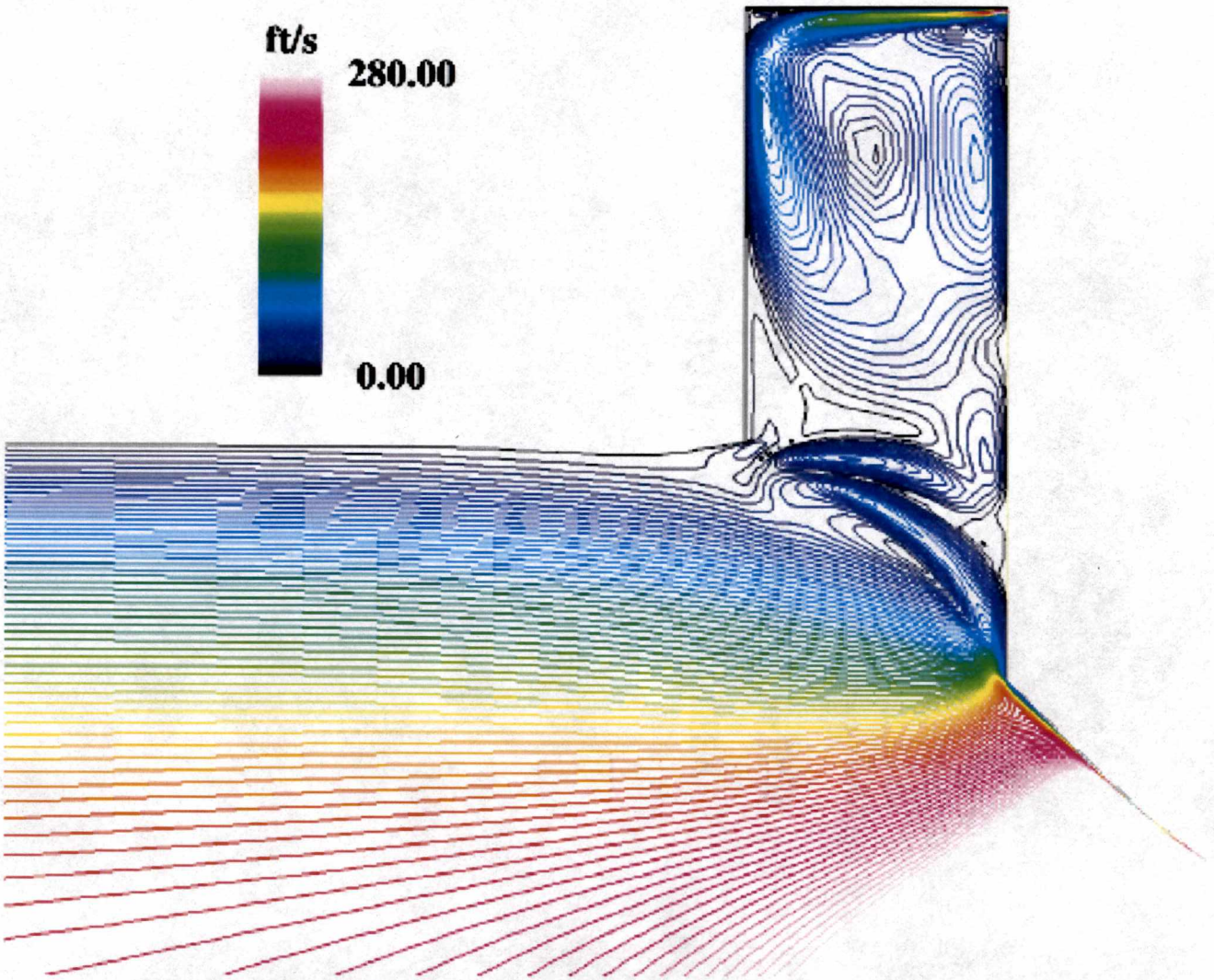


Figure A-B. 5. Velocity magnitude contours at 5/10th of a cycle.

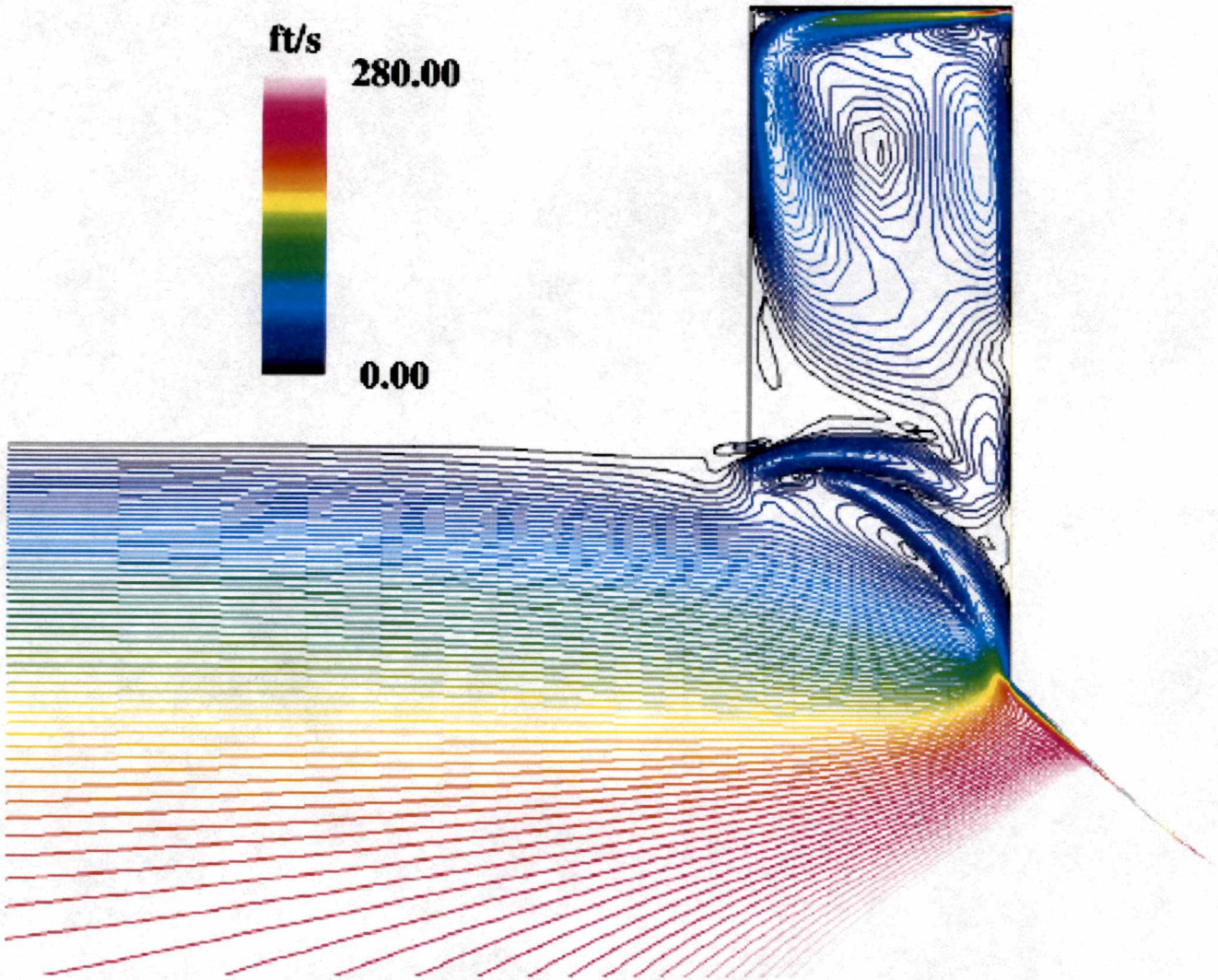


Figure A-B. 6. Velocity magnitude contours at 6/10th of a cycle.

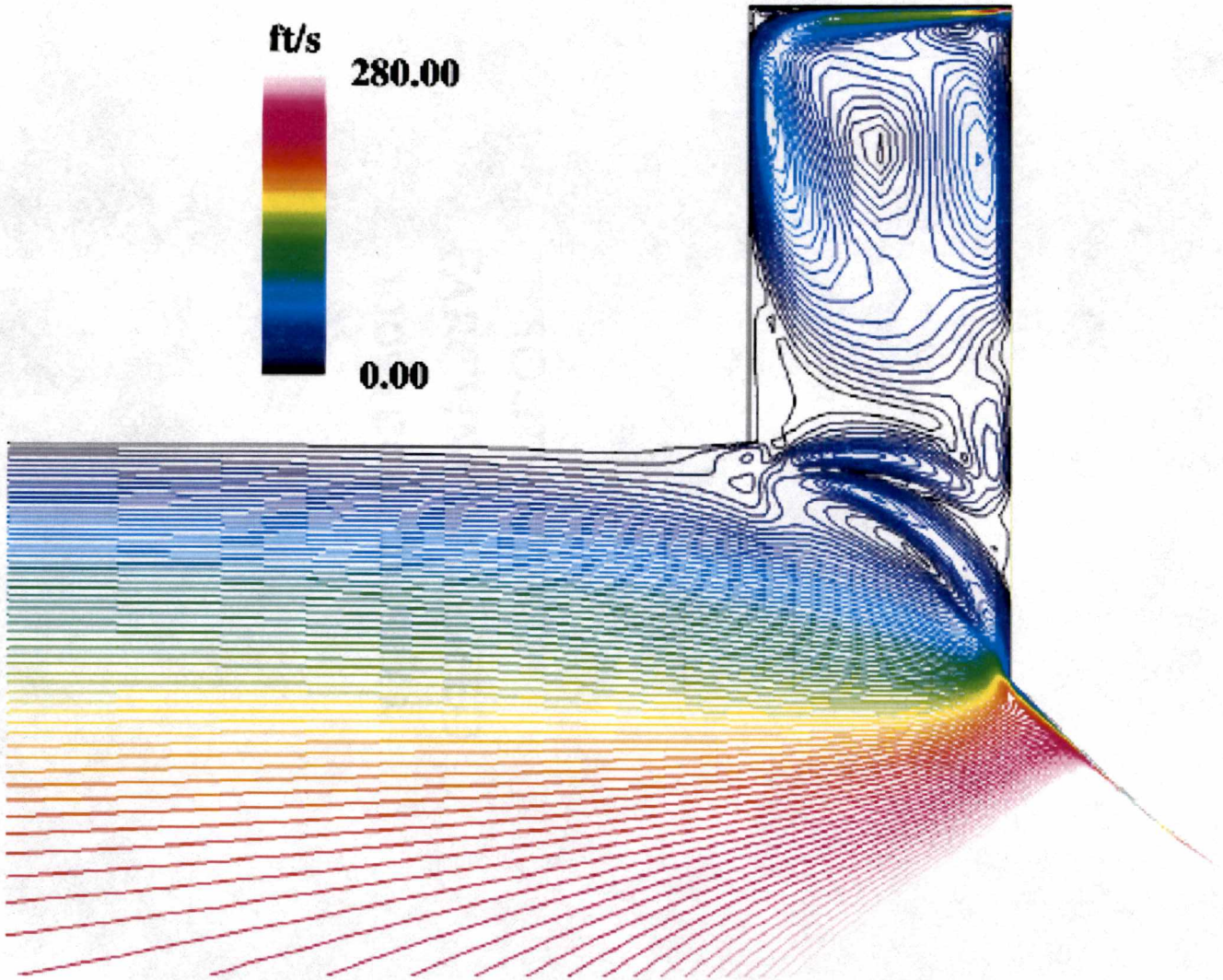


Figure A-B. 7. Velocity magnitude contours at 7/10th of a cycle.

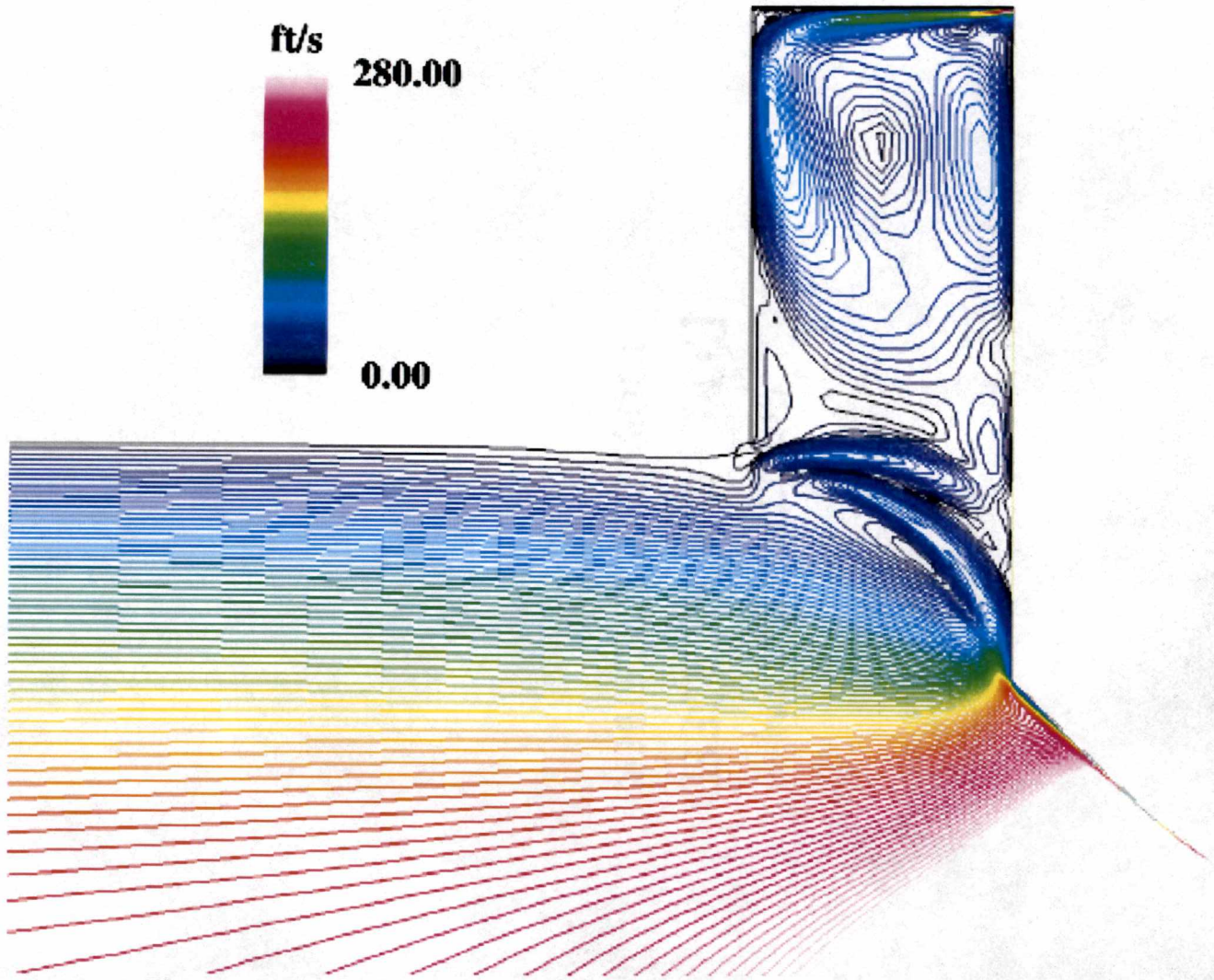


Figure A-B. 8. Velocity magnitude contours at 8/10th of a cycle.

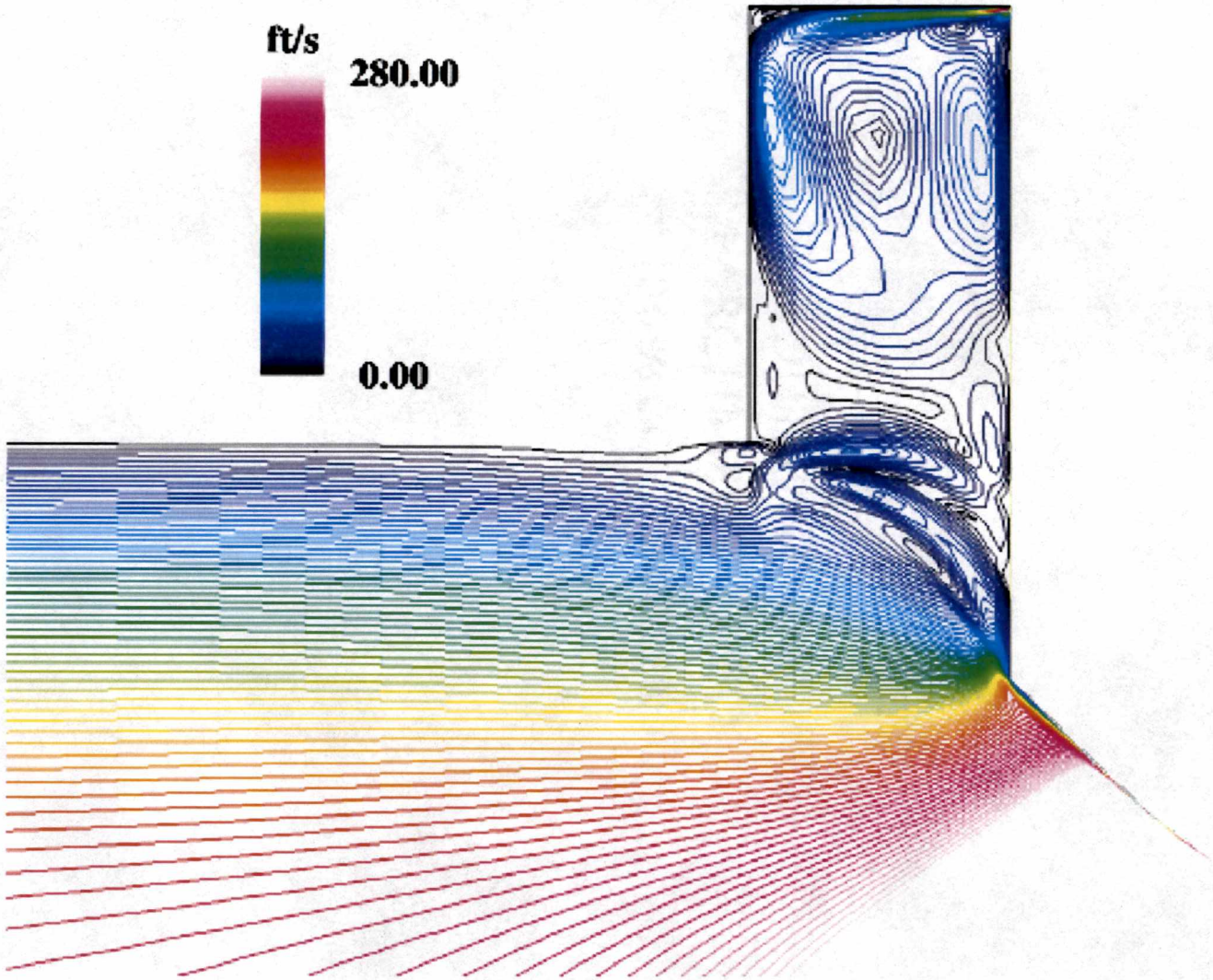


Figure A-B. 9. Velocity magnitude contours at 9/10th of a cycle.

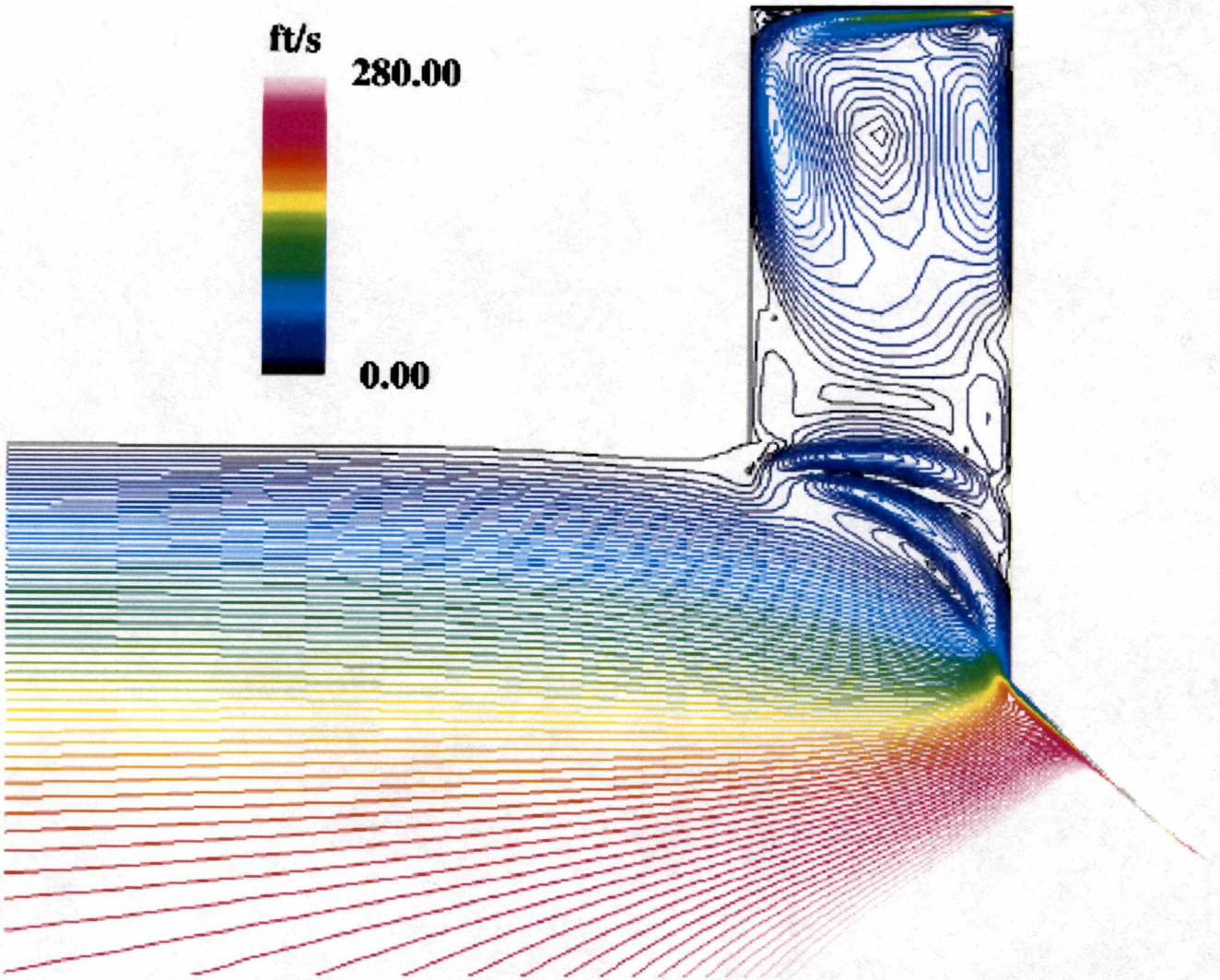


Figure A-B. 10. Velocity magnitude contours at 10/10th of a cycle.

APPENDIX C

CLOSE-UP FIGURES OF VELOCITY MAGNITUDE IN THE SLOT

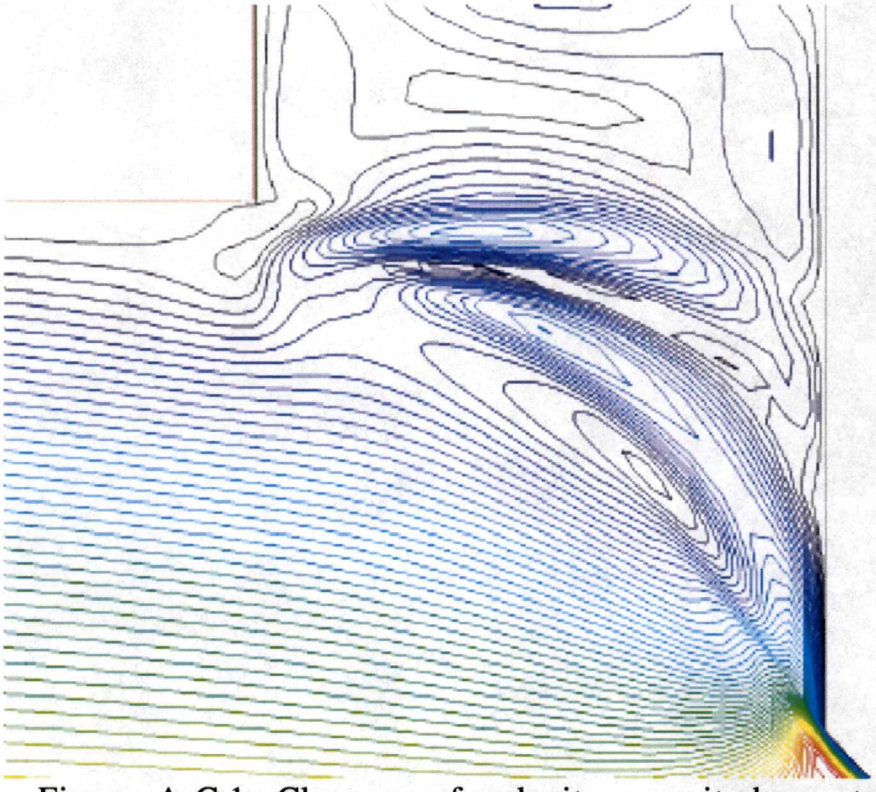


Figure A-C.1. Close-up of velocity magnitude contours near the slot at 1/10th of a cycle.

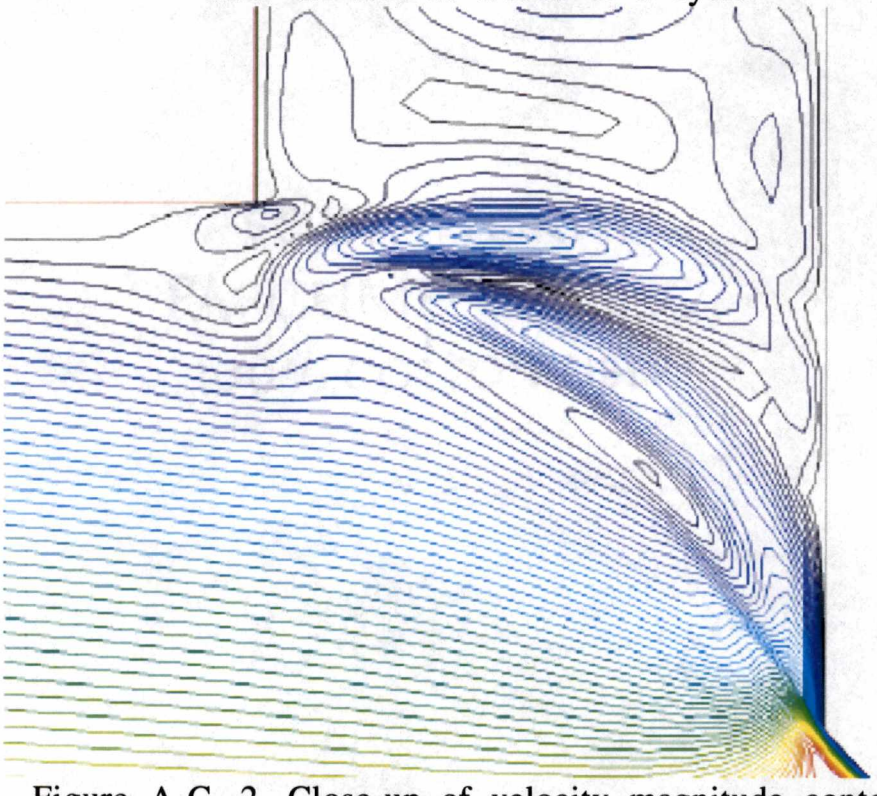


Figure A-C. 2. Close-up of velocity magnitude contours near the slot at 2/10th of a cycle.

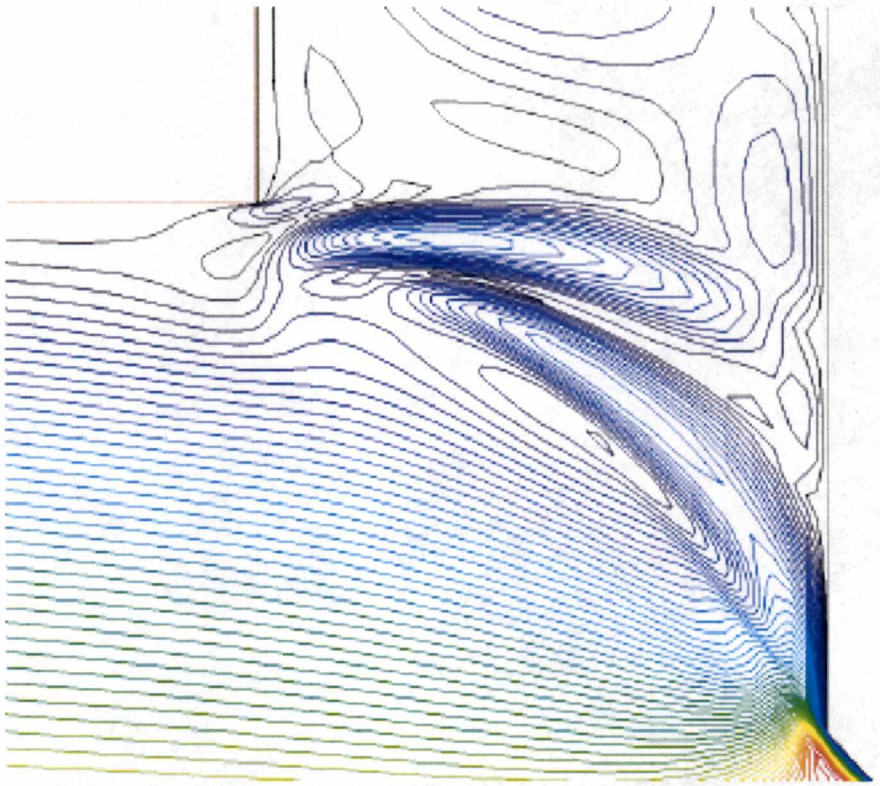


Figure A-C. 3. Close-up of velocity magnitude contours near the slot at 3/10th of a cycle.

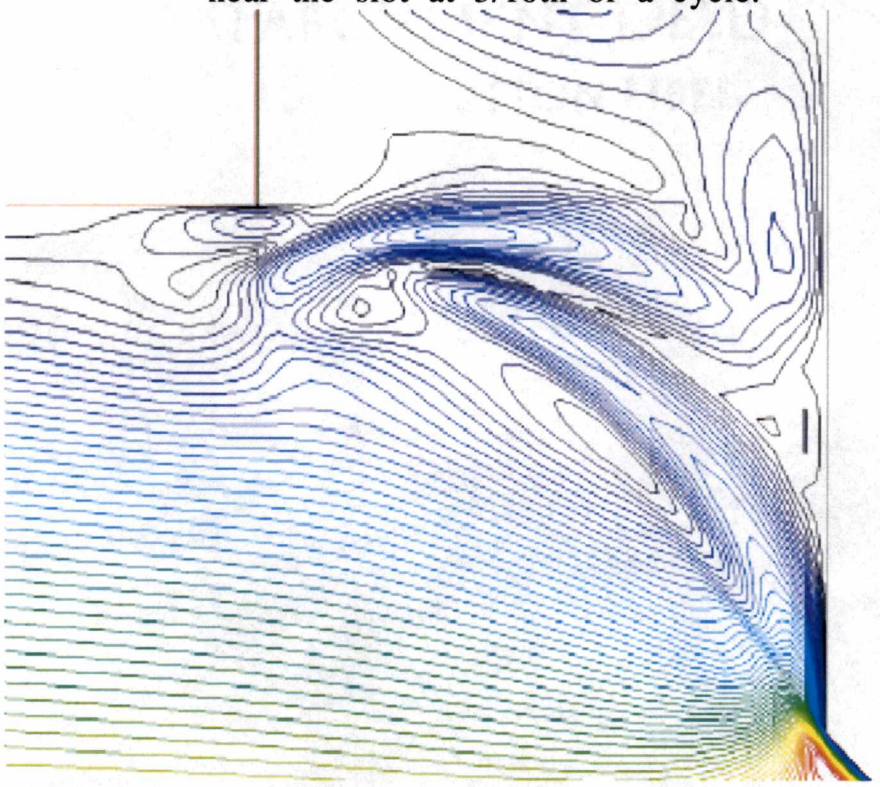


Figure A-C. 4. Close-up of velocity magnitude contours near the slot at 4/10th of a cycle.

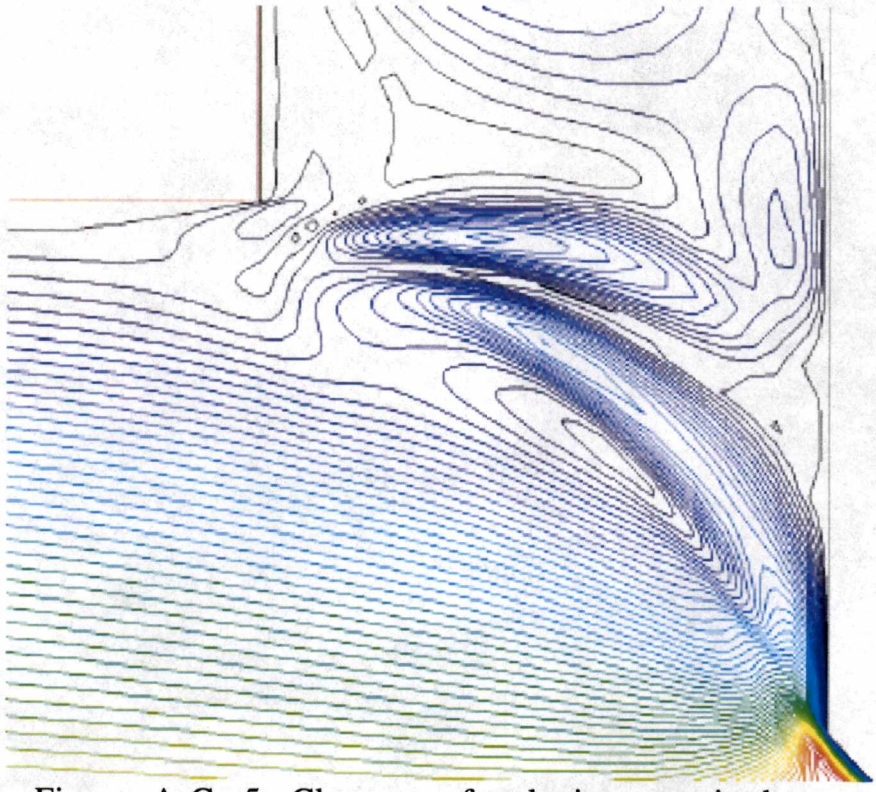


Figure A-C. 5. Close-up of velocity magnitude contours near the slot at 5/10th of a cycle.

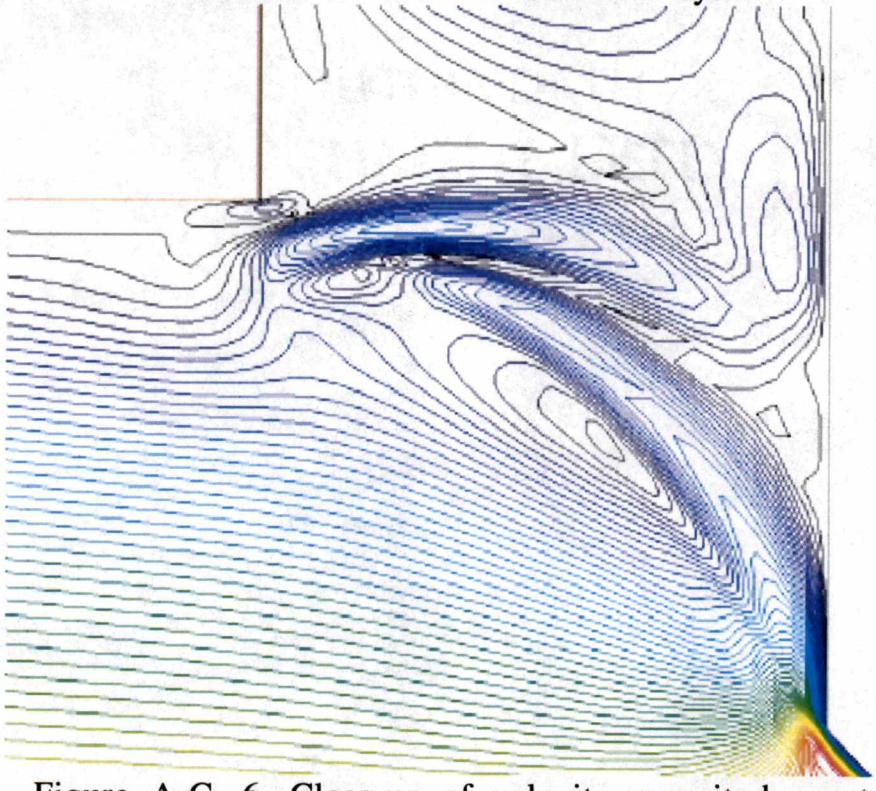


Figure A-C. 6. Close-up of velocity magnitude contours near the slot at 6/10th of a cycle.

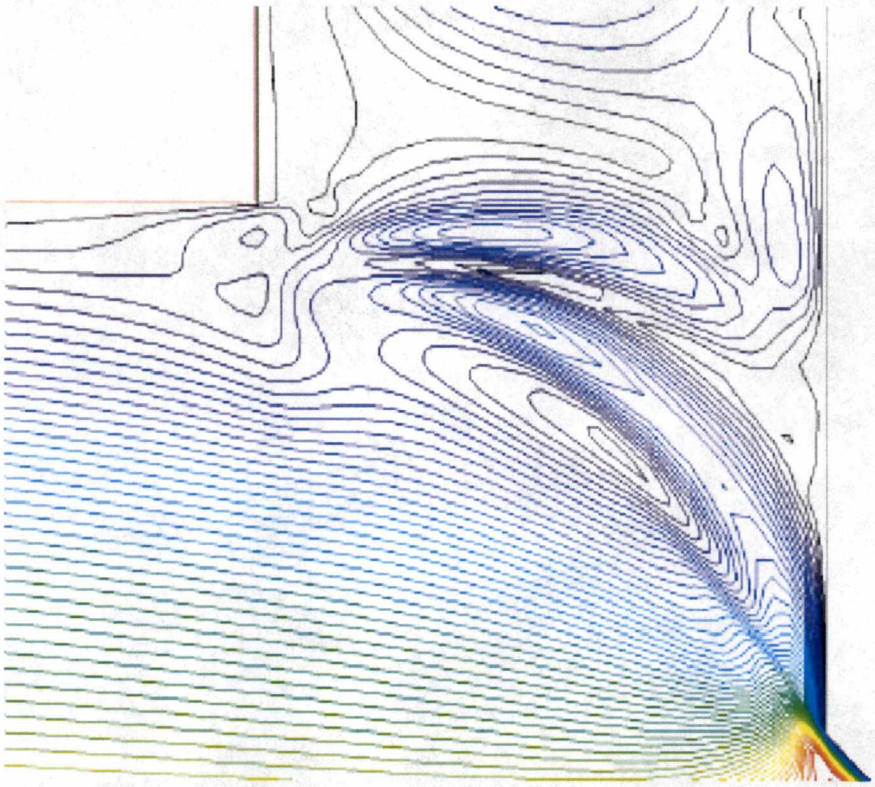


Figure A-C. 7. Close-up of velocity magnitude contours near the slot at 7/10th of a cycle.

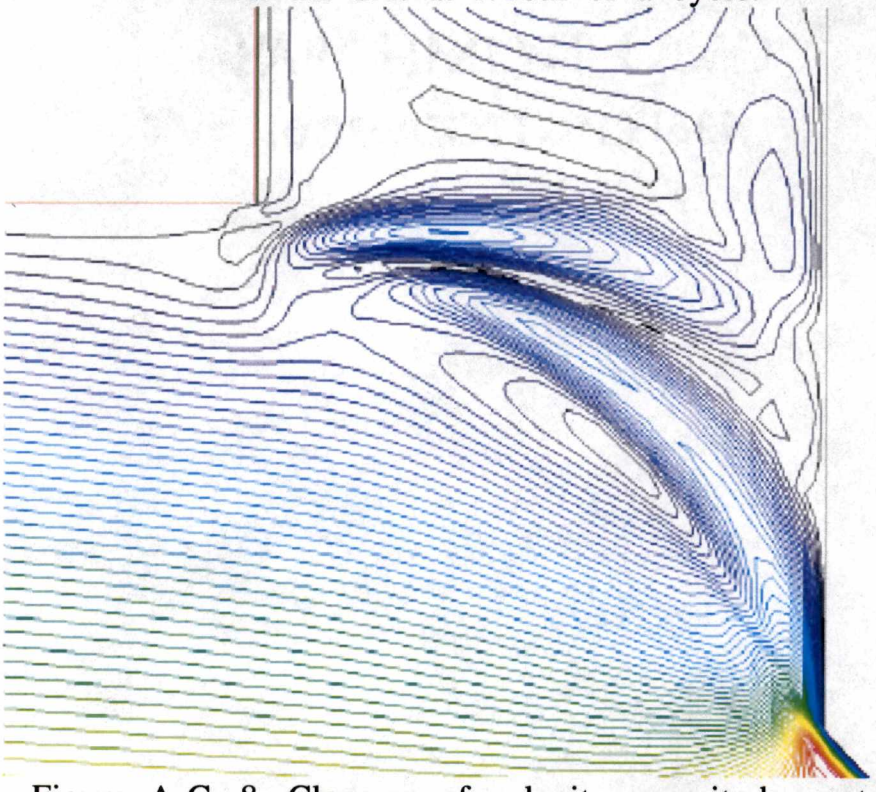


Figure A-C. 8. Close-up of velocity magnitude contours near the slot at 8/10th of a cycle.

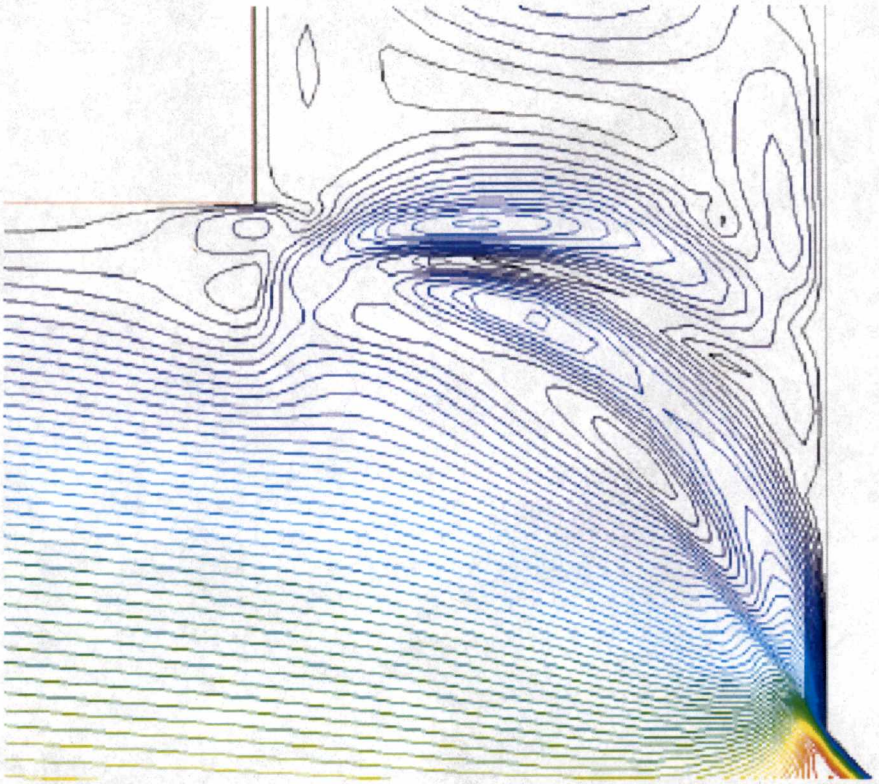


Figure A-C. 9. Close-up of velocity magnitude contours near the slot at 9/10th of a cycle.

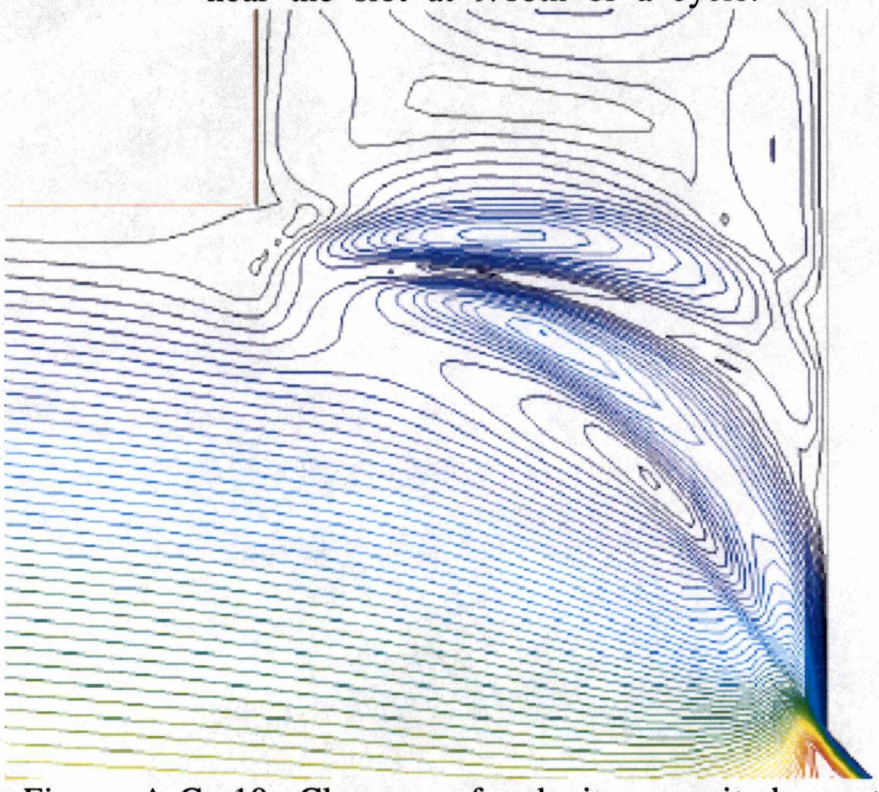


Figure A-C. 10. Close-up of velocity magnitude contours near the slot at 10/10th of a cycle.

APPENDIX D

CLOSE-UP FIGURES OF VELOCITY VECTORS IN THE SLOT

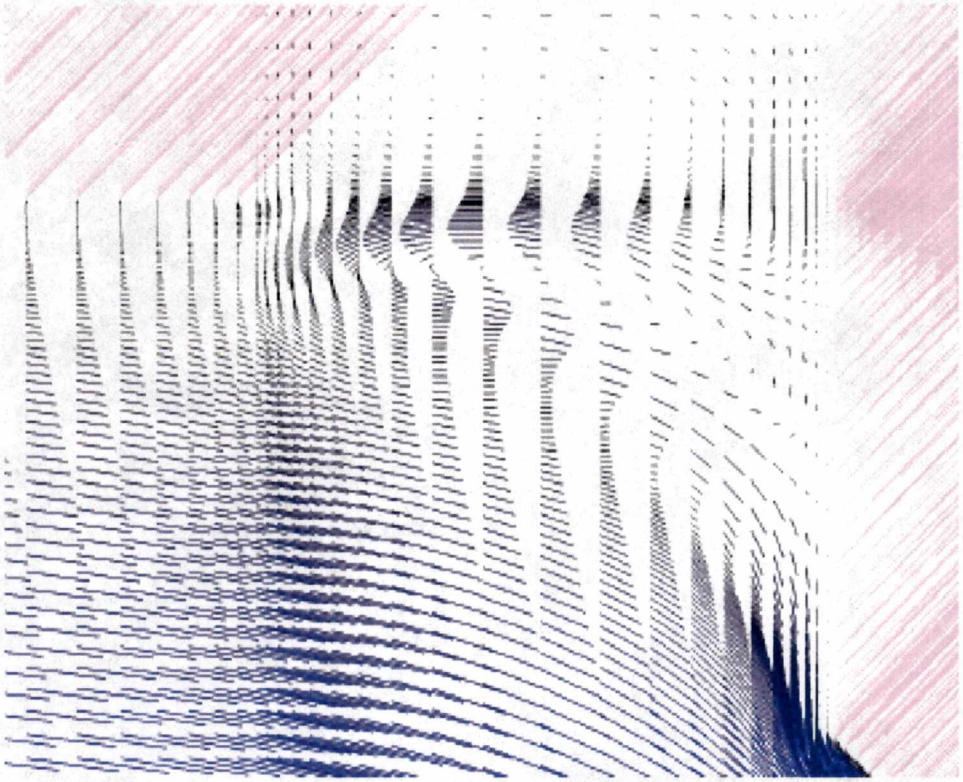


Figure A-D. 1. Close-up of velocity vectors near the slot at 1/10th of a cycle.

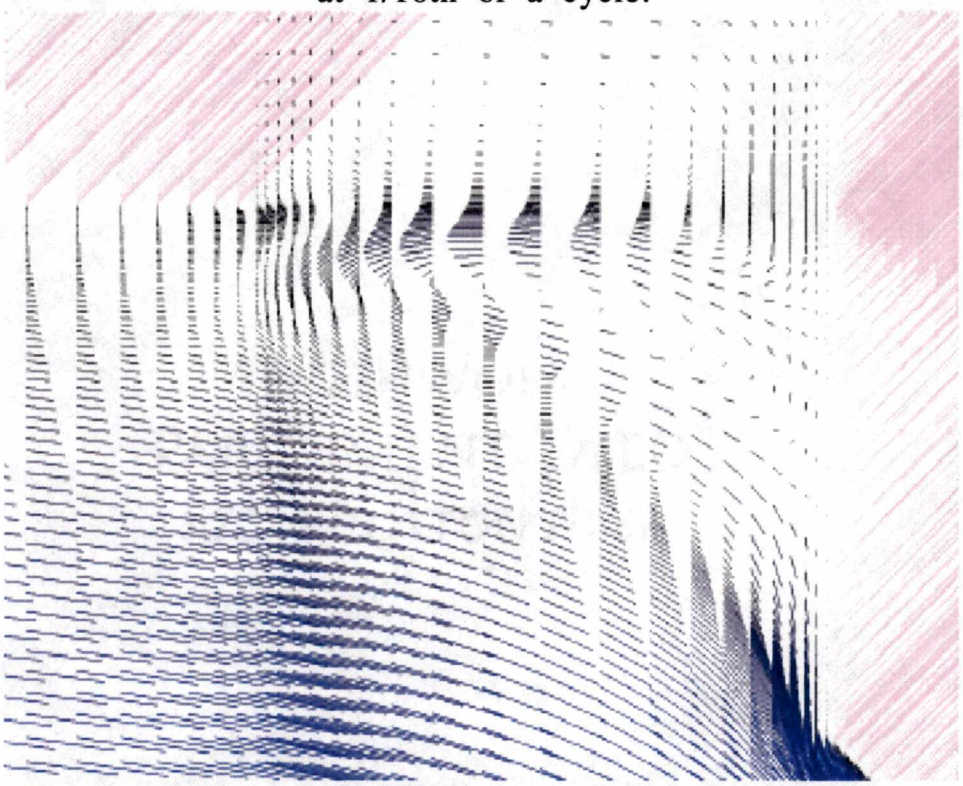


Figure A-D. 2. Close-up of velocity vectors near the slot at 2/10th of a cycle.

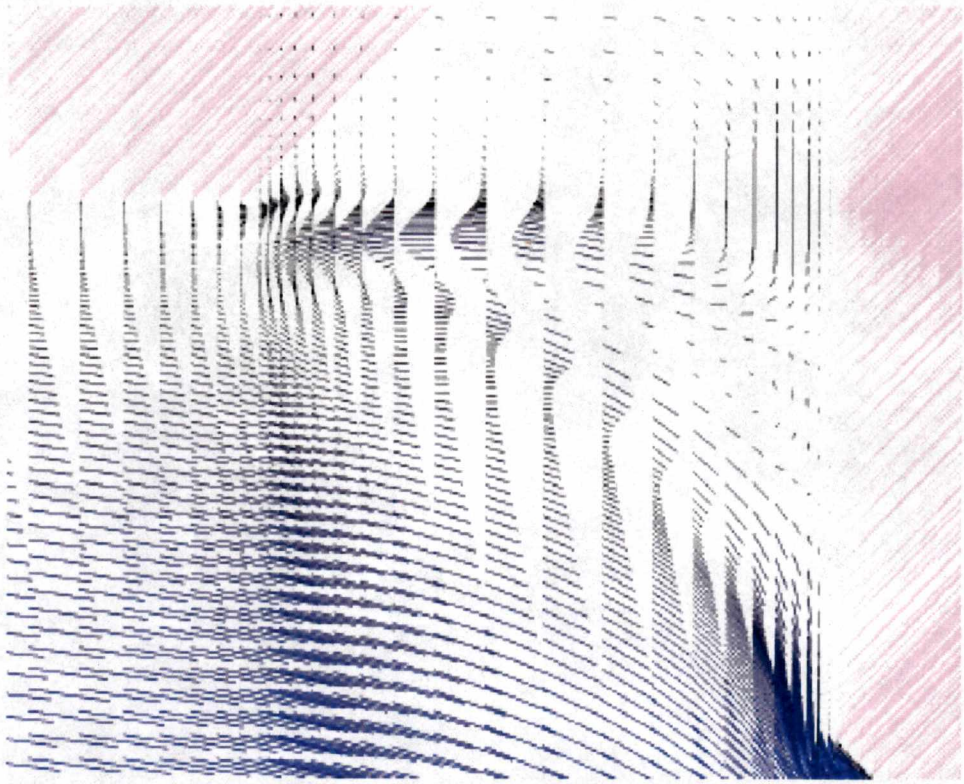


Figure A-D. 3. Close-up of velocity vectors near the slot at 3/10th of a cycle.

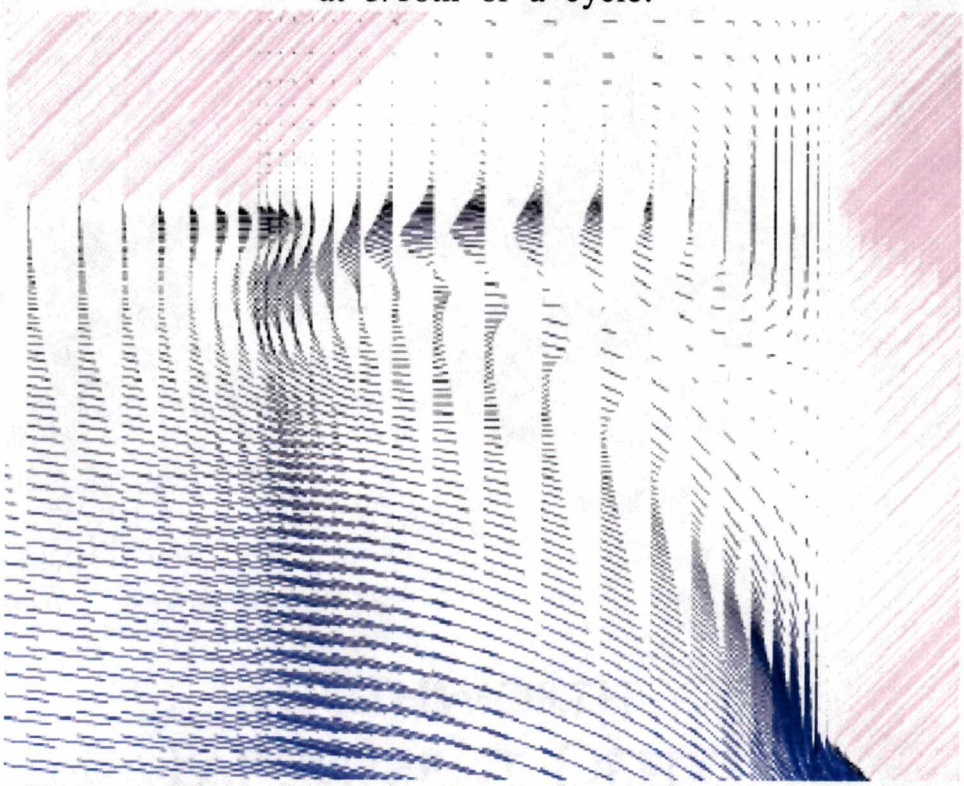


Figure A-D. 4. Close-up of velocity vectors near the slot at 4/10th of a cycle.

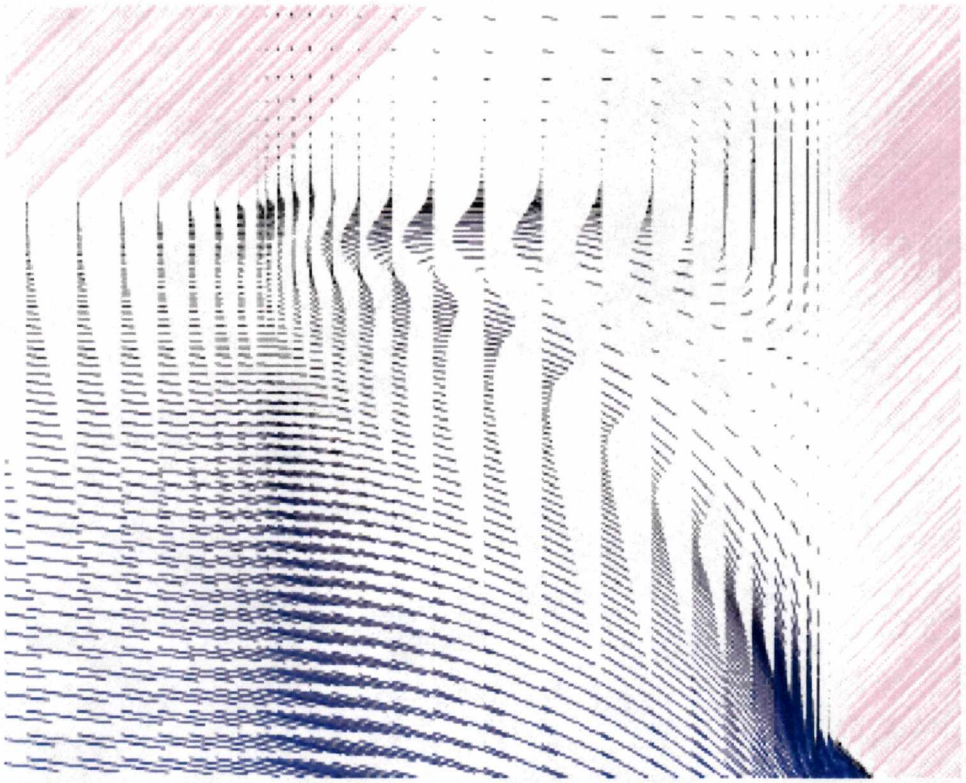


Figure A-D. 5. Close-up of velocity vectors near the slot at 5/10th of a cycle.

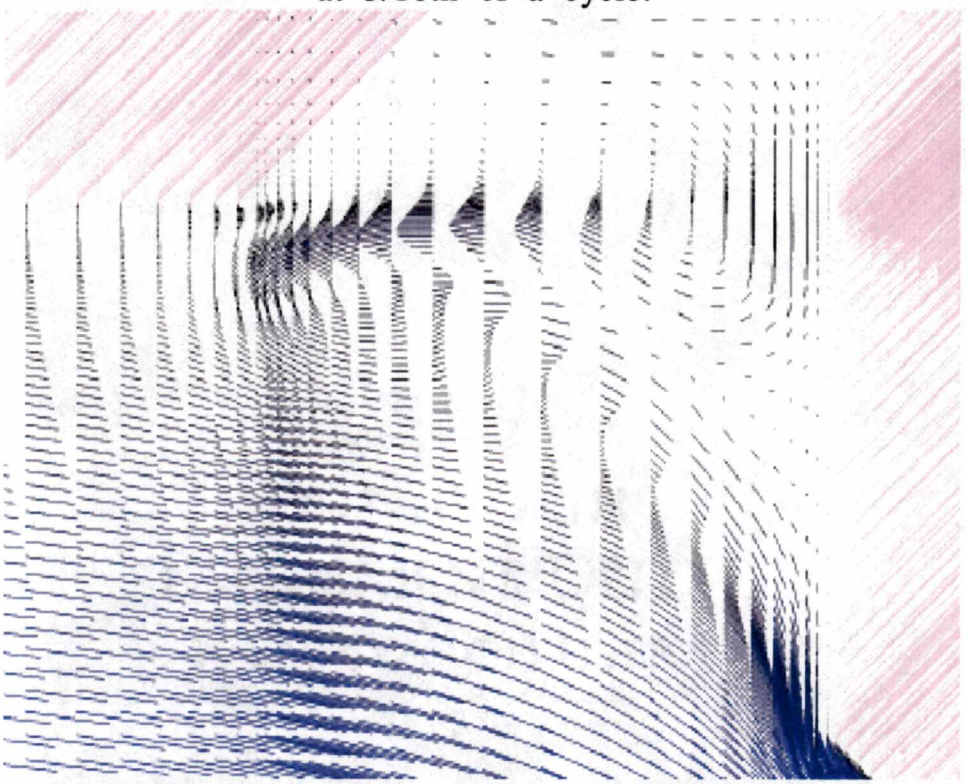


Figure A-D. 6. Close-up of velocity vectors near the slot at 6/10th of a cycle.

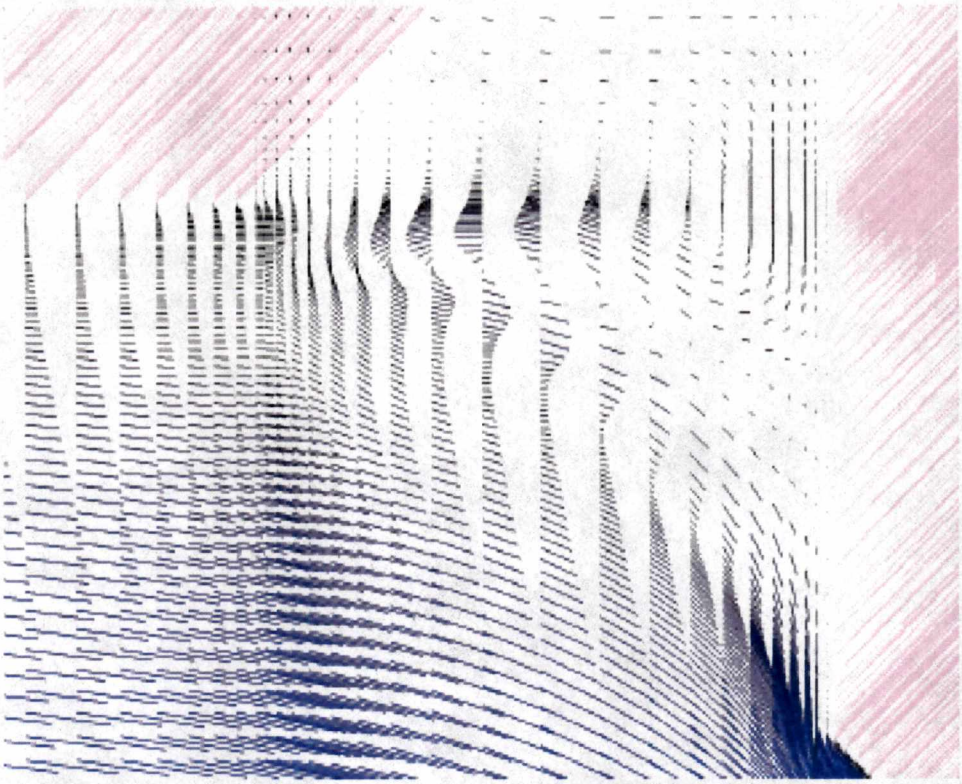


Figure A-D. 7. Close-up of velocity vectors near the slot at 7/10th of a cycle.

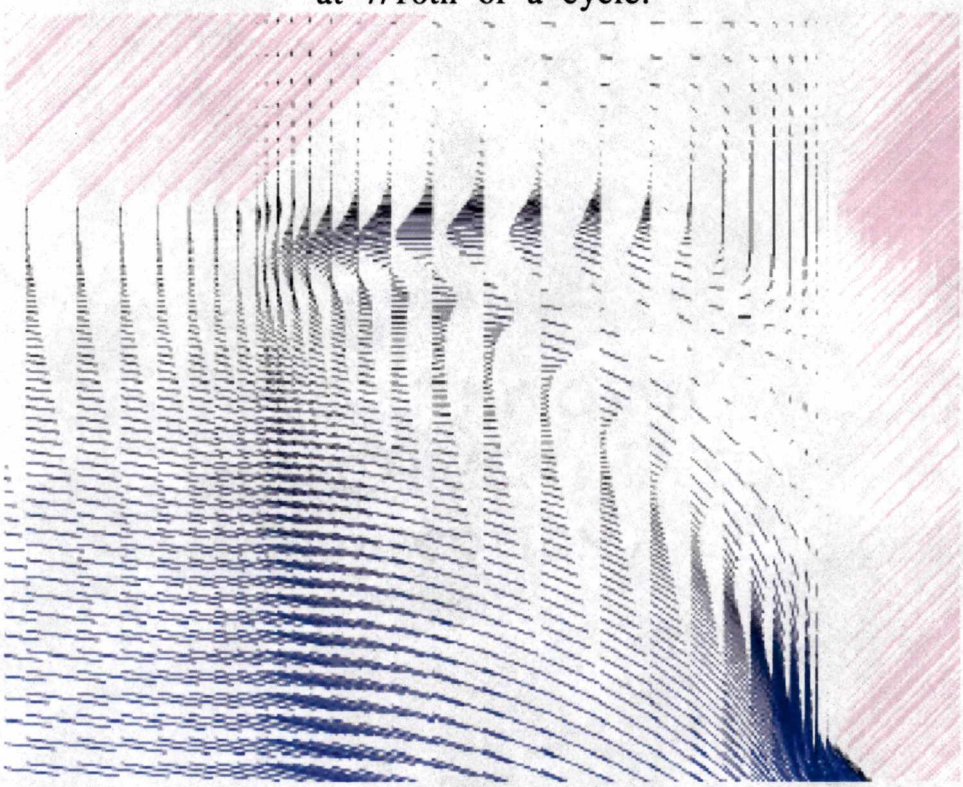


Figure A-D. 8. Close-up of velocity vectors near the slot at 8/10th of a cycle.

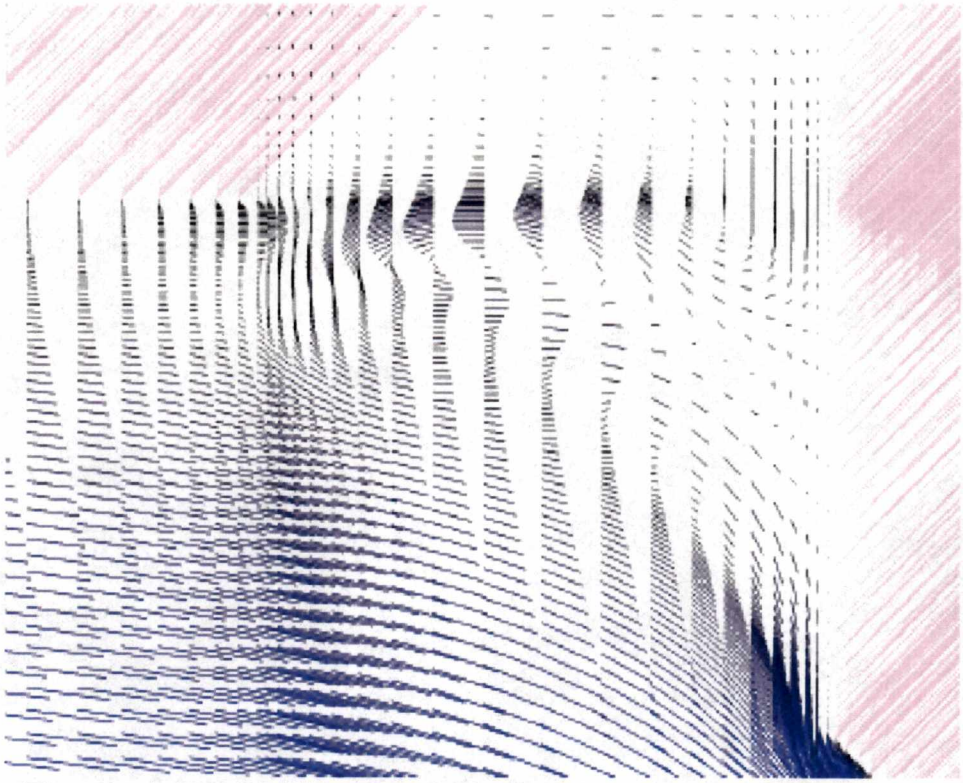


Figure A-D. 9. Close-up of velocity vectors near the slot at 9/10th of a cycle.

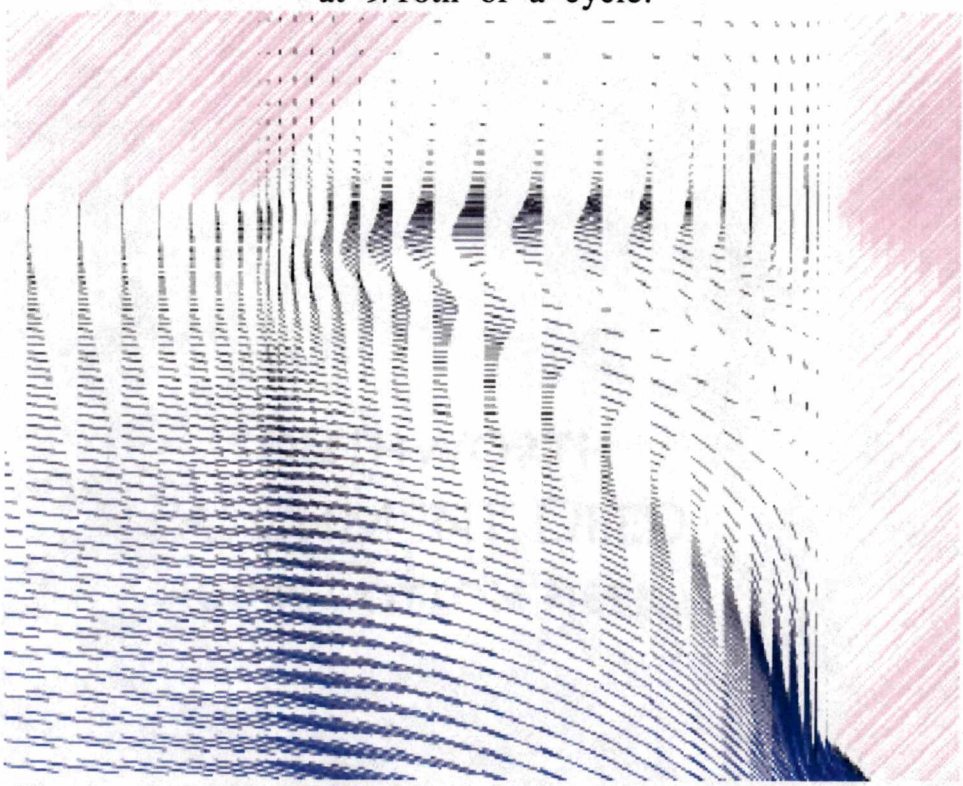


Figure A-D. 10. Close-up of velocity vectors near the slot at 10/10th of a cycle.

VITA

Sheri Lea Hlady was born on 8 April 1969 in Calgary, Alberta, Canada. She attended schools in Calgary's Catholic School System and graduated in 1987. In 1988, Sheri moved south for the warmer climes of L.A. (Lethbridge, Alberta) and to attend the University of Lethbridge. After completing her Bachelor's of Arts in Psychology in 1993, Sheri was encouraged to pursue medical studies. While continuing her studies at the University of Lethbridge in pre-med., Sheri discovered a love for Physics. Although Sheri had been exposed, briefly, to physics in high school, the experience was not particularly gratifying. In Dr. Mark Walton's first year physics class at the University of Lethbridge, Sheri discovered that physics offered a unique challenge with wonderful reward. She changed majors, and in 1996 completed a Bachelor's of Science in Physics. While researching possible schools at which to pursue postgraduate studies, Sheri found that the University of Tennessee Space Institute offered a unique opportunity for study. In August of 1996, Sheri changed majors again, and moved even further south to even warmer climes. In December 1998, Sheri completed her Master's of Science in Engineering Science. Changing topics (and perhaps majors) again, Sheri has been accepted into the doctoral program at the University of Tennessee Space Institute for January 1999. To fulfill her love of education, Sheri hopes to explore new horizons and, as always, new majors.